Photophysics and Structural Dynamics in Metal-Halide Perovskite Semiconductors

Vincent Jae-Yeon Lim

St. Hilda's College

University of Oxford

A thesis submitted for the degree of

Doctor of Philosophy

Michaelmas 2024

Acknowledgements

Firstly, I would like to express my gratitude to Oxford Photovoltaics and EPSRC for their funding of my studentship, and Rank Prize for their financial support through the Return to Research Grant Scheme.

I am very grateful to my supervisor, Professor Laura Herz, for her guidance, support, and inspiration throughout my degree, and to Professor Michael Johnston for helpful discussions. I have learnt a lot from them and grown as a scientist and a researcher during my degree.

I would like to thank everyone in the Herz-Johnston group for their wonderful company, all the beautiful memories made together, and making the journey so enjoyable. I would like to thank in particular: Leonardo Buizza, Thomas Haward, Alexander Knight, Snigdha Lal, Jae Eun Lee, Joshua Lilly, Thomas Siday, Ford Wagner and Siyu Yan. Special thanks go to: Karim Elmestekawy, my partner in crime, for supporting me throughout our journeys together, and for his company on walks to the post office and the water fountain; Marcello Righetto, el pastor, for his scientific and life advice, and venting sessions; and Aleksander Ulatowski, forever my mentor, for the fun lab sessions, scientific discussions, and his enthusiasm for science, engineering and coffee. These people are who made my journey and my time at Oxford so amazing and memorable, and I have learnt so much, both academically and personally, from these wonderful friends.

Lastly, I would like to thank my mother, father, and brother for absolutely everything. I am also thankful to my friends for their encouragement, and Shani Yang for her love, care and support.

Abstract

Metal-halide perovskites have been under intense research over the past decade due to their potential to compete with and complement silicon in solar photovoltaic devices, owing to their affordability and better device performances. However, their commercialisation has been hindered mainly due to their problems with stability, which requires more thorough fundamental investigation of these materials. This thesis focuses on understanding their photophysics and structural dynamics through various spectroscopic techniques. More specifically, metal-halide perovskites have issues regarding halide segregation and tin oxidation, as well as intriguing low-frequency Raman response, which are addressed in this thesis.

The effects of a hole-transport layer and defect passivation on halide segregation under illumination in mixed-halide perovskites have been investigated using in-situ photoluminescence and X-ray diffraction. It is demonstrated that using photoluminescence on its own may be misleading when studying halide segregation, especially when a charge-transport layer is present. The introduction of a hole-transport layer slows down halide segregation due to hole depletion, but increases the photoluminescence intensity through hole back-transfer into iodide-rich regions near the interface between the perovskite and the hole-transport layer. It is shown that defect passivation has a profound and complex effect on halide segregation, and the nature of the trap states determines their role in halide segregation.

The degradation mechanisms in tin-only and mixed lead-tin iodide perovskites in ambient air have been examined. Although these two different types of perovskites both undergo severe optoelectronic degradation in ambient air over a few hours, their degradation mechanisms have been shown to differ; tin-only perovskites undergo heavy doping of the valence band when exposed to ambient air, but mixed lead-tin perovskites do not undergo any significant doping during exposure. It was concluded that tin-only perovskites degrade via introduction of shallow defect states which contribute to hole-doping of the valence band, while mixed lead-tin perovskites degrade via formation of deep trap states which do not significantly dope either of the electronic bands. Possible degradation products during ambient air exposure of these perovskites have also been identified.

Finally, low-frequency vibrational properties of metal-halide perovskites were investigated. Metal-halide perovskites have been reported to have intriguing responses in low-frequency Raman spectra, where the response is extremely broad. However, this is not the case for IR spectra, where only well-defined contribution from phonon modes are visible. The origin of the broad Raman response, as well as the discrepancy between Raman and IR spectra, has been an actively debated topic in the literature, with various hypotheses being presented. Through Raman and IR spectra of various metal-halide semiconductors and literature data, a number of hypotheses have been ruled out as the main cause of such Raman response. Those that are ruled out include: extrinsic defects, octahedral tilting, cation lone pairs, and 'liquid-like' Boson peaks. Instead, an alternative explanation for such broad Raman response and the discrepancy with IR spectra was presented: the broad Raman response is a result of an interplay of significant broadening of Raman-active vibrational modes and a Bose-Einstein population factor, while IR-active vibrational modes are subject to different and slower decay channels, and such Bose-Einstein population factor is not applicable to IR spectra.

Contents

Appendices

List of Publications

- **Lim, V. J. -Y.**, Knight, A. J., Oliver, R. D. J., Snaith, H. J., Johnston, M. B., Herz, L. M. ‘Impact of Hole-Transport Layer and Interface Passivation on Halide Segregation in Mixed-Halide Perovskites’. *Advanced Functional Materials*, **2022**, 32(41), 2204825.
- **Lim, V. J. -Y.**, Ulatowski, A. M., Kamaraki, C., Klug, M. T., Miranda Perez, L., Johnston, M. B., Herz, L. M. ‘Air-Degradation Mechanisms in Mixed Lead-Tin Halide Perovskites for Solar Cells’. *Advanced Energy Materials*, **2023**, 13(33), 2200847.
- **Lim, V. J. -Y.**, Righetto, M., Yan, S., Patel, J. B., Siday, T., Putland, B., McCall, K. M., Sirtl, M. T., Kominko, Y., Peng, J., Lin, Q., Bein, T., Kovalenko, M., Snaith, H. J., Johnston, M. B., Herz, L. M. ‘Contrasting Ultra-Low Frequency Raman and Infrared Modes in Emerging Metal Halides for Photovoltaics’. *ACS Energy Letters*, **2024**, 9, 41274135
- Righetto, M., Caicedo-Dávila, S., Sirtl, M. T., **Lim, V. J. -Y.**, Patel, J. B., Egger, D. A., Bein, T., Herz, L. M. ’Alloying Effects on Charge-Carrier Transport in Silver–Bismuth Double Perovskites’. *The Journal of Physical Chemistry Letters*, **2023**, 14(46), 10340-10347.
- Kamaraki, C., Klug, M. T., **Lim, V. J. -Y.**, Zibouche, N., Herz, L. M., Islam, S., Case, C., Perez, L. M., ’Charting the Irreversible Degradation Modes of Low Bandgap Pb-Sn Perovskite Compositions for De-Risking Practical Industrial Development’. *Advanced Energy Materials*, **2024**, 14(10), 2302916.

List of Abbreviations

CCD	Charge-coupled device
CW	Continuous wave
FA	Formamidinium $CH(NH_2)_2$
FTIR	Fourier-transform infrared
FWHM	Full width at half maximum
HTL	Hole-transport layer
IR	Infrared
LO	Longitudinal-optical
MA	Methylammonium CH_3NH_3
MHP	Metal-halide perovskite
ND	Neutral-density
OAP	Off-axis parabolic mirror
OPTP	Optical-pump–THz-probe
PCE	Power conversion efficiency
PL	Photoluminescence
PLQY	Photoluminescence quantum yield
PMMA	Polymethyl methacrylate
PTAA	Poly(triaryl amine)
TCSPC	Time-correlated single-photon counting
TDS	Time-domain spectroscopy
THz	Terahertz
TO	Transverse-optical
TRPL	Time-resolved photoluminescence
ULF	Ultra-low frequency
XRD	X-ray diffraction

1

Introduction

Greenhouse gas emissions from human activities have led to rising global surface temperatures.[1] This phenomenon, known as climate change, has already caused extreme weather conditions, irreversible damage to ecosystems, and reduced water and food security.[1] In order to slow down and eventually stop climate change, a worldwide energy transition from fossil fuels to renewable energy is paramount. Solar photovoltaics have been the fastest-growing source of renewable energy in recent years,[2] and are expected to be a major contributor to global renewable energy production over the next decade.[3]

The power conversion efficiency of crystalline silicon, currently the dominant semiconductor for solar photovoltaics, has slowed down in recent years.[4] However, novel materials have emerged and been subject to intense research over the past few decades, including organic, kesterite and quantum dot materials.[4,5] Of those novel emerging materials, metal-halide perovskites (MHPs) are particularly promising, and their power conversion efficiencies when implemented in solar cells have overtaken that of crystalline silicon.[4]

This thesis focuses on MHPs, especially on their fundamental photophysics and structural dynamics.

Thesis Overview

In Chapter 2, I briefly outline the concepts in fundamental physics relevant to the work presented in this thesis, and provide a literature summary of MHPs. I first explain the fundamental semiconductor physics concepts using a tight-binding model, where electronic bands are derived. Similarly, concepts in lattice vibrations using monatomic and diatomic chains are also explained. Later, I present a literature review of metal-halide perovskites, focusing on their structure and photophysics.

Chapter 3 introduces and explains different experimental techniques that were used in the work presented in this thesis. The working principles and experimental implementation are discussed. The techniques covered are absorption spectroscopy, photoluminescence (PL), X-ray diffraction (XRD), terahertz spectroscopies, and ultra-low frequency Raman spectroscopy.

Chapter 4 is the first chapter with experimental results in this thesis. In this chapter, XRD and PL were used in-situ to understand the halide anion segregation phenomenon in mixed-halide MHPs under illumination. More specifically, the effects of a hole-transport layer, as well as an ionic additive passivation agent, on such halide segregation were investigated. This work revealed that PL cannot be reliably used on its own to study halide segregation, especially with the presence of a charge-transport layer.

Chapter 5 investigates the degradation mechanisms of tin-only and mixed lead-tin iodide perovskites in ambient air. Photophysical, as well as structural, changes occurring during degradation in these materials were studied. It was revealed that these MHPs with different B-site metal cation compositions undergo degradation through contrasting mechanisms. Namely, tin-only iodide perovskites suffer from heavy p-doping from shallow defect state formation, but mixed lead-tin perovskites do not exhibit any significant doping during degradation. Instead, mixed lead-tin perovskites undergo degradation through deep defect state formation. To conclude this study, I suggest that different and more specific passivation techniques might be needed for mixed lead-tin perovskites.

Chapter 6 studies low-frequency vibrational properties of MHPs. MHPs exhibit a very broad response towards zero frequency in Raman spectra, but such broad response is not visible in the IR spectra. The exact origin of this phenomenon is still under debate in literature, positing numerous hypotheses. In this chapter, I systematically reviewed and assessed different hypotheses by contrasting the Raman and IR spectra of different metal-halides. I was able to rule out many hypotheses, and I suggested an alternate explanation for this phenomenon and for the apparent discrepancy between Raman and IR spectra of these materials.

In Chapter 7, I summarise the work presented earlier in the thesis, and outline its implication for future research. Additionally, Appendices A, B and C provide supplementary discussions and data for Chapters 4, 5 and 6, respectively.

2

Background and Fundamentals

Contents

This chapter outlines some the fundamental physics concepts relevant to the work presented in this thesis, as well as the background and motivation for the studies. I will outline the fundamental concepts of semiconductor physics in Section 2.1, and that of lattice vibrations in Section 2.2. The background of the metal-halide perovskite research field is summarised in Section 2.3, and charge-carrier dynamics of metal-halide perovskites are discussed in Section 2.4.

2.1 Band Theory of Solids

I briefly outline the theory behind the electronic structure of a solid state material, especially of a semiconductor. Different approaches can be taken to derive the formation of electronic bands, for example the nearly-free electron model, but I take the tight-binding model approach in this chapter as a demonstration.

Tight-Binding Model

First, consider a chain of atoms, each with a single orbital, with periodic boundary conditions. The orbital of the atom n can be written as $|n\rangle$, and orthonormality of these orbital wavefunctions can be assumed, namely $\langle n|m\rangle = \delta_{nm}$. A general wavefunction can be taken as:

$$|\psi\rangle = \sum_n \phi_n |n\rangle, \tag{2.1}$$

which is a Linear Combination of Atomic Orbitals (LCAO).

The Hamiltonian can be written as:

$$H = K + \sum_j V_j \tag{2.2}$$

where $K = \mathbf{p}^2/2m$ is the kinetic energy term, $\mathbf{p}$ and m are the momentum and the mass of the electron, and V_j is the potential term from Coulombic interaction between the electron at $\mathbf{r}$ and the j^{th} nucleus. Therefore,

$$H = (K + V_m) + \sum_{j \neq m} V_j = H_{\text{atomic}} + \Delta U \tag{2.3}$$

where H_{atomic} is the Hamiltonian of an isolated atom, and ΔU is the correction deriving from the Coulombic interactions, which is assumed to be small. Bloch's theorem dictates that the wavefunction in a crystal is:[6–8]

$$\psi(\mathbf{r} + \mathbf{R_n}) = e^{i\mathbf{k}\cdot\mathbf{R_n}} \psi(\mathbf{r}) \tag{2.4}$$

where $\mathbf{k}$ is the wavevector, and $\mathbf{R}_n$ is a translational vector of the lattice. Requiring normalisation conditions, the wavefunction can be shown to be:[6–8]

$$\psi(\mathbf{r}) = \frac{1}{\sqrt{N}} \sum_j e^{i\mathbf{k}\cdot\mathbf{r_j}} \phi(\mathbf{r} - \mathbf{r}_j) \tag{2.5}$$

where N is the number of atoms in the chain, and ϕ is the atomic orbital. Using this wavefunction and the Schrödinger's equation, the dispersion of the band can be shown to be:

$$E = E_0 - 2t \cos ka \tag{2.6}$$

where $E_0 = E_{\text{atomic}} + V_0$. E_{atomic} is the energy of an electron on an isolated atom, i.e.

$$H_{\text{atomic}} |m\rangle = E_{\text{atomic}} |m\rangle \tag{2.7}$$

and V_0 and t are given by matrix elements of V_j

$$\sum_{j \neq m} \langle n | V_j | m \rangle = \begin{cases} V_0 & n = m \\ -t & n = m \pm 1 \\ 0 & \text{otherwise} \end{cases} \tag{2.8}$$

In summary, the tight binding model can successfully describe the electronic states of an array of atoms each with a discrete energy level transitioning into a continuous energy band. This can be extended to include multiple energy levels within an atom, which would then result in multiple energy bands, separated by energy gaps.[6–8]

2.2 Lattice Vibration of Solids

In this section, I briefly outline the lattice vibration using a model system of a one-dimensional monatomic chain, and generalise it to a one-dimensional diatomic chain.

Consider a model system of an infinite one-dimensional diatomic chain of mass m with spring constant k between them, and the unit cell length a, as illustrated in Figure 2.1 (a). If the displacement of the nth atom is written as u_n, the force exerted on the n^{th} atom is given by:

$$F_n = k(u_{n+1} - u_n) + k(u_{n-1} - u_n) \tag{2.9}$$

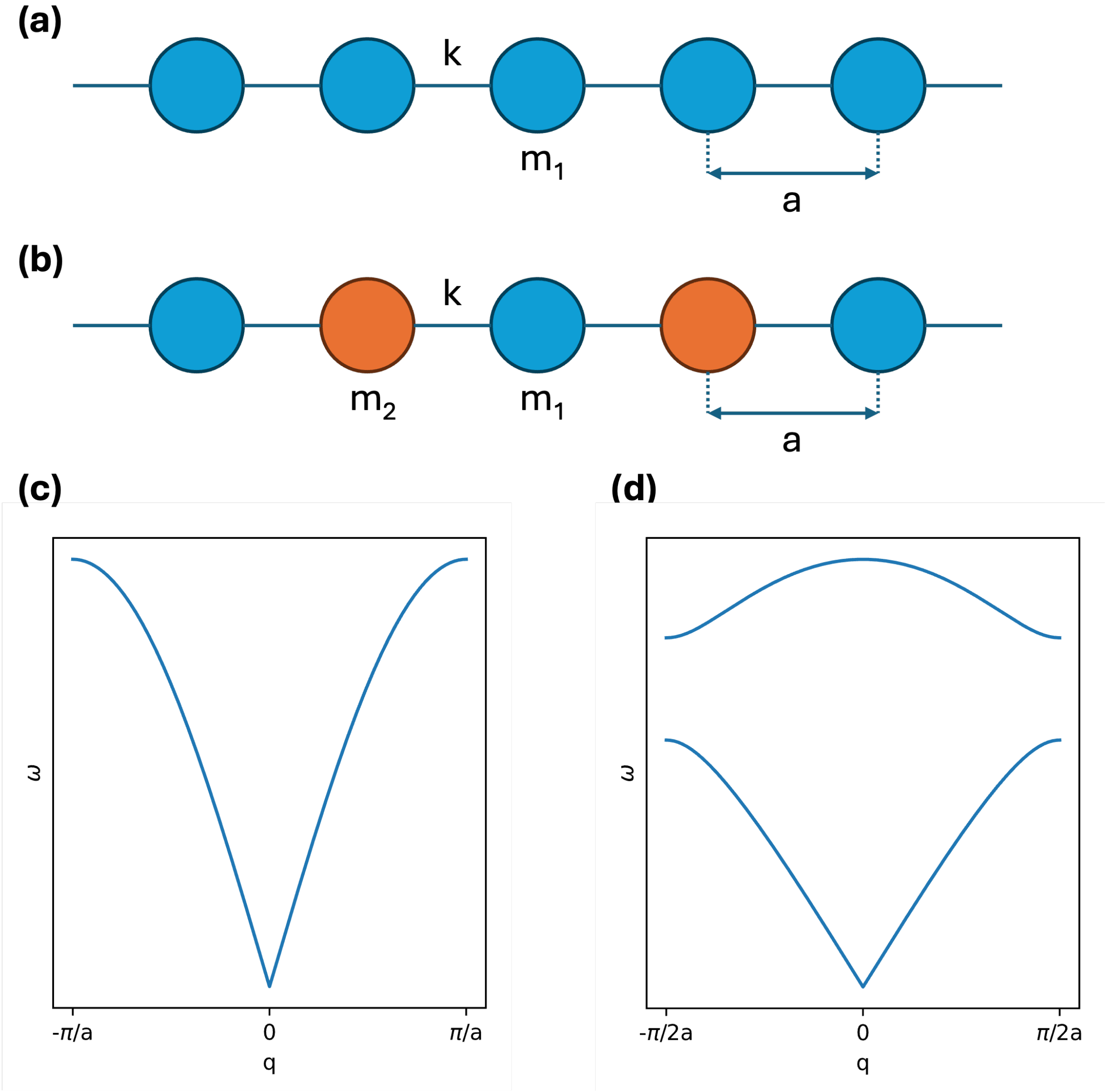

Figure 2.1: (a) One-dimensional monatomic chain, each particle of mass m_1 and spring in between with spring constant k. (b) One-dimensional diatomic chain of particles of alternating m_1 and m_2 masses with springs with spring constant k. (c) Dispersion relation of a monatomic chain. (d) Dispersion relation of a diatomic chain.

Using Newton's second law of motion,

$$M\frac{d^2u_n}{dt^t} = F_n = k(u_{n+1} - u_n) + k(u_{n-1} - u_n) = -k(2u_n - u_{n+1} - u_{n-1}) \tag{2.10}$$

This can be solved using an ansatz of the form:

$$u_n = A \exp i(qx_n - \omega t), \tag{2.11}$$

where x_n is the equilibrium position of the n^{th} atom, so $x_n = na$. This ansatz represents a travelling wave with an angular frequency of ω with an amplitude of A and wavevector q. The solution of this equation of motion gives us the dispersion relation:

$$\omega = 2\sqrt{\frac{k}{m}}\left|\sin\left(\frac{qa}{2}\right)\right|, \tag{2.12}$$

which is plotted in Figure 2.1 (c). For a diatomic chain of alternating masses m_1 and m_2 (Figure 2.1 (b)), the dispersion relation can be shown to be:[6,7]

$$\omega^2 = k\left(\frac{1}{m_1} + \frac{1}{m_2}\right) \pm k\sqrt{\left(\frac{1}{m_1} + \frac{1}{m_2}\right)^2 - \frac{4\sin^2 qa/2}{m_1 m_2}}, \tag{2.13}$$

which is plotted in Figure 2.1 (d). Transitioning from a monatomic chain to a diatomic chain, an introduction of different branches can be observed. The upper branch is called the optical branch, and the lower the acoustic branch. Only the optical branch, defined as a branch having non-zero frequency at zero wavenumber (Brillouin zone center), can directly couple to the electric field of a light wave due to momentum and energy conservation laws. This approach can be further extended into three dimensional crystals, giving multiple branches in different directions. In three dimensions, optical modes can also be divided into transverse optical (TO) and longitudinal optical (LO) phonon modes, depending on the relative direction of vibration and propagation.

Lattice vibration described so far can also be quantised to introduce a quasiparticle called a phonon, which is the quantum of vibration. Out of the optical phonons, which can interact with photons, only a subset will be active in infrared (IR) measurements (experimental implementation described in Section 3.2) and/or Raman measurements (described in Section 3.3), depending on the symmetry of the phonon modes; if the vibration changes the dipole moment of the lattice, it is IR-active, and if it changes the polarisability, it is Raman-active.

2.3 Metal-Halide Perovskites

Metal-halide perovskites (MHP) are a promising class of semiconductors for the next-generation solar cells and light-emitting devices applications. These materials have made rapid progress over the last decade, with current record power conversion efficiency (PCE) and external quantum efficiency exceeding 26% and 20% respectively.[4,9] What make MHPs such a promising class of materials are their optoelectronic performance and flexibility, as well as their low cost and facile fabrication methods.[10] Particularly, the bandgap of MHPs can be easily tuned by modifying the chemical composition, which is ideal for LED applications for tuning the emission wavelength, and for tandem solar cells where the overall PCE is highly dependent on the bandgap, E_{g}, of each layer.[11,12] The absorption coefficient of MHPs are also very high,[13] due to their bandgap being direct, which does not require phonon interaction for interband excitation. However, there still are challenges to be overcome before a commercial success for MHPs, the biggest one being their instability under oxygen, humidity or light.[14–16]

The perovskite structure is defined by the chemical formula ABX_3. For MHPs, the A cation is usually methylammonium (MA, $CH_3NH_3{}^+$), formamidinium (FA, $CH(NH_2)_2{}^+$), or caesium (Cs^+), the metal B cation lead (Pb^{2+}) or tin (Sn^{2+}), and the halide X anion bromide (Br^-), iodide (I^-) or chloride (Cl^-), or a mixture thereof.[13] The perovskite structure is shown as a unit cell in Figure 2.2; the idealised crystal structure is cubic, with the smaller B cation at the centre, surrounded by an octahedra formed by the halide X ions, and the larger A cations lie on the corners of the unit cell. Each of the

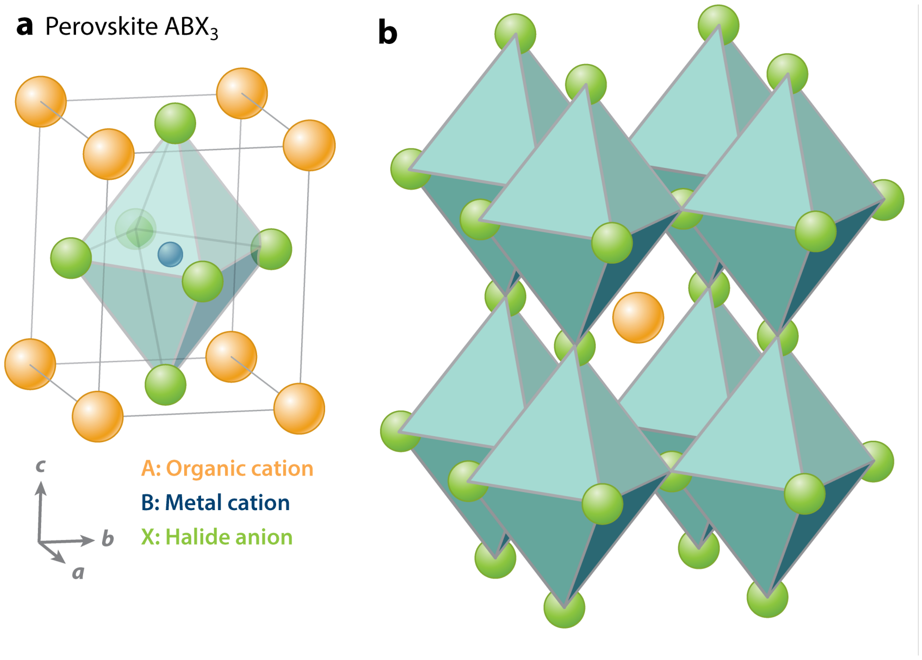

Figure 2.2: (a) Perovskite unit cell. (b) Representation of the perovskite structure in terms of corner-sharing octahedra. Figure reprinted with permission from Reference [13]. Copyright (2016) Annual Reviews.

A-,B- or X-sites of the perovskite ABX_3 can be varied in composition, including mixing of two or more species. Different sites have different effects on the properties of the MHPs, with particular interests on stability and bandgap tuning.[15] For a given choice of the composition, the Goldschmidt tolerance factor $t = \frac{R_A+R_B}{\sqrt{2}(R_X+R_B)}$, where R_A, R_B and R_X are the ionic radii of the A-,B- and X-sites, can be used to estimate whether the material will form a stable (pseudo-)cubic perovskite structure.[17]

2.3.1 Band Structure

In MHPs, the valence band maximum (VBM) is mostly consisted of the anti-bonding of p-orbitals of the X-site halide ions and the s-orbitals of the B-site metal ions.[13,18,19] The conduction band minimum (CBM) is dominated by the p-orbital of the B-site metal ion.[13,18,19] Both VBM and CBM occur at the Γ-point in the momentum space, resulting in a direct bandgap.[19,20] As mentioned above, MHPs have higher absorption coefficients compared to materials like silicon with an indirect bandgap, but its absorption coefficients are higher than other III-V semiconductors with a direct bandgap too.[18,19] This is because of the band-to-band optical transitions in MHPs being a p-p transition, while the transition being p-s transition in III-V semiconductors, leading to a higher joint density of states for MHPs.[18,19] Also, the heavy nature of the B-sit metal ions, there is a strong spin-orbit coupling in MHPs, leading to a reduction in the bandgap, as well as a splitting in the conduction band.[13,19]

2.3.2 A-site Cation Variation

$MAPbI_3$ has been initially used as the benchmark composition for perovskites, but MA-only perovskites has been less popular for device fabrication due to its thermal instability.[21] The bandgap can be affected by the composition of the A-site via distorting the lattice structure,[22] but the A-site is usually used to optimise for stability. Alloying two or even three A-site cations has been shown to improve device performance, crystallinity and stability.[23–25]

2.3.3 B-site Metal Cation Variation

Pb-based perovskite devices have been best performing regarding B-site choice, but there are health and environmental concerns over the usage of toxic Pb, which encourages total or partial replacement of Pb.[26] Potential candidates include germanium based halide perovskites, double perovskites, and Sn-based perovskites, but the former two have shown worse solar cell performances compared to the last.[27]

Sn-based perovskites are the most promising class of Pb-free perovskite, with the highest demonstrated PCE of over 14%.[28] However, Sn-based perovskites suffer from severe air instability, and undergoes Sn vacancy formation and Sn^{2+} oxidation to Sn^{4+} when exposed to air, resulting in p-doping of the material.[12,29,30] As a way to mitigate such self p-doping, SnF_2 additives have been routinely used in the literature.[31–34] SnF_2 passivates Sn defects and suppresses Sn vacancy hole formation by creating a tin-rich environment, resulting in reduced background hole density.[31–34]Accordingly, the use of SnF_2 has been linked to improved the optoelectronic properties, including longer PL lifetimes, decreased energy disorder and higher charge carrier mobilities.[32,33]

Pb-Sn Perovskites

Mixed Pb-Sn perovskites exhibit a bandgap bowing behaviour, where the bandgap of the alloy is lower than that of all-Pb or all-Sn parent materials; this makes Pb-Sn perovskites an ideal candidate for the bottom subcell in all-perovskite tandem solar cells.[33,35–37] This bowing behaviour is expressed in the following equation:

$$E(x) = E_1 x + E_2(1 - x) + bx(1 - x), \tag{2.14}$$

where $E(x)$ is the bandgap of the alloy between tin- or lead-only materials of bandgaps E_1 and E_2, and x is the mixing ratio between the two. The first two terms are a linear interpolation between the two materials, known as the Vegard's law, and the last term represents a quadratic bowing behaviour, where b is the bowing parameter.[32,38] Such bandgap bowing behaviour has been attributed to bond bending.[36,37] Mixed Pb-Sn perovskites have been reported to exhibit superior device performances compared to Sn-only perovskites, with the PCE exceeding 23%,[39,40] as well as better stability.[40,41]

2.3.4 X-site Halide Anion Variation

X-site alteration has a significant impact on the bandgap of perovskite, due to the different energies of the halide orbital involved in the B-X bond.[42] Cl-Br and Br-I alloying is possible, with the latter providing a more attractive bandgap for tandem applications.[12,15] By altering the X-site composition, the bandgap of MHPs can be tuned across the entire visible spectrum by altering the X-site composition.[43,44]

2.3.4.1 Halide Segregation

Despite Br-I mixed halide perovskites offering an attractive bandgap for photovoltaic application, they possess a compositional instability known as halide segregation, where the perovskite material segregates into spatially separated iodide-rich and bromide-rich regions under illumination.[15,16] Since the iodide-rich regions possess lower bandgap compared to the original mixed iodide-bromide material,[16,43,45] excited charge carriers funnel into the low-bandgap iodide-rich regions to minimise energy, and therefore halide segregation results in a red-shift of the photoluminescence spectra.[16] These iodide-rich regions possess a higher VBM and a similar CBM compared to the mixed phase, therefore holes are more susceptible to funneling, after which electrons follow because of Coulomb interaction.[46–49] Halide segregation is reversible, such that the material mixes back into its original homogeneous distribution when left in the dark.[16] It is now widely believed that excited charge carriers initiate halide segregation, given halide segregation is still observed under charge-carrier injection without any photoexcitation, but the exact explanation remains under debate.[15,50–52] Halide segregation has a detrimental effect on the performance of perovskite solar cells; charge-carrier funnelling causes the radiative recombination to be accelerated, lowering the open-circuit voltage[53–56] and current extraction efficiency.[50,52] X-ray diffraction (XRD) measurements suggest that only a small fraction undergoes halide segregation, but PL measurements are affected more dramatically, also due to charge-carrier funnelling.[15,16,57]

There have been various attempts to suppress halide segregation in perovskites. Certain compositions of the perovskites have proven to be more resistant to halide segregation; for example, perovskites with FA and Cs at the A-sites have been observed to undergo halide segregation over much longer timescales than MA-only counterparts,[15,57] and the FA to Cs ratio is also observed to affect the stability.[24] The stability is also influenced by the X-site composition, and the compositions near the central range (i.e.

50% of each halide) are particularly unstable.[15,16] This limits the range of stable X-site composition, and therefore the bandgap, which does not exhibit halide segregation, without further suppression techniques.

Low energetic barriers against halide ion movement in MHPs,[58,59] especially along grain boundaries,[60–62] have been reported to promote halide segregation. Stabilising against halide segregation was achieved by different trap passivation techniques in various studies.[63–66] The amount of trap-mediated charge-carrier recombination has also been correlated to the rate of halide segregation.[57,67,68] The electric field generated by charge carriers localised in trap states has therefore been suggested as a cause of halide segregation as an explanation.[69] Consequently, suitable trap passivation has been suggested as a viable way to stabilise MHPs against halide segregation.[15] There are other explanations in the literature for the possible mechanisms of halide segregation, namely thermodynamic,[46,70] polaronic[71,72] and redox models.[73–75]

2.3.5 Solar Cell Operation

Initially, MHP solar cells used the sensitised architecture where MHP-coated mesoporous TiO_2 was used as the photoactive layer,[76] but thin-film based architecture has become more popular.[10,13,77] In a thin-film MHP solar cell, the MHP absorber layer is positioned between an electron-transport layer (ETL) and a hole-transport layer (HTL), which are then connected to metal contact layers.[13,78] After photoabsorption of the MHP layer, photoexcited electrons and holes are separated and are transported respectively into the ETL and HTL.[10,13,78] The band alignment of ETL and HTL with respect to the MHP prevents the unwanted charge-carrier species from entering the transport layers.[78] These charge carriers are then transported into the contacts, before being extracted out of the device for electrical power output.

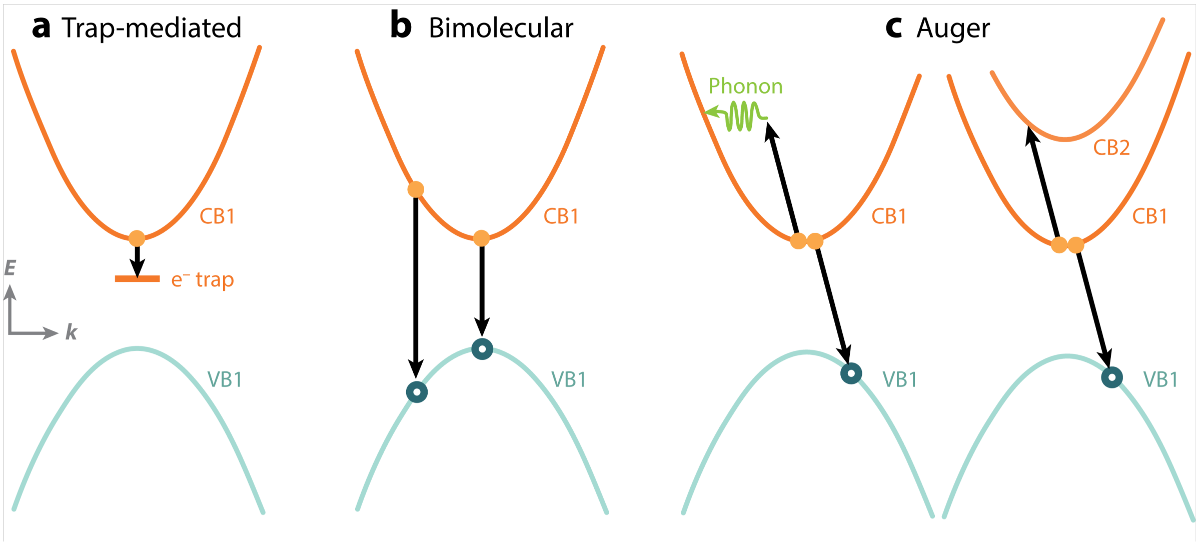

Figure 2.3: Schematic band diagrams denoting different charge-carrier recombination mechanisms. Figure reprinted with permission from Reference [13]. Copyright (2016) Annual Reviews.

2.4 Charge-Carrier Dynamics

Charge-carrier dynamics and their lifetimes are fundamental to optoelectronic device operation. The charge-carrier lifetime limits the time available for charge extraction for solar cell applications. MHPs are shown to have low charge-carrier recombination rates, ideal for solar cell applications.[79] A general rate equation for charge-carrier recombination describing changes in the free charge-carrier density $n(t)$ that has been shown to be applicable to MHPs is:[13]

$$\frac{\mathrm{d}n}{\mathrm{d}t} = -k_3 n^3 - k_2 n^2 - k_1 n, \tag{2.15}$$

where k_1, k_2 and k_3 are the monomolecular, bimolecular and Auger recombination rates, respectively. These recombination processes are schematically shown in Figure 2.3.

Monomolecular Recombination

First-order recombination can occur via two different pathways: recombination of an exciton, and by a trap-mediated process. The former is considered monomolecular if the excitonic quasiparticle state is already formed. However, most excitons are dissociated in MHPs at room temperature because their exciton binding energy is comparable to or lower than the thermal energy at room temperature,[13] making the latter the dominant process. This is also known as Shockley-Read-Hall recombination, which is usually non-radiative.[13] However, if there is a high background density of charge carriers from doping, pseudo-monomolecular recombination can occur, which may be radiative.[80]

Bimolecular Recombination

Bimolecular recombination occurs when a free electron in the conduction band recombines with a free hole in the valence band, and is the primary radiative recombination pathway. Since band-to-band bimolecular recombination is the inverse process of photoexcitation through photon absorption, k_2 can be accurately from the principle of detailed balance.[20] Although k_2 is a fundamental intrinsic material property, there are variations within the literature for the reported values. The variation may be due to reabsorption effects, masking the true intrinsic value, and lowering the apparent values.[81]

Auger Recombination

In Auger recombination, a conduction band electron recombines with a valence band hole, but excess energy and momentum are transferred to another electron or hole in order to comply with energy and momentum conservation laws. This is a non-radiative process, and only observable at very high excitation fluences.[13] Therefore, this process is irrelevant for normal solar cell operation, but it may be important for solar concentrators[82] or LED applications where charge-carrier densities are necessarily high.[83]

Trap states and Defects

Trap states and defects give rise to monomolecular recombination, but k_1 may be spatially or temporally varying, due to its dependence on the density of unfilled traps and inhomogeneous distribution of defects, which can result in stretched exponential decays.[33,36] Frenkel defects, where an ion leaves its site to become an interstitial and create a vacancy, are the main type of defects in MHPs, and this type of defects can introduce sub-bandgap trap states.[84] Defect densities are also shown to be higher near grain boundaries and surfaces.[85,86] MHPs are defect tolerant, possessing mostly shallow trap states, which helps to maintain excellent device performances even with high defect densities.[87,88] However, trap states do have adverse effects, including increased k_1 and decreased open-circuit voltage.[89] The sub-bandgap states formed due to defects and disorder can be quantified by Urbach energy, E_U, at the band edge, where a high Urbach energy indicates high energetic disorder:[90,91]

$$\alpha = \alpha_0 e^{(E-E_\mathrm{g})/E_\mathrm{U}}, \tag{2.16}$$

where α is the absorbance, E the photon energy, and E_g the bandgap.

3

Experimental Theory and Methods

Contents

In this chapter, I explain the details and working principles of the experimental techniques and analysis carried out for the work presented in this thesis.

3.1 Absorption Spectroscopy

Absorption spectroscopy can give insights into the electronic structure of the material under investigation. Absorption of electromagnetic waves, or photons, can cause different transitions within the material, depending on the energy of the excitation. Most of the absorption measurements presented in this thesis focus on the visible and near-infrared regime. For the semiconductors under investigation, excitation in this range can cause electrons in the valence band to be photoexcited to the conduction band, and information about the electronic bandgap (E_g) and exciton binding energy (E_b) can be extracted from the absorption spectra.

Experimentally, absorption spectra are acquired through a technique called Fourier-Transform Infrared spectroscopy (FTIR) - for the absorption spectra presented in this thesis, a Bruker Vertex 80v FTIR spectrometer was used. A schematic diagram is depicted in Figure 3.1, where the light source is split by a beamsplitter, and one branch reflects off a stationary mirror, and the other off a movable mirror. These two branches then recombine and interfere, and the combined path goes through the sample under investigation. After the light has passed through the sample, the intensity of the transmitted light is measured by a detector. The apparatus used in this thesis was set up such that the transmission through the sample and the reflection off the sample can both be measured by a simple change in configuration. By measuring both transmission and reflection, the absorption of the sample can be better determined. The transmission and reflection spectra have to be calibrated, so a metallic mirror and the sample substrate were used as references for reflection and transmission measurements, respectively.

This apparatus can be used to determine the absorption spectrum across different spectral ranges by changing the source, detector, beamsplitter and the reference mirror accordingly. Namely, for the near-infrared and visible range used in the thesis, a tungsten filament lamp was used as the source, CaF_2 as the beamsplitter, a silicon photodiode as the detector, and a silver mirror as the reflection reference mirror.

Absorbance was then calculated using:

$$A = -\ln \frac{T}{1-R}, \tag{3.1}$$

where A is the absorbance, T is the transmission, and R is the reflectance.

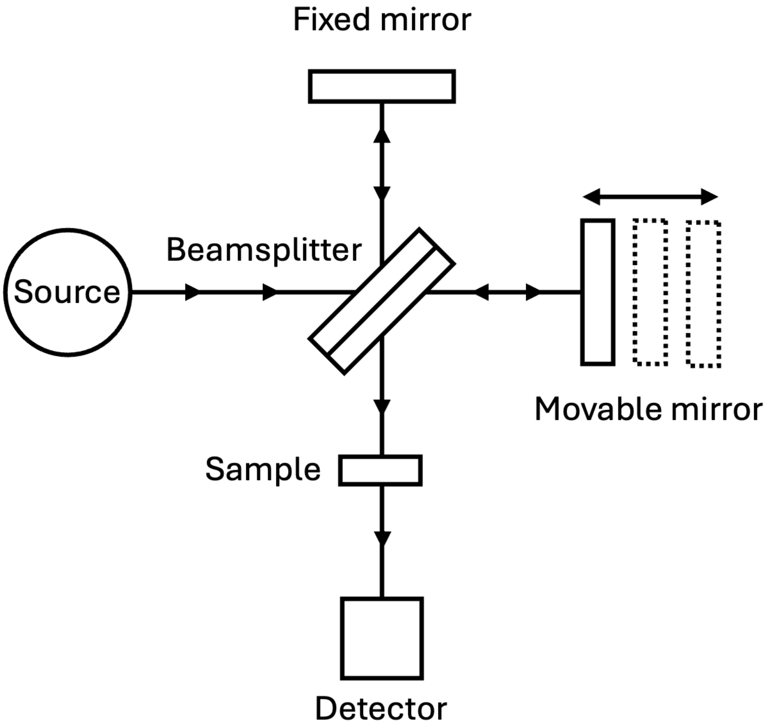

Figure 3.1: A schematic of a Fourier-Transform Infrared (FTIR) absorption experiment.

3.1.1 Elliott Fitting

Absorbance spectra can be fitted with an expression derived from Elliott theory describing the absorption of a semiconductor in the presence of Coulomb correlations.[92] This has been done for Chapter 5, in a similar manner to previous reports.[20,92,93] This fitting allowed me to attribute the changes in the absorbance observed during degradation to both the blueshift of bandgap arising from the Burstein-Moss effect, and the decrease of the exciton binding energy caused by screening resulting from unintentional electrical doping.

The absorption given by the Elliott model is:

$$\alpha(E) = \alpha_{\mathrm{X}}(E) + \alpha_{\mathrm{C}}(E) \tag{3.2}$$

where α_X is the exciton and α_C is the continuum contribution to the absorbance. The exciton contribution is given by:

$$\alpha_{\mathrm{X}}(E) = \frac{b_0}{E} \sum_{n=1}^{\infty} \frac{4\pi E_{\mathrm{b}}^{\frac{3}{2}}}{n^3} \delta\left(E - \left[E_{\mathrm{g}} - \frac{E_{\mathrm{b}}}{n^2}\right]\right) \tag{3.3}$$

where the electric dipole transition matrix element between the conduction and the valence bands is incorporated in the proportionality constant b_0. E_b is the exciton binding energy, E_g is the bandgap, and n is the quantum number of the exciton. The electron-hole continuum contribution is given by:

$$\alpha_\mathrm{C}(E) = \frac{b_0}{E}\left[\frac{2\pi\sqrt{\frac{E_\mathrm{b}}{E-E_\mathrm{g}}}}{1-\exp\left(-2\pi\sqrt{\frac{E_\mathrm{b}}{E-E_\mathrm{g}}}\right)}\right] c_0^{-1}\mathrm{JDoS}(E) \tag{3.4}$$

where the joint density of states $\mathrm{JDoS} = \frac{c_0}{1-b(E-E_\mathrm{g})}\sqrt{E-E_\mathrm{g}}$ for $E > E_\mathrm{g}$, and 0 otherwise, where b is the band non-parabolicity factor,[94] and $c_0 = \frac{2}{(2\pi)^2}\left(\frac{2\mu}{\hbar^2}\right)^{3/2}$, where μ is the reduced effective mass of the electron-hole system. A Gaussian broadening was also introduced by convolving $\alpha(E)$ with a normal distribution $N(0, \Gamma^2)$.

3.2 Photoluminescence

Photoluminescence (PL) measures the radiative recombination of excited charge carriers after photoexcitation. Electrons in the conduction band relax down to the conduction band minimum (CBM) after photoexcitation, and they can recombine with holes at the valence band maximum (VBM), emitting photons; there are other processes through which they recombine, as explained in Section 2.4. These emitted photons can have a distribution of energy, giving a spectrum, which can be investigated using steady-state PL (SSPL) (Section 3.2.1), or the temporal dynamics of how the PL intensity changes in time can be investigated in time-resolved PL (TRPL) (Section 3.2.2). TRPL can therefore give information about photoexcited charge-carrier dynamics, including their lifetimes. Time-dependent PL with wavelength resolution can also be acquired, and this is called time-resolved emission spectra (TRES) measurements.

3.2.1 Steady-State Photoluminescence

For a steady-state photoluminescence (SSPL) experiment, typically a continuous-wave (CW) laser is used as the excitation source, which is focused onto the sample. The excitation source should have an energy higher than the bandgap in order to photoexcite the semiconductor sample under investigation. The sample will then photoluminesce, and this signal is collected with collection optics. Not all of the light is absorbed by the sample and some of the excitation source light is scattered, so a spectral filter is used to block the excitation light and only collect and measure the PL from the sample. After collection, the PL signal is spectrally resolved using a spectrometer with a diffraction grating. Typically, once the signal is resolved, a charge-coupled device (CCD) is used to detect the PL spectrum.

3.2.2 Time-Resolved Photoluminescence

There are a number of ways to detect the photoluminescence signal with time resolution, namely with a fast photodiode,[95] streak camera,[96] or upconversion technique[97]. In the work carried out in this thesis, I employed the time-correlated single-photon counting (TCSPC) method. In this method, the time between the generation of the light pulse (typically pulsed laser) from the source, and the detection of light (PL) is electronically measured. An electronic signal is split in two, and one generates a laser pulse that photoexcite the sample, and the other a precise timer, which is stopped once a photon is detected. This measurement takes place over multiple pulses, and it results in a histogram, which is representative of how long it takes for charge carriers to recombine and emit photons, i.e. PL dynamics. There are a number of considerations to be taken into account. Wrap-around is a phenomenon where charge carriers do not fully decay until the next excitation pulse arrives, and therefore increase the background of the signal. Pile-up is where the probability of multiple photons arriving in one cycle is too high; since the detector has a down-time, it can only detect the photon arriving first, so pile-up can artificially decrease the apparent charge-carrier lifetime.

For the work presented in this thesis, a pulsed diode laser (LDH-D-C-470, PicoQuant) was used as the excitation source, set at 1MHz repetition rate. The beam radius at the sample position was $\approx 0.1\,\mathrm{mm}$. The PL emission was collected in a reflection geometry and was coupled into a spectrometer (SP-2558, Princeton Instruments), before being detected by a single-photon avalanche-diode device (PDM, MPD). The excitation fluence was controlled with neutral density filters. The timing was electronically controlled using a PicoHarp300 event timer.

3.3 X-Ray Diffraction

X-ray diffraction (XRD) is an experimental technique that can be used to extract structural information about a crystal. The interference between different lattice planes result in interference patterns at specific geometries. In the simplest case, the Bragg equation dictates the condition under which the X-ray will be scattered:

$$2d\sin 2\theta = n\lambda, \tag{3.5}$$

where d is the distance between neighbouring lattice planes, 2θ is the angle between the incoming and scattered beams, n is an integer, and λ is the wavelength of the incoming X-ray. When this condition is satisfied, the diffracted X-ray interferes constructively, giving a maximum in the intensity of the measured signal. This can be generalised to three-dimensional crystals, so a full XRD pattern can be analysed to understand the crystallographic phase of the sample.

For all the wide-angle XRD measurements presented in this thesis, PANalytical X'Pert powder X-ray diffractometer with a Cu-K$_{\alpha 1}$ source was used. Minor sample tilt was corrected by applying a constant offset in 2θ by using a reference z-cut quartz substrate peak at $2\theta = 16.43°$

3.3.1 In Situ XRD/PL

A custom-built insert was employed, as reported previously by Knight et al.,[57] to measure concurrent, in situ XRD patterns and PL spectra, in order to observe both electronic and structural changes during halide segregation simultaneously. The setup consisted of an optical insert to a Rigaku SmartLab X-ray diffractometer, which consisted of illumination and PL collection optics. A fiber-coupled 470 nm diode laser (PicoQuant LDH-D-C-470, $190\,\mathrm{mW\,cm^{-2}}$ intensity, CW, beam radius $\approx$ 2 mm) was used as the illumination source, which was attached to the illumination optics of the insert using an optical fiber. The laser illumination was then launched into free space, directed at the sample. The beam was expanded with a lens, which was ensured to be larger than and overlap with the X-ray beam (beam radius $\approx$ 0.2 mm) from the X-ray diffractometer. The collected PL was coupled into a fibre, which was led out of the Rigaku SmartLab, and analysed using an Ocean Optics USB2000 spectrometer. The XRD measurements were taken with a HyPix-3000 2D X-ray detector, while the aforementioned optical insert was mounted into the Rigaku SmartLab diffractometer. The incident radiation used was the Cu-K_α line. The 2D detection sensor of the X-ray detector was used to capture a range of 2θ continuously without having to move any of the components, including the X-ray source, sample, or detector.

3.4 Terahertz Spectroscopy

Terahertz (THz) radiation can be very useful in investigating the electronic properties of a material. Free charge carriers, either photoexcited or doped, and IR-active phonon modes can absorb THz radiation. In order to study these, THz spectroscopy is used as a non-contact optical method of determining the THz conductivity of a material, either a spectrum without time resolution (Section 3.4.1), or a spectrum-averaged intensity with time resolution (Section 3.4.2). A schematic of the setup is shown in Figure

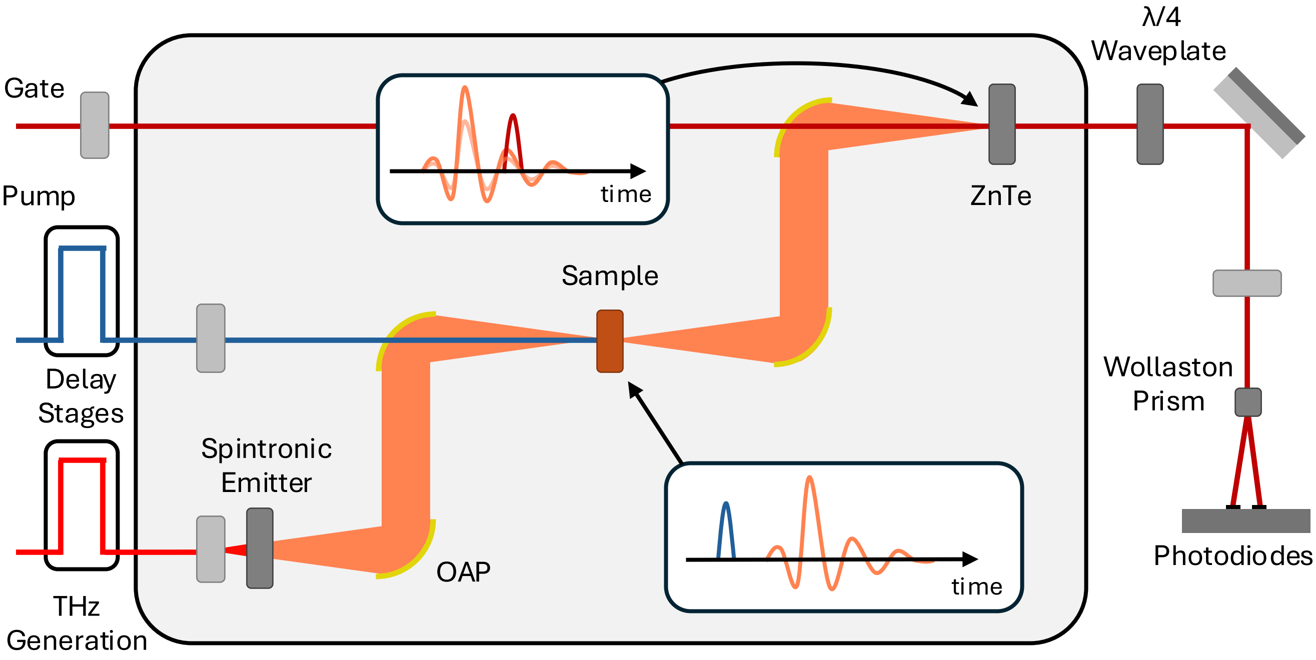

Figure 3.2: A schematic of the optical-pump terahertz-probe (OPTP) setup.

3.2. A titanium:sapphire regenerative amplified system was used in this setup. The oscillator (Maitai, SpectraPhysics) was amplified through a regenerative amplifier (Spitfire, SpectraPhysics) and a seed laser (Nd:YAG, Ascend, SpectraPhysics). The output of the system was pulsed at 5 kHz with a central wavelength of 800 nm and a pulse duration of ≈ 35 fs. The laser output is split into three beamlines, gate, pump and THz-generation lines. Two optical delay stages were used to independently delay the pump and THz generation beam with respect to the gate beam by mechanically adjusting the physical beam path length. The pump and the THz generation pulses were modulated to 1.25 kHz and 2.5 kHz respectively, using mechanical choppers.

THz pulses were generated using a spintronic emitter with a tri-layer structure (2 nm tungsten, 1.8 nm $Co_{40}Fe_{40}B_{20}$, 2 nm platinum on a quartz substrate), in between two permanent magnets.[98] When an ultrafast laser pulse is incident on the emitter, a net current flows from the ferromagnetic layer ($Co_{40}Fe_{40}B_{20}$, already under a magnetic field) to a non-magnetic layer (tungsten or platinum), and this current is also spin-polarised. This current undergoes inverse spin Hall effect originating from spin-orbit coupling, resulting in a deflection and therefore a current in a perpendicular direction to the laser propagation direction. This current is sufficiently short-lived, hence generating a THz pulse. The THz pulses propagate in a vacuum box, to avoid absorption by water molecules in the THz range. After THz generation, the THz pulses are then focused onto the sample using gold off-axis parabolic mirrors (OAPs), and the transmitted THz pulses are collected using another set of gold OAPs. The THz transmission is then focused onto a 1 mm-thick (110) ZnTe crystal for electro-optic sampling; this THz beam is overlapped with the gate beam both spatially and temporally within the crystal. The intensity of electric field of the THz radiation changes the birefringence of the ZnTe crystal due to Pockels effect, which changes the polarisation of the gate beam. Such change can be measured using a quarter-wave plate and a Wollaston prism, which separates the incoming light into two linearly polarised beams. The separated beams are detected using two balanced photodiodes. A home-made FPGA (field-programmable gate array) based data acquisition board was used to collect the data.

3.4.1 Time-Domain Spectroscopy

In THz Time-domain spectroscopy (TDS), THz pulses are used to probe the sample, and the amplitude and phase of the THz pulses are measured as a function of time using an optical delay stage, controlling the relative delay between the THz and gate beams. In this setup, the gate beam had a fixed beam path, while the beam path of the THz beam was modified. The measured time-domain transmission through the thin film was Fourier transformed, $\tilde{T}_{\text{sample}}$, and is compared to the transmission through the bare substrate, $\tilde{T}_{\text{substrate}}$. The following equation is used to calculate the dark conductivity spectrum of the thin film:[99–102]

$$\tilde{\sigma}_{\text{dark}} = \frac{\tilde{T}_{\text{substrate}} - \tilde{T}_{\text{sample}}}{\tilde{T}_{\text{sample}}} \times \frac{\epsilon_0 c(1 + n_{\text{substrate}})}{d}, \tag{3.6}$$

where $n_{\text{substrate}}$ is the refractive index of the substrate (2.1 for z-cut quartz)[103], d is the thickness of the thin film, and c and ϵ_0 are the speed of light in vacuum and vacuum permittivity, respectively. The thickness of the samples was measured using Dektak 150 Surface profiler.

3.4.2 Optical-Pump Terahertz-Probe

The terahertz transmission of thin films was measured at the peak of the electric field of the THz pulse for different delays of the pump beam for optical-pump terahertz-probe (OPTP) measurements, mapping the THz transmission as a function of time after photoexcitation. The pump beam was frequency-doubled from 800 nm to 400 nm with a 1 mm-thick beta barium borate (BBO) crystal (type 1). The pump beam radius was ≈ 2 mm, the radius of the THz beam was ≈ 0.3 mm at the sample position. The THz stage was first scanned in time with respect to the fixed gate beam to find the maximum THz transmission, before scanning with the delay stage for the pump beam. The photoconductivity of the thin-film sample is given by:[79]

$$\sigma = \varphi \frac{\epsilon_0 c}{d}(1 + n_{\text{substrate}}) \frac{\Delta T}{T}, \tag{3.7}$$

where φ is the photon-to-charge branching ratio, the fraction of photons being converted to free charge carriers, d is the thickness of the thin film, $n_{\text{substrate}} = 2.1$ is the refractive index of the substrate (z-cut quartz) at THz frequencies,[103] T is the THz transmission through the sample in the dark, ΔT is the difference in THz transmission between the photoexcited sample and the sample without any photoexcitation. ϵ_0 and c are the vacuum permittivity and speed of light in vacuum, respectively.

However, the high dark conductivity of tin-only MHPs investigated in Section 5 means that Equation 3.7 is no longer valid, and has to be modified by adding a higher order term.[33,99,100] The modified expression is:

$$\sigma = \left[\sigma_{\text{dark}} + \frac{\epsilon_0 c(1 + n_{\text{substrate}})}{d}\right] \frac{\Delta T}{T}, \tag{3.8}$$

where σ_{dark} is the DC Drude conductivity of the thin-film sample in the dark. σ_{dark} was extracted from THz-TDS measurements in Section 3.4.1.

Photoconductivity transients can be fitted with equations discussed in Section 2.4. However, in the study presented in Section 5, the fluences were low, and together with relatively large amounts of trap- or doping-assisted recombination in tin-iodide perovskites meant that I could assume that the recombination of photoexcited charge carriers is mostly monomolecular:

$$n(t) = Ae^{-k_1 t}, \tag{3.9}$$

where $n(t)$ is the charge-carrier density at time t after photoexcitation, k_1 is the monomolecular recombination rate, and A is a constant. Equation 3.9 was fitted to photoconductivity transients to extract k_1.

The charge-carrier sum mobility μ in the THz region can also be estimated with photoconductivity transients:

$$\sigma(t) = n(t)e\mu, \tag{3.10}$$

where σ can be substituted in from Equation 3.8, and e is the elementary charge. The charge-carrier density n at time $= 0$ can be estimated by:

$$n(t = 0) = \frac{E\lambda}{hcA_{\text{eff}}d}, \tag{3.11}$$

assuming perfect absorption of the photoexcitation by the sample, where A_{eff} is the effective overlap area between the pump and THz probe pulses, E is the energy of the photoexcitation pulse, λ is the wavelength of the photoexcitation, and h is the Plank constant. The effective overlap area was calculated using scanning knife edge measurements and fitting an error function to the transmission intensity of the THz and pump beams separately.

3.5 Ultra-Low Frequency Raman

When investigating the vibrational properties, absorption measurements described in Section 3.1 and 3.4.1 are only sensitive to IR-active modes. Therefore, in order to gain a more comprehensive understanding of the vibrational characteristics of a material, having complementary information from Raman-active modes is crucial. Ultra-low frequency Raman spectroscopy is also called THz-Raman spectroscopy since it measures the Raman response in the THz regime. This is particularly useful, given that the IR response in the same regime can be probed with THz-TDS (Section 3.4.1).

As part of my DPhil work, I built a new ultra-low frequency Raman setup, designing and ordering as well as setting up all components. A schematic of the setup is presented in Figure 3.3. This setup was built around a pre-existing PL setup, sharing the sample holder and the spectrometer, and hence the use of flip mirrors just before the sample and the spectrometer. All the filters were custom made by OptiGrate, with their central wavelength 900 nm. These filters are reflective volume-Bragg gratings, where there is a periodic modulation of the refractive index within the volume of the filter, and the reflection from this filter can be customised to have a very narrow linewidth at a specific wavelength.[104] The spectral bandwidth (FWHM) of the notch filters used is $5\,\text{cm}^{-1} \approx 0.15\,\text{THz}$, which determines the lowest Raman frequency accessible with these filters. The central wavelength of 900 nm was chosen as a compromise between the sensitivity of

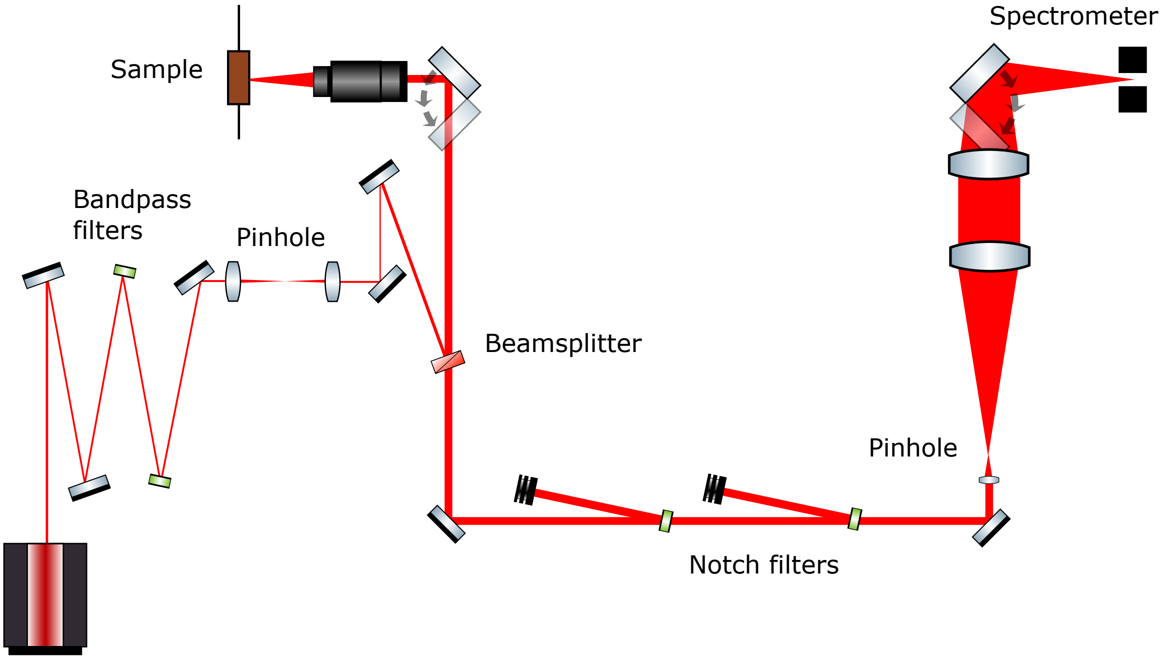

Figure 3.3: A schematic of the Raman setup, built around a pre-existing PL setup.

silicon CCDs, which decreases towards longer wavelengths, and the ability to perform below-bandgap Raman spectroscopy on MHPs, for which a longer wavelength is desirable. A SpectraPhysics 3900S titanium:sapphire tuneable CW laser was used as the excitation source, which was pumped with SpectraPhysics Millenia (532 nm). The central wavelength of the laser was set to 900 nm. The beam first goes through two bandpass filters to suppress spontaneous emission from the laser, in order to narrow the laser bandwidth, before being spatially filtered with a pinhole, to improve the spatial profile and to collimate the beam. Then, the beam is directed into a beamsplitter and reflected off it, then into a microscopic objective (Olympus LMPLFLN50x, 0.5 numerical aperture). The beam is focused onto the sample, and the Raman signal is collected in a back-scatter geometry. The collimated signal beam passes through the beamsplitter, and the Rayleigh elastic scatter is filtered out by two notch filters, before being spatially filtered. After this, the beam is focused into the spectrometer (Horiba iHR320), and detected with a 600 g mm^{-1} grating (central wavelength 750 nm) and a nitrogen-cooled silicon CCD.

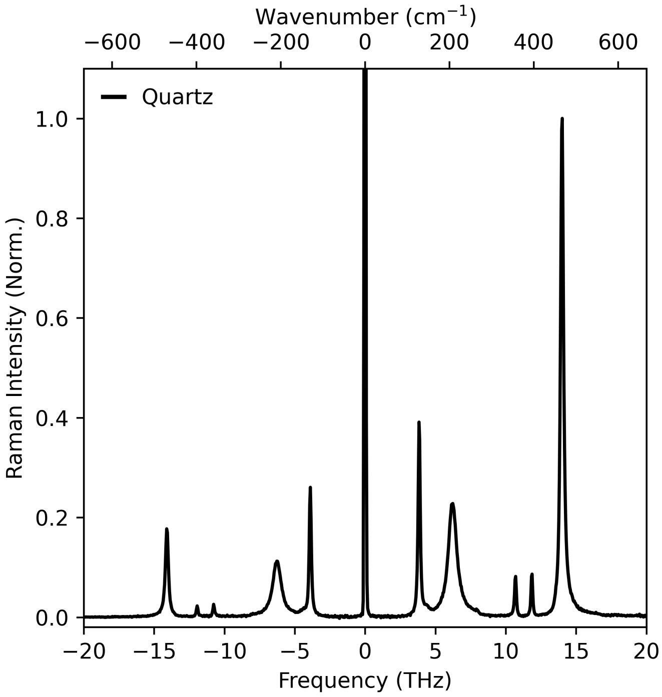

Figure 3.4: Raman spectrum of a z-cut quartz substrate, measured with the ULF Raman setup.

For analysing and presenting Raman scattering data, the recorded Raman spectrum was first background corrected using a background spectrum acquired by performing the same measurement procedure but without the sample in place. The spectrum was further intensity corrected using a tungsten-filament reference lamp with a known emissivity spectrum. Finally, the fourth-power dependence of Raman scattering intensity on the frequency was corrected.[105] For reference, a Raman spectrum of the substrate, z-cut quartz, is presented in Figure 3.4

4

Impact of Hole-Transport Layer and Interface Passivation on Halide Segregation

Contents

The work presented in this chapter has been published in:

Lim, V. J. -Y., Knight, A. J., Oliver, R. D. J., Snaith, H. J., Johnston, M. B., Herz, L. M. 'Impact of Hole-Transport Layer and Interface Passivation on Halide Segregation in Mixed-Halide Perovskites'. *Advanced Functional Materials*, **2022**, 32(41), 2204825. (Ref. [106])

V. J. -Y. L. performed all the experiments and data analysis except PLQY, and wrote the manuscript. A. J. K. and L. M. H. supervised. R. D. J. O. fabricated the samples and measured PLQY. All authors discussed the results and reviewed the manuscript.

4.1 Introduction

While halide segregation has clear impact on MHP tandem device development, most investigations to date have investigated the phenomenon through relatively straightforward observation of the evolution of photoluminescence spectra of standalone MHP films under illumination.[15,16] However, this approach ignores the influence of charge-transport layers (CTLs) interfacing MHP layers, which are fundamental to the architecture of real-world MHP photovoltaic devices.[107,108] Knowledge of how charge-transport layers affect halide segregation is particularly crucial because it is well known that MHP/CTL interfaces exhibit high trap densities,[109–111] and also that electronic trap states can be important instigators of halide segregation.[15,52,63,65,69] It is noted that while there are previous studies of halide segregation in device stacks,[50,54,112] only a few studies have methodologically investigated the impact of charge-transport layers on halide segregation,[64,75] and an understanding of how trap states affect such segregation is still lacking. In particular, it has been proposed that only a subset of electronic traps appear to be associated with halide segregation,[52,74] therefore a distinction is beneficial between the impact of traps present in the MHP bulk and those introduced at the MHP/CTL interface. In addition, the prominent use of photoluminescence techniques to reflect the extent to which halide segregation has occurred has been shown to be misleading at times,[57] because the spectra collected not only represent the fraction of the material present in the phase-segregated state, but also the extent to which charge carriers diffuse to iodide-enriched, low-energy domains. In the presence of a CTL competing with iodide-rich domains for charge-carrier collection, any changes in PL spectra over time may therefore be potentially unable to capture accurately the true extent to which halide segregation has occurred.

In this study, I have investigated the effects of a hole-transport layer (HTL) and trap passivation on halide segregation in the lead mixed-halide perovskite $FA_{0.83}Cs_{0.17}Pb(Br_{0.4}$

$I_{0.6})_3$ whose bandgap of 1.79 eV is optimised for use in all-perovskite tandem photovoltaic devices.[113] Compared to the mixed wide-bandgap phase, the iodide-rich regions formed during halide segregation are known to have a higher valence band edge but relatively unchanged conduction band edge.[48,49] I thus expect halide segregation to affect charge-carrier dynamics mostly in the presence of a HTL, and therefore focus on such effects here. Through a combined approach of in-situ, simultaneous X-ray diffraction (XRD) and photoluminescence (PL) spectroscopy, I am able to disentangle the structural effects of halide segregation from its impact on optoelectronic properties, showing that in the presence of hole-transport layers, an assessment of halide segregation from photoluminescence measurements alone can be highly misleading. My analysis reveals that the presence of a typical poly(triaryl amine) (PTAA) hole-transport layer surprisingly lowers the extent to which halide segregation occurs. This effect primarily results from the removal of holes from the bulk of the MHP, as a result of them being trapped at the MHP/PTAA interface and holes drifting into the PTAA. I show that the highly abundant interfacial trap states at the MHP/PTAA interface do not drive halide segregation, and are efficiently passivated by a piperidinium salt. Interestingly, the removal of trap states at the MHP/PTAA interface leads to more halide segregation being observed, as determined from XRD measurements. This is because charge carriers are no longer populating these interfacial states, and instead accumulate in bulk trap states that do drive the segregation process. These findings thus demonstrate the effect of an HTL on the halide segregation process and underline the need for passivation strategies tuned to eliminate the specific type of trap states that drive halide segregation.

4.2 Results and Discussion

$FA_{0.83}Cs_{0.17}Pb(Br_{0.4}I_{0.6})_3$ is relevant to all-perovskite and perovskite/silicon tandem cell applications as the top (wide bandgap) subcell,[12,114,115] owing to its superior stability, compared to MA-based MHPs,[21,23,116] and its ideal bandgap.[23] Samples were fabricated on z-cut quartz substrates, as detailed in Section A.1, with one set of MHP films being over-coated with a poly(triaryl amine) (PTAA) hole-transport layer,[49] and another with an inert layer of poly(methyl methacrylate) (PMMA) to act as a control system. Ambient air is known to interact with MHPs and affect their PL transients[117–119] and halide segregation dynamics,[69,120] therefore the PMMA coating was chosen to eliminate such interactions with ambient gas by providing encapsulation in the absence of electronic interactions with the MHP.[57] Each set of MHP samples were further fabricated either with or without a piperidinium ionic additive (1-butyl-1-methylpiperidinium tetrafluoroborate ($[\mathrm{BMP}]^+[\mathrm{BF_4}]^-$)) which has recently been reported to effectively passivate traps occurring near the boundary between the perovskite photoactive layer and the hole-transport layer.[121,122] It has been proposed that this piperidinium ionic additive reduces the density of iodine Frenkel defects by adsorbing to them at the surface.[121] The addition of the piperidinium salt to the MHP layer enabled us to investigate halide segregation in real-world conditions, for which effective passivation strategies are likely to have been deployed. Moreover, the piperidinium additive enabled us to distinguish the electronic effects of adding a PTAA layer from those arising solely from the introduction of interfacial trap states at the MHP/PTAA boundary. Absorption spectra measured for these four thin-film combinations (either with PTAA or PMMA coating, with or without piperidinium salt), as well as two further MHP films without any coating, show that neither the coating nor the addition of piperidinium affected the absorption spectra of the $\mathrm{FA_{0.83}Cs_{0.17}Pb(Br_{0.4}I_{0.6})_3}$ perovskite in the wavelength region of interest, as presented in Figure 4.1, and this is in agreement with the observations of Oliver et al., who showed such piperidinium additive had negligible effect on the fundamental electronic structure of the MHP.[122]

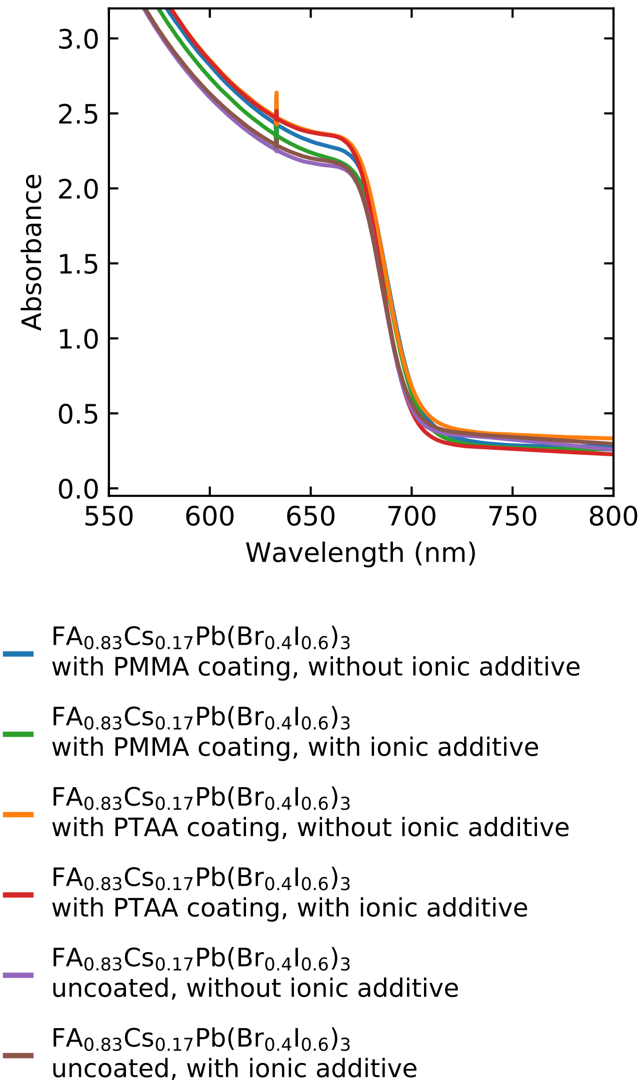

Figure 4.1: Absorbance spectra for $FA_{0.83}Cs_{0.17}Pb(Br_{0.4}I_{0.6})_3$ thin films, top-coated with PMMA or PTAA, or uncoated, and with or without piperidinium ionic additive to the MHP, measured before any halide segregation may have occurred. The peaks at 632.8 nm are from He-Ne laser used for alignment within the FTIR.

4.2.1 Effects of HTL

To explore halide segregation in $FA_{0.83}Cs_{0.17}Pb(Br_{0.4}I_{0.6})_3$ in the presence of a HTL, I employed an in-situ, concurrent XRD and PL measurement approach described previously elsewhere[57] and in Section 3.3.1. XRD and PL have commonly been used as two separate techniques to characterize the extent to which halide segregation has occurred in a mixed-halide MHP.[16,50,51,63,123,124] However, their in-situ combination presents distinct

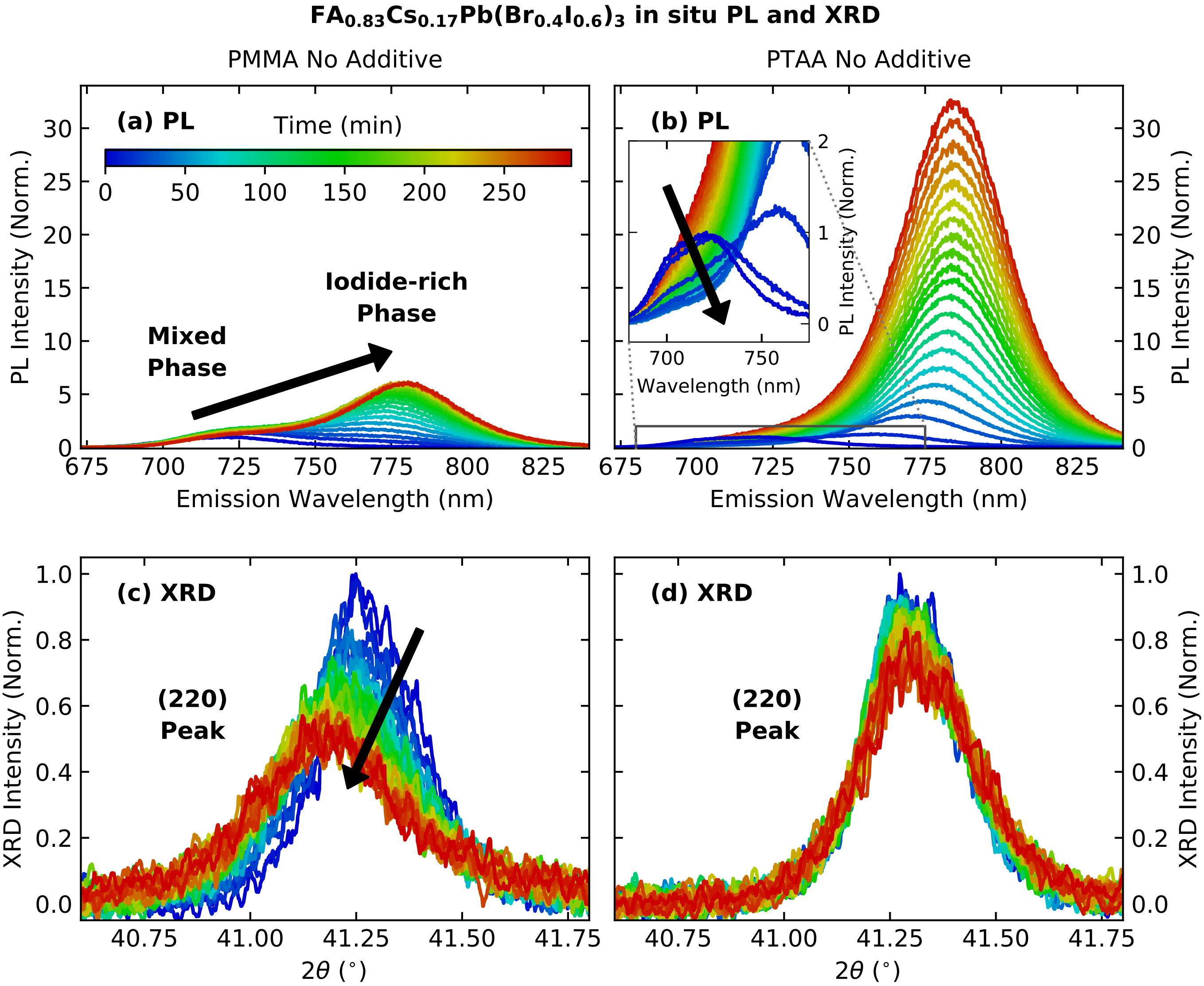

Figure 4.2: In situ, simultaneously recorded PL spectra and XRD patterns, recorded in ambient air for $FA_{0.83}Cs_{0.17}Pb(Br_{0.4}I_{0.6})_3$ thin films coated with either PMMA or PTAA under 470 nm continuous wave (CW) illumination with 190 mW cm^{-2} intensity for $\approx$ 5 hours. (a) PL spectra, normalized to the maximum value of the spectrum at time = 0, for an $FA_{0.83}Cs_{0.17}Pb(Br_{0.4}I_{0.6})_3$ thin film coated with PMMA. (b) PL spectra, normalized to the spectrum at time = 0, for an $FA_{0.83}Cs_{0.17}Pb(Br_{0.4}I_{0.6})_3$ thin film coated with PTAA. (inset) An enlarged view of the PL spectra with finer time steps between consecutive spectra, with those for earliest illumination times shown in blue. (c) Evolution of the (220) X-ray diffraction peak of an $FA_{0.83}Cs_{0.17}Pb(Br_{0.4}I_{0.6})_3$ thin film coated with PMMA, recorded in situ and simultaneously with PL measurements shown in (a). (d) Evolution of the (220) XRD peak of an $FA_{0.83}Cs_{0.17}Pb(Br_{0.4}I_{0.6})_3$ thin film coated with PTAA, recorded in situ and simultaneously with (b). Cu-K$_{\alpha 1}$ line was used as the incident radiation for (c) and (d).

advantages because the two techniques probe different aspects of the material. While XRD probes structural properties evenly across the bulk material, PL spectra reflect the optoelectronic properties of the MHP, and specifically the material regions where radiative recombination of charge carriers is prevalent. For the specific case of monitoring halide segregation, XRD will accurately reflect the extent to which the materials have structurally segregated in the bulk, while PL will in addition be highly influenced by charge-carrier funnelling into iodide-rich regions.[56] The combination of these two measurement techniques is particularly important for this study, since the presence of the PTAA layer will lead to charge extraction from the MHP by equilibrating the quasi-Fermi levels.[125] The optoelectronic and structural properties reflected in the PL and XRD may therefore be affected in different ways depending on the presence of PTAA, as well as the piperidinium additive.

I begin the analysis by contrasting halide segregation during illumination for $FA_{0.83}Cs_{0.17}Pb(Br_{0.4}I_{0.6})_3$ thin films top-coated with either a PTAA hole-extraction layer or an inert PMMA layer. It is noted that MHP thin films in absence of any coating layers were also examined (see Figure A.1), however, these exhibit qualitative behavior similar to that of the PMMA-coated MHP films. Those without any coating layers do exhibit some fluctuations in the PL spectra, which have previously been shown to be caused by interactions with ambient air.[69] This observation implies that the PMMA and PTAA top layers are sufficiently effective encapsulants to prevent such fluctuations arising from the interactions between ambient air and the MHP layer.[69] Figure 4.2 contrasts the PL spectra (top) and (220) X-ray diffraction peak (bottom) of $FA_{0.83}Cs_{0.17}Pb(Br_{0.4}I_{0.6})_3$ films without piperidinium additive, coated with either a PMMA (left) or PTTA (right) top layer, recorded concurrently in situ over ≈ 5 hours of illumination with a continuous-wave, 470 nm wavelength laser at $190\,\mathrm{mW\,cm^{-2}}$ intensity, ≈ 3.5 sun equivalent photon flux at this bandgap. The XRD peak selected for investigation was the (220) peak, comparable to earlier measurements.[57] This choice aimed to maximise the XRD signal, and a second-order peak was selected (as oppose to the first order (110) peak) to improve the angular resolution.

The first striking observation to be made from these measurements is that the introduction of a PTAA hole-extraction layer leads to significantly enhanced radiative recombination of charge carriers from iodide-rich domains formed by halide segregation in $FA_{0.83}Cs_{0.17}Pb(Br_{0.4}I_{0.6})_3$. Figures 4.2(a) and (b) display the PL spectra of PMMA- and PTAA-coated MHP, respectively, scaled by equating the peak intensity values of their respective initial spectra at the beginning of illumination (time = 0). For both cases, the initial photoluminescence spectra reflect the entropically mixed state (peak at 720 nm), but under laser illumination, a secondary PL peak at a higher wavelength (at 780 nm) grows with time. This low-energy PL peak corresponds to photoemission from iodide-rich regions with a lower bandgap, reflecting progressing halide segregation.[15,16,123] However, the two top layers clearly induce a different extent of low-energy PL enhancement: while the PTAA-coated MHP exhibits much more substantial growth in low-energy (high-wavelength) PL intensity with respect to the initial mixed-phase PL, by a factor of ≈ 32, the PMMA-coated MHP only exhibits a $\approx$ six-fold increase. Another way in which the qualitative behavior differs between the two scenarios is that the initial mixed-phase emission peak is always present to some extent for the PMMA-coated MHP (Figure 4.2(a), blue line, consistent with previous reports[57]), whereas this peak quickly disappears entirely for the PTAA-coated MHP (see inset in Figure 4.2(b)). I stress that at this point, these results solely reveal that the addition of a PTAA top layer results in substantially increased radiative charge-carrier recombination from iodide-rich domains in the phase-segregated MHP (compared to the case of adding an inert PMMA top-layer).

Such enhanced emission from phase-segregated domains in PTAA-coated $FA_{0.83}Cs_{0.17}Pb(Br_{0.4}I_{0.6})_3$ may at a cursory glance suggest that the addition of a HTL layer leads to increased phase segregation in the MHP. However, my analysis of the evolution of the MHP's XRD peak shows this conclusion to be erroneous, with the illuminated bulk MHP film actually showing a far lower extent of structural re-organisation for PTAA-coating (Figure 4.2(d)) than for PMMA-coating (Figure 4.2(c)). It is noted that XRD is a far more accurate measure of the extent to which halide segregation has occurred compared to PL measurements, owing to its sensitivity to structural changes occurring across the full material volume. Because bromide and iodide ions have different radii and bond lengths, the lattice parameters of the MHP shift with the local average composition of the halide site.[16,23,44,45,126] Rearrangement of these halide ions will therefore affect the local lattice parameter, which will alter the overall distribution of lattice parameters reflected in the XRD pattern. After halide segregation, the XRD patterns will reflect the changes in the lattice parameters from the presence of additional iodide- and bromide-enriched material, as well as remnants of the original well-mixed phase.[57] It is noted that other factors, including lattice strain, atomic form factor and crystallinity, and material degradation may also potentially affect the XRD response. However, I find, through angle-integration across the (220) XRD peak (Figure 4.3), that the XRD signal is constant with illumination time, indicating that the overall perovskite structure is maintained. In addition, full XRD patterns recorded after halide segregation (Figure 4.4) reveal an absence of chemical degradation e.g. to crystalline PbI_2, therefore halide segregation is the dominant process occurring under illumination. Knight et al. investigated degradation of related samples under similar conditions and observed negligible degradation.[57]

The evolution of the $FA_{0.83}Cs_{0.17}Pb(Br_{0.4}I_{0.6})_3$ XRD peaks, shown in Figures 4.2(c) and (d), clearly indicates that the PMMA-coated MHP exhibits significantly stronger halide segregation compared to the PTAA-coated MHP. The (220) XRD peak of the PMMA-coated MHP indicates an enhancement of diffraction amplitudes at angles below the peak of the original mixed-halide phase, caused by a growth in iodide-rich material,

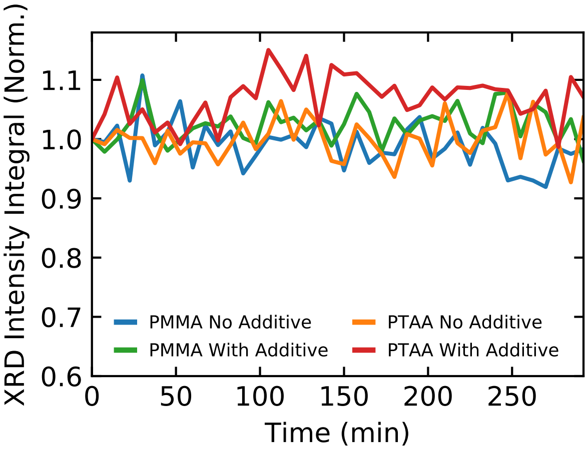

Figure 4.3: The integrals across the (220) XRD peaks for the four sample combinations under consideration, $FA_{0.83}Cs_{0.17}Pb(Br_{0.4}I_{0.6})_3$ thin films fabricated with or without piperidinium ionic additive and with either PTAA or PMMA top coating, recorded during the ≈ 5 hour illumination period, and normalized to the initial integral before the start of the illumination cycle. The integral range was between 40° and 42.5°.

and a rise in high-angle signal resulting from bromide-enriched phases, as can be more clearly seen from Figure 4.5.[57] In contrast, the XRD peak of the PTAA-coated MHP only exhibits relatively minor changes with time under illumination. Taken together, the combined PL and XRD measurements therefore demonstrate that coating the MHP with a PTAA layer results in significant suppression of bulk halide rearrangement. However, in spite of this suppression, a larger fraction of charge carriers recombines in iodide-rich domains, leading to an enhancement of low-energy PL that is far greater for PTAA coating than for the case of PMMA coating. These results therefore demonstrate that the significantly stronger enhancement of the PL from iodide-rich domains for the PTAA-coated MHP arises from the altered charge-carrier dynamics, rather than enhanced halide segregation. The combined, in-situ XRD/PL technique therefore also demonstrates that analysis of halide segregation from PL spectral evolution alone can be highly misleading, in particular in the presence of charge-extraction layers.

To understand the differences in halide segregation and PL emission between PTAA- and PMMA-coated $FA_{0.83}Cs_{0.17}Pb(Br_{0.4}I_{0.6})_3$, I consider the optoelectronic changes

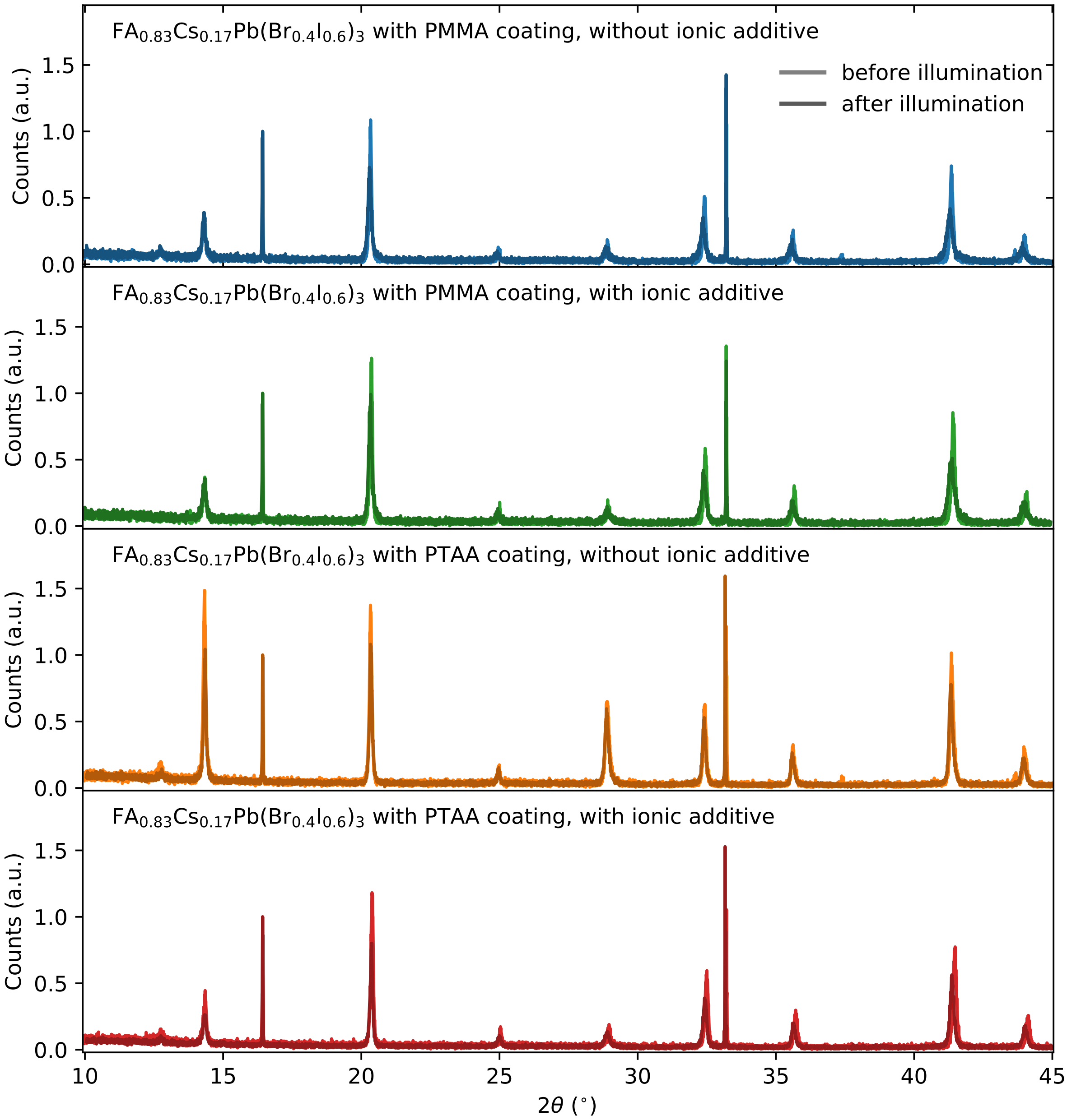

Figure 4.4: Extended wide-angle XRD patterns of the four sample combinations under consideration, $FA_{0.83}Cs_{0.17}Pb(Br_{0.4}I_{0.6})_3$ thin films fabricated with or without piperidinium ionic additive and with either PTAA or PMMA top coating, recorded before and after the ≈ 5 hour illumination period for which halide segregation was investigated.

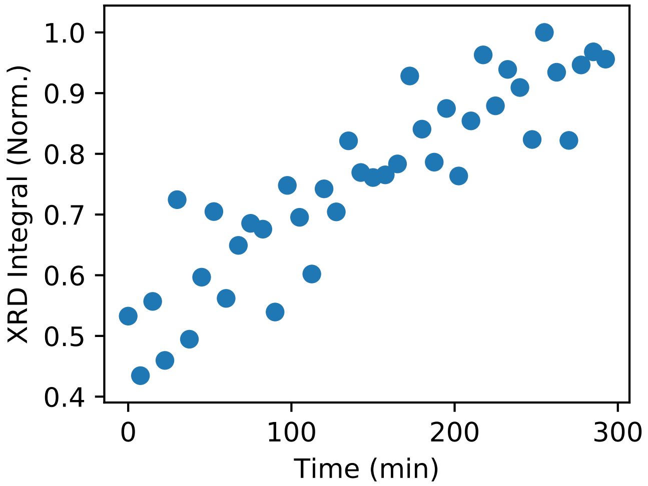

Figure 4.5: The high-angle integrals across the (220) XRD peaks between 41.5° and 42° for the $FA_{0.83}Cs_{0.17}Pb(Br_{0.4}I_{0.6})_3$ thin film fabricated without piperidinium ionic additive and with PMMA top coating, recorded during the ≈ 5 hour illumination period, and normalized to the final integral at the end of the illumination cycle.

occurring upon halide segregation at the MHP/PTAA interface. Figure 4.6 schematically depicts the simplified energy level scheme near the MHP/PTAA interface, based on literature values.[48,49,125] The valence band edge (or highest occupied molecular orbital) of PTAA is higher in energy compared to the valence band edge of $FA_{0.83}Cs_{0.17}Pb(Br_{0.4}I_{0.6})_3$, so that before halide segregation has occurred (Figure 4.6a), holes in the MHP layer diffuse towards and are captured by the PTAA layer. The energy gap between the valence bands of the mixed-phase MHP and the PTAA layer presents a significant energetic barrier towards the back-transfer of holes from PTAA back into the MHP, as desirable in a photovoltaic device. Before halide segregation commences, charge carriers are therefore likely to recombine non-radiatively, e.g. via interfacial trap states, rather than radiatively in the MHP following hole re-transfer to the MHP. The accumulation of holes within the PTAA layer is likely to influence the region in which halide segregation nucleates under prolonged illumination; hole accumulation will lead to a net positive charge within the PTAA layer, which will attract electrons in the MHP layer Coulombically towards the MHP/PTAA interface. The high charge-carrier density near the interface means

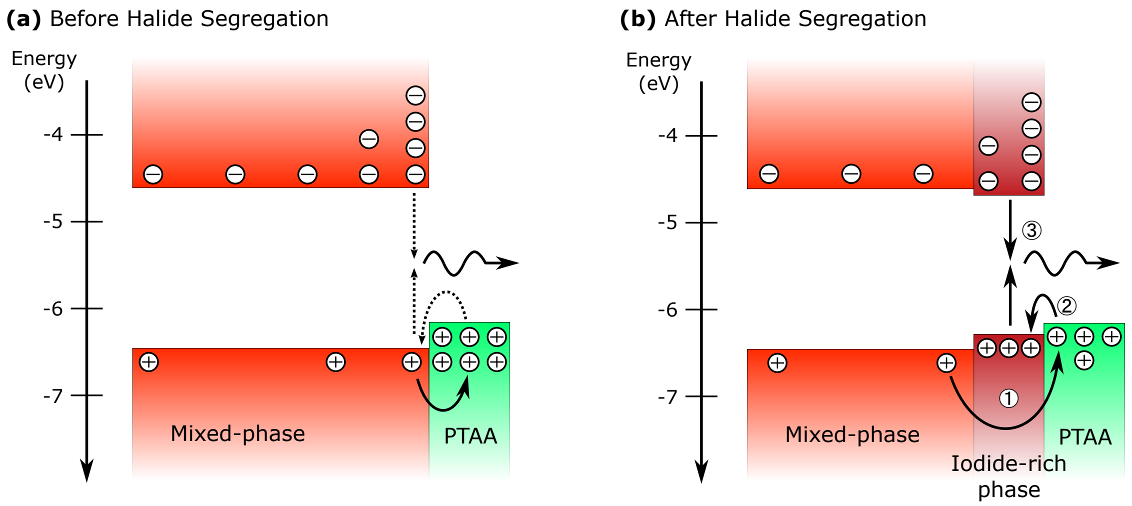

Figure 4.6: Schematic diagram illustrating the dynamics of charge carriers in a MHP/PTAA partial device before and after halide segregation. (a) Before halide segregation has occurred, photogenerated holes in the MHP diffuse into the PTAA layer, but only a small minority is able to transfer back into the MHP owing to the large energy offset at the interface. Such minority back transfer allows for relatively faint radiative recombination with electrons, yielding photoluminescence spectra representative of the mixed phase. The accumulation of holes in the PTAA layer Coulombically attracts electrons towards the MHP/PTAA interface. (b) After halide segregation has occurred, photoexcited holes diffuse into the PTAA layer (1), and a more significant proportion of these holes later back-transfer preferentially into iodide-rich regions within the MHP layer, owing to the smaller energy gap compared with the mixed phase (2). These holes subsequently recombine radiatively with electrons, yielding red-shifted photoluminescence characteristic of iodide-rich regions (3). Energy levels shown are relative to the vacuum level, and were extrapolated based on previous reports.[48,49] Bromide-rich regions formed after halide segregation are not indicated, since their wider bandgap and unfavourable energy alignment mean that charge carriers generally cannot be injected into these from mixed-phase or iodide-rich regions.

that any limited amount of halide segregation present in this configuration with PTAA will be more concentrated near the interface, rather than spread throughout the bulk. Accordingly, the charge-carrier density remaining in the bulk of the MHP layer will be relatively depleted, lowering the propensity for halide segregation to occur far from the interface. These considerations also explain my observation (from XRD) that the presence of the PTAA layer reduces halide segregation, because charge carriers driving such segregation are effectively removed from the bulk, e.g. through hole collection into PTAA or fast charge trapping at interface states.

The prevalence of halide segregation near the MHP/PTAA interface further explains the observation of enhanced photoluminescence from iodide-rich regions following illumination (Figure 4.2(b)). As schematically illustrated in Figure 4.6(b), the introduction of an iodide-rich phase near the interface alters the band alignment in this region towards more favourable back transfer of holes into the MHP, where they may recombine radiatively. The newly introduced iodide-rich regions are associated with an upshift in valence band maximum compared to that of the mixed phase,[48,127] resulting in a smaller energy difference with respect to the PTAA band edge. This altered band alignment under illumination facilitates the back-transfer of holes from PTAA to iodide-rich regions near the interface (compared to a back transfer into the original mixed-phase regions) leading to substantial radiative charge-carrier recombination from the iodide-rich MHP regions near the interface. In order to verify the better energy offset for iodide-rich regions with PTAA, PL quantum yield (PLQY) measurements were performed (by R. D. J. Oliver) for an iodide-rich MHP of the composition $FA_{0.83}Cs_{0.17}Pb(Br_{0.1}I_{0.9})_3$, which is representative of that expected for iodide-rich regions occurring in $FA_{0.83}Cs_{0.17}Pb(Br_{0.4}I_{0.6})_3$ after halide segregation from the PL emission wavelength, with and without a PTAA top-coating layer. The relative PLQY quenching observed upon the introduction of a PTAA top-coating layer was lower for the iodide-rich MHP, compared to the wide-bandgap MHP (Section A.4). Such change in PLQY for the iodide-enriched MHP as compared to the $FA_{0.83}Cs_{0.17}Pb(Br_{0.4}I_{0.6})_3$ MHP further corroborates that the PL enhancement is the direct result of improved band alignment for hole re-transfer and/or a reduction in traps upon iodide enrichment; this is in agreement with Oliver et al. who demonstrated a significant deviation between the quasi-fermi level splitting and open-circuit voltage for wide-bandgap MHP devices,[122] and Stolterfoht et al. showing a smaller such offset for a low-bandgap (iodide-rich) MHP device.[128]

The dynamic processes occurring in PTAA-coated $FA_{0.83}Cs_{0.17}Pb(Br_{0.4}I_{0.6})_3$ after halide segregation can therefore be summarized as follows. Photogenerated holes diffuse into the PTAA layer (step 1 in Figure 4.6(b)), after which holes will preferentially funnel back into the iodide-rich regions induced by halide segregation near the interface (Figure 4.6(b) step 2). It is noted that bromide-rich regions will also form to conserve overall halide content, but charge carriers cannot enter these regions from mixed-phase or iodide-rich regions as they exhibit wider bandgap and unfavourable energy alignment. These bromide-rich regions will therefore have minimal optoelectronic effects, and are neglected accordingly in Figure 4.6(b). A fraction of charge carriers recombines radiatively in these iodide-rich regions exhibiting lower bandgap (Figure 4.6(b) step 3), inducing intense red-shifted photoluminescence. These back-transfer effects also explain why no emission is observed from the original mixed-phase MHP: holes may diffuse rapidly from this phase into PTAA from which they will only transfer back effectively into iodide-rich regions.[127] In contrast, the PMMA-coated MHP still features remnant emission from the mixed phase, even after substantial halide segregation has occurred (Figure 4.2(a)), since holes neither drifted out, nor selectively reinjected into segregated phases, but rather diffuse into iodide-rich domains throughout the whole MHP layer. I therefore conclude that the significant enhancement of PL emission from iodide-rich domains in the presence of the hole-extraction layer is solely the result of charge-carrier dynamics occurring at and across the interface. The selective back-transfer of holes from PTAA to the MHP also explains the dramatic overall increase in PL intensity: concentration of charge carriers in a narrow iodide-enriched region near the interface leads to particularly rapid radiative electron-hole bimolecular recombination, resulting in higher overall photoluminescence intensity.[13,56,129]

4.2.2 Effects of Interfacial Passivation

I continue the investigation by exploring the reasons why halide segregation scarcely occurs when the MHP is top coated with PTAA. Given that halide segregation is triggered by the presence of excited charge carriers,[15,50,52] their rapid removal soon after photoexcitation could effectively limit halide segregation. The presence of a PTAA hole-transport layer may lead to holes either drifting from the MHP into the PTAA, or being trapped at defect states introduced at the interface, neither of which would occur in the presence of the inert PMMA layer. The interface between MHPs and typical charge-transport layer is known to possess an especially high density of trap states in general,[109,110,125] and this has been shown to be also true for the MHP/PTAA interface for wide-bandgap MHPs.[122] As a hydrophobic polymer, PTAA does not have any suitable bond to form with perovskites, resulting in a very poor MHP/PTAA interface.[130] It is further noted that while some types of traps have been shown to aid halide segregation, others may not, but simply act to localize charge carriers.[52] In order to understand why the addition of PTAA reduces halide segregation, it is therefore needed to distinguish the effects of hole extraction into PTAA from those of charge trapping at the MHP/PTAA interface. For this purpose, I employ a recently reported piperidinium additive that has been shown to be particularly effective in passivating trap states at MHP/CTL interfaces.[121,122]

As a first step, I ascertained the extent to which the piperidinium ionic additive reduces charge-carrier trap state densities. For this purpose, I recorded time-resolved photoluminescence transients for $FA_{0.83}Cs_{0.17}Pb(Br_{0.4}I_{0.6})_3$ thin films before halide segregation had occurred, for the four combinations of the MHP having been coated with PTAA or PMMA layers, and with and without piperidinium ionic additive having been added. As shown in Figure 4.7, the piperidinium additive increases the lifetimes of the PL transients, implying an effective reduction in trap state density. The transients also confirm the high density of trap states introduced by the MHP/PTAA interface, given that the PTAA-coated MHPs exhibit significantly shorter charge-carrier lifetimes than the those coated with inert PMMA coating, in particular in the absence of piperidinium additive (see Table 4.1 for extracted lifetimes from monoexponential fitting, whose fits

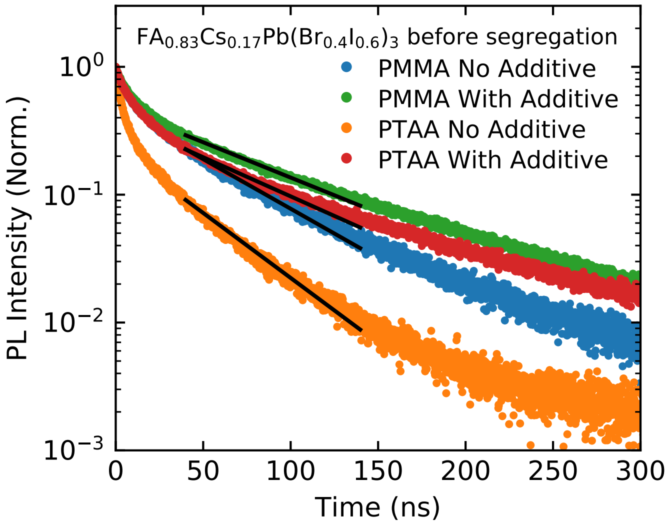

Figure 4.7: PL decay transients for $FA_{0.83}Cs_{0.17}Pb(Br_{0.4}I_{0.6})_3$ thin films coated with either PMMA or PTAA, with and without piperidinium salt having been added to the perovskite during processing. Films were excited with a pulsed laser (1 MHz repetition rate) at 470 nm with fluence of 15 nJ cm^{-2} and PL was detected at a wavelength of 700 nm corresponding to emission from the high-energy mixed phase of the perovskite, before any phase segregation had occurred under illumination. The black lines indicate monoexponential fits after an initial fast decay due to trap filling and bimolecular recombination.

are shown in Figure 4.7). Meanwhile, the long charge-carrier lifetimes for the PMMA-coated MHPs further corroborates that the boundary between inert PMMA and MHP layer is relatively benign. Trap state passivation upon the addition of piperidinium salt is evidently highly effective, with passivated films showing strikingly similar PL transients, regardless of the top-layer coating. It should also be noted that most likely, the piperidinium additive not only passivates interfacial trap states, but also bulk trap states to an extent, given the observed rise in charge-carrier lifetimes for the PMMA-coated MHPs upon the addition of piperidinium salt.

It is found that once interfacial trap states have been removed through piperidinium ionic additive, both PMMA and PTAA-coated $FA_{0.83}Cs_{0.17}Pb(Br_{0.4}I_{0.6})_3$ films undergo halide segregation to an almost identical extent. Figure 4.8(a) and (b) show that following 5 hours of illumination with 190 mW cm^{-2} intensity, the observed changes in the XRD patterns of the passivated MHP are very similar for both PMMA and PTAA coatings.

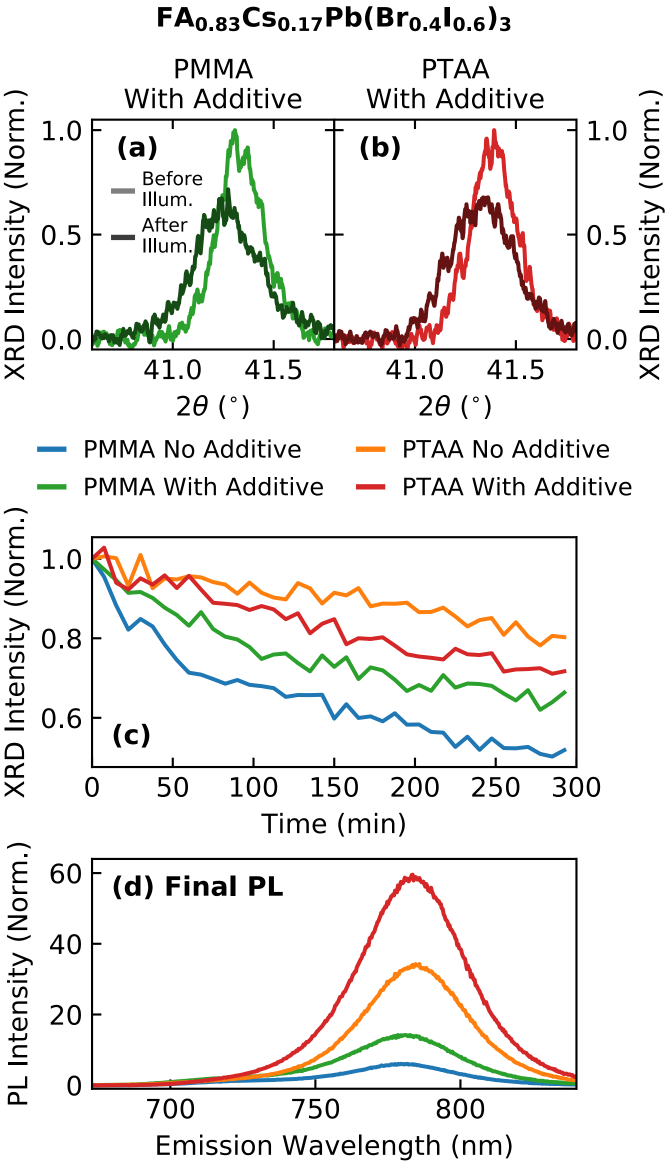

Figure 4.8: (a, b) Second-order (220) XRD peak of $FA_{0.83}Cs_{0.17}Pb(Br_{0.4}I_{0.6})_3$ films with piperidinium ionic additive, coated with either (a) PMMA or (b) PTAA, shown before and after illumination with a 470 nm laser at 190 mW cm^{-2} intensity for ≈ 5 hours. (c) Evolution of the (220) XRD peak amplitude under the same illumination conditions for $FA_{0.83}Cs_{0.17}Pb(Br_{0.4}I_{0.6})_3$ thin films with or without the addition of piperidinium salt, and with either PMMA and PTAA top coatings. (d) Final PL spectra recorded in situ at the end of the 5-hour illumination period, each normalized to the respective maximum value of the corresponding initial spectrum recorded before illumination had commenced. The raw data of the two films with piperidinium ionic additive can be found in Figure A.2.

Sample	Charge-carrier lifetime (ns)
MHP without piperidinium additive, PMMA-coated	122
MHP with piperidinium additive, PMMA-coated	157
MHP without piperidinium additive, PTAA-coated	85
MHP with piperidinium additive, PTAA-coated	142

Table 4.1: Extracted charge-carrier lifetimes of the four samples under consideration, $FA_{0.83}Cs_{0.17}Pb(Br_{0.4}I_{0.6})_3$ thin MHP films with or without piperidinium additive, coated with either PMMA or PTAA, extracted from fits assuming monomolecular recombination.

Therefore, the suppression of halide segregation in PTAA-coated, unpassivated MHPs is simply caused by the unintentional introduction of a large density of interfacial traps, rather than hole collection into PTAA. As discussed in more detail in Section A.3, the minor changes occurring in the XRD pattern under illumination for the unpassivated, PTAA-coated MHP film are also qualitatively different from those occurring in the rest of the MHPs (the XRD peak angle does not change with illumination time) which is attributed to halide segregation occurring predominantly at the MHP/PTAA interface. Thus for PTAA top coating, the extent of halide segregation is almost fully governed by the density of trap states at the MHP/PTAA interface.

It is noted that for PMMA coating, which does not introduce significant interfacial trap states, the introduction of the piperidinium salt to the MHP has a very different effect. Figure 4.8(c) exhibits the XRD amplitude evolution during illumination for the four combinations of MHP films with either PMMA or PTAA coating, with or without piperidinium additive. It is found that the rate of halide segregation in MHPs with the two different coatings are affected in opposite ways by piperidinium addition: while it accelerates halide segregation for the PTAA-coated MHPs, it slows down segregation for the PMMA-coated MHPs. I propose that such differences in the effect of the piperidinium additive on halide segregation stem from the different types of trap states present at the interface and in the bulk MHP. As discussed in more detail below, some trap states induce halide segregation, while others do not. The MHP/PTAA interface clearly presents a large number of trap states, but my results suggest that these do not drive halide segregation throughout significant volume of the MHP. Therefore, the presence of such interfacial trap states simply causes charge carriers to be trapped near the interface, as a result of which these carriers are unable to diffuse through the MHP bulk where they would otherwise have encountered traps that drive halide segregation. Rapid trapping of these charge carriers at the MHP/PTAA interface therefore suppresses halide segregation. For the case of PMMA-coated MHP films, traps exist mostly in the bulk volume of the MHP and appear to be capable of driving halide segregation. The addition of piperidinium salt then passivates these bulk trap states to an extent, slowing down halide segregation, consistent with previous reports on the effects of trap passivation on halide segregation.[15,63–66] In contrast, piperidinium passivation for the PTAA-coated film removes trap states at the interface, allowing bulk trap states to be populated and accelerating halide segregation. Thus, the overall extent of halide segregation is governed by a complex interplay of competition for charge carriers between interfacial traps that do not induce halide segregation and bulk traps that are effective drivers of halide segregation. As a result, for PTAA-coated MHP, piperidinium mostly passivates interfacial trap states, accelerating halide segregation, while for PMMA-coated MHPs piperidinium additive passivates bulk traps, impeding halide segregation. It is noted that such trap passivation effects are clearly evident through an increase of the PL intensity upon the addition of piperidinium salt for both PMMA and PTAA-coated MHPs, shown in Figure 4.8(d), and the increase in the charge carrier lifetimes discussed earlier (Figure 4.7).

It is noted that my conclusions are consistent with previous reports stipulating that only specific types of trap states are responsible for inducing halide segregation, while others are not.[52,74] Such differences may, for example, be caused by local electric fields generated by captured charge carriers in trap states driving halide segregation.[52,64,65,67–69] In this case, only initially charge-neutral defects might be responsible for halide segregation, as these will generate local charges once traps are filled. In addition, halide chemistry and oxidation has been postulated to be central to the halide segregation process.[74] Overall, it is therefore evident that the nature of trap states is as central to their propensity to drive halide segregation as their density.

With regards to the specific effect of the piperidinium additive that was employed as a passivation agent here, it is noted that Lin et al. demonstrated that it improved device stability by inhibition of lead oxidation, and proposed this was ultimately caused by either a reduction of iodide vacancy-interstitial pair Frenkel defects, or by reducing their diffusivity.[121] This is in line with previous reports showing the abundance and stability of halide defects in MHPs.[131–136] I therefore propose that the MHP/PTAA interface possesses a high density of charged halide interstitials and vacancies, the latter of which is filled with electrons upon steady-state photoexcitation, owing to the high density of electrons in the MHP layer at the interface (Figure 4.6(b)). Such halide vacancies, which also act as electronic trap states, then become neutrally charged and therefore cannot promote or participate in halide migration. The interface then effectively becomes a halide-excess environment given the abundance of halide interstitials, in which halide segregation is impeded, as observed before,[15,63,66,137–139] because the lack of available halide vacancies lowers the halide ion mobility. Upon the addition of the piperidinium salt, these halide defects become efficiently passivated. It is noted that while there are numerous reports demonstrating halide defects promoting halide segregation,[137,139–141] my results are not contradicting these, but rather proposing that the electronic nature of halide defect trap states do not contribute to halide segregation, because of their neutral charge upon charge-carrier capture. In order for halide segregation to occur, the trap states that create an electric field are required, as well as halide defects to provide low-energy halide ion migration pathways.

I would like to comment that an enhancement of PL upon the addition of any generic HTL is expected for different MHP compositions, since the mechanism of such enhancement relies on the favourable energy alignment between iodide-rich regions and HTL. However, I expect different HTL and passivation agents will affect the halide segregation behavior differently, depending on the fundamental nature of the trap states present at the MHP/HTL interface. Given the device-relevant FACs MHPs also exhibit a range of trap densities and difference in overall stability against halide segregation across the bromide-iodide ratio, I expect some variations as halide content is changed.[24] The stability of a mixed-halide perovskite in the presence of an HTM against halide segregation therefore depends critically on the nature of the trap states present in the bulk and at the interfaces, and the chemical and physical mechanisms of passivation techniques deployed.

4.3 Conclusion

In conclusion, I have investigated the effects of hole-transport layers and trap passivation agents on halide segregation in a lead mixed-halide perovskite with bandgap optimized for use in tandem in all-perovskite photovoltaic devices ($FA_{0.83}Cs_{0.17}Pb(Br_{0.4}I_{0.6})_3$). While observation of changes in PL spectra under illumination is most commonly used to assess the extent to which halide segregation occurs, I find here that such assessment can be highly misleading, in particular in the presence of hole-transport layers. I show that the combined approach – concurrently assessing the structural changes associated with halide segregation through XRD, and the optoelectronic changes with PL spectroscopy – is able to provide an accurate understanding of these processes. The presence of a hole-transport layer such as PTAA slows down halide segregation, compared to the case of inert PMMA (or absent) coating. This effect primarily results from the removal of charge carriers from the bulk of the perovskite by their capture into interfacial trap states at the MHP/PTAA boundary. However, despite the observed reduction in halide segregation for the PTAA-coated MHP, more photoluminescence is emitted from iodide-rich domains in the presence of PTAA, which I attribute to preferential back-transfer of holes from PTAA to iodide-rich regions formed in close proximity to the interface. I further demonstrate that electronic traps generated near the interface between PTAA and the MHP, although present in high density, are ineffective drivers of halide segregation, while those that are prominent in the bulk are responsible for most of the halide segregation observed. Removal of such trap states at the MHP/PTAA interface with a piperidinium additive thus interestingly leads to more halide segregation occurring because, instead of channelling into interfacial states, charge carriers now accumulate in bulk trap states which are highly effective drivers of the segregation process. Overall, my work shows that interfacial trap states prominent at the MHP/PTAA interface do not contribute significantly to halide segregation throughout the bulk MHP and are efficiently passivated by a piperidinium salt. However, the presence of a PTAA layer leads to hole back-transfer from PTAA into iodide-enriched regions near the interface that exhibit reduced interfacial energy offsets, adversely affecting photovoltaic performance. Such re-transferred holes may in turn exacerbate radiative recombination losses in the MHP beyond the detailed balance limit, by generating locally strongly enhanced electron and hole densities. Careful passivation of trap states at the interface between MHP and charge-extraction layers therefore remains imperative for achieving high efficiencies in wide-bandgap photovoltaics devices.

5

Air-Degradation Mechanisms in Mixed Lead-Tin Halide Perovskites

Contents

The work presented in this chapter has been published in:

Lim, V. J.-Y., Ulatowski, A. M., Kamaraki, C., Klug, M. T., Miranda Perez, L., Johnston, M. B., Herz, L. M. 'Air-Degradation Mechanisms in Mixed Lead-Tin Halide Perovskites for Solar Cells'. *Advanced Energy Materials*, **2023**, 13(33), 2200847. (Ref. [99])

V. J.-Y. L. performed all the experiments and data analysis, and wrote the manuscript. A. M. U. and L. M. H. supervised. C. K. fabricated the samples. All authors discussed the results and reviewed the manuscript.

5.1 Introduction

Despite their importance to the development of all-perovskite tandem cells, mixed lead-tin halide perovskites still suffer from instabilities when exposed to oxygen and moisture even under encapsulation,[142] which deteriorate their optoelectronic properties and hinder their commercialization.[41,142–144] However, a comprehensive evaluation of the degradation pathways in lead-tin halide perovskites is still part of ongoing research. The degradation mechanisms of tin-only halide perovskites have been previously investigated,[31,41,145–148] providing potential insight into the degradation pathways of their mixed lead-tin counterparts. Tin-only MHPs suffer from severe oxygen and moisture stability issues, which derive from the formation of tin vacancies and iodide interstitials.[30,149] The presence of these point defects induces the oxidation of Sn^{2+} to Sn^{4+}[150,151] and introduces unintentional p-type doping, leading to the presence of a large density of background holes.[32] Such oxidation of the metal in the perovskite structure is intensified by the relatively small standard reduction potential of Sn^{4+}/Sn^{2+} when compared to Pb^{4+}/Pb^{2+} (+0.15 and +1.67 V, respectively).[149,152] SnF_2 additive has been commonly and successfully used to suppress tin vacancy formation in tin-only perovskites by creating a tin-rich environment during the fabrication process.[31–34] There have been suggestions that mixed lead-tin MHPs may undergo similar degradation pathways, involving tin vacancy formation and oxidation. An increase in lead content is expected to result in a gradual transition toward the defect chemistry present in lead-only perovskite, which is mostly free of trap states located deeply in the bandgap.[30] However, full knowledge of the defect chemistry in mixed lead-tin MHPs is still lacking, with a particular need to contrast the degradation mechanisms of tin-only with those of mixed tin-lead iodide perovskites.

In this study, I have unraveled the differences in the degradation pathways of tin-only and mixed lead-tin MHPs under ambient air. I examined spin-coated $FA_{0.75}Cs_{0.25}Pb_{0.5}Sn_{0.5}I_3$

(mixed lead-tin) and $FA_{0.75}Cs_{0.25}SnI_3$ (tin-only) thin perovskite films (fabrication details provided in Section B.1) which have direct relevance to all-perovskite tandem and lead-free single-junction photovoltaics devices, respectively. Both of these compositions were fabricated with the addition of 10 mol SnF_2, which has been a frequently adopted additive in previous studies reporting high-performing photovoltaic devices.[153–156] I investigated the optoelectronic properties of the perovskites in ambient air utilizing a combination of non-contact transient THz photoconductivity measurements and visible absorption spectroscopy, and their structural and vibrational properties employing X-ray diffraction (XRD) as well as infrared and THz transmission spectroscopy. It was found that degradation in tin-only $FA_{0.75}Cs_{0.25}SnI_3$ can be explained almost exclusively by tin-vacancy formation and self-doping effects. However, I demonstrate that for intermediate mixed lead-tin MHPs this is not the prevalent degradation pathway. I instead propose that degradation of lead-tin iodide perovskites in ambient air involves the formation of deep trap states, which do not contribute to the significant doping of the MHP. The findings thus highlight that stability improvements for mixed lead-tin perovskites likely require different defect passivation methods to those already developed for their tin-only counterparts.

5.2 Results and Discussion

I commence the study by investigating the effect of ambient air exposure on the optoelectronic properties of $FA_{0.75}Cs_{0.25}Pb_xSn_{1-x}I_3$ thin films, contrasting the mixed lead-tin material $FA_{0.75}Cs_{0.25}Pb_{0.5}Sn_{0.5}I_3$ with its tin-only $FA_{0.75}Cs_{0.25}SnI_3$ equivalent (full fabrication protocols are provided in Section B.1). Assessing such changes in the optoelectronic quality of the materials under air degradation is critical for photovoltaic applications which rely on photo-generated charge carriers being able to travel across the full thickness of the active layer to the respective transport layers and electrodes for the efficient generation of electrical power. High charge-carrier diffusion lengths are essential to this process and depend on high electronic mobilities and low charge-carrier recombination rates.[157] Therefore, to assess the effect of oxygen and moisture exposure on the optoelectronic properties of the materials, I measured the changes occurring in their photoinduced conductivity dynamics during exposure to ambient air of 45 ± 10% humidity over hundreds of minutes. I employed optical-pump terahertz-probe (OPTP) spectroscopic technique,[100] for which the films are excited with an ultrafast pump laser pulse, and their time-dependent photo-induced conductivity is measured by THz probe-pulse transmission, as detailed in Section 3.4.2.

5.2.1 OPTP Measurements

Figure 5.1(a) shows examples of photoconductivity decay transients measured for a $FA_{0.75}Cs_{0.25}SnI_3$ thin film at different air-exposure times (full data sets for both $FA_{0.75}Cs_{0.25}$ SnI_3 and $FA_{0.75}Cs_{0.25}Pb_{0.5}Sn_{0.5}I_3$ are provided in Section 3.4.2. With increasing air exposure, the photoconductivity amplitude following initial photoexcitation declines. This trend can be understood given that the conductivity σ of the material depends on the charge-carrier pair density n and the electron-hole sum mobility μ according to $\sigma = en\mu$, where e is the elementary charge. The mobility of the charge carriers can therefore be extracted from the THz transmission immediately after photoexcitation (time = 0) before any charge-carrier recombination events may have occurred (full description of data analysis provided in Section 3.4.2). The subsequent decay of the photoconductivity over time after excitation is associated with the decline of charge-carrier population $n(t)$, therefore providing insight into the charge-carrier recombination dynamics. It is found that the photoconductivity transients can be well described by a monoexponential decay function, $n(t) = n_0\exp(k_1 t)$, with fits displayed as solid lines on top of measured data shown in hollow hoops. The majority of charge carriers thus recombine through monomolecular channels, which could arise, e.g., from trap-mediated recombination or electron recombination with a significantly larger density of background holes, both of which depend on the dynamics of only one charge-carrier species.[33] From these monoexponential fits (full data set and fits shown in Figure 5.2 and 5.3) I extracted values for the decay rate k_1 (shown in Figure 5.1(b)) and electron-hole sum mobility μ (Figure 5.1(c)) for both $FA_{0.75}Cs_{0.25}SnI_3$ and $FA_{0.75}Cs_{0.25}Pb_{0.5}Sn_{0.5}I_3$ thin films and plotted them against degradation time in air. These data reveal a clear rise in recombination rates and a decrease in charge-carrier mobility for both materials with air exposure. As shown in Figure 5.4, the combined effect has disastrous consequences for the charge-carrier diffusion length L_D in the two materials: for $FA_{0.75}Cs_{0.25}SnI_3$, air exposure over 5 h leads to a three-fold decline of L_D from 270 to 80 nm while for $FA_{0.75}Cs_{0.25}Pb_{0.5}Sn_{0.5}I_3$, L_D falls from initially 910 to 220 nm.

Surprisingly, Figure 5.1(b) reveals that the relative increase in the recombination rate with extended air exposure is far smaller for $FA_{0.75}Cs_{0.25}SnI_3$ than for its lead-tin equivalent, even though the initial rate for the pristine thin film is significantly higher. This observation indicates[33] that as-fabricated $FA_{0.75}Cs_{0.25}SnI_3$ is more prone to defect formation even in the absence of sizable exposure to oxygen or moisture. This difference arises from marked changes in the defect chemistry along the lead-tin solid solution line, as predicted previously from theoretical calculations,[30] which will be discussed in more detail later below. Conversely, the low initial value of the decay rate k_1 for $FA_{0.75}Cs_{0.25}Pb_{0.5}Sn_{0.5}I_3$ suggests inherently better resistance during fabrication to the type of defects accelerating monomolecular recombination, however, the significant increase in the recombination rate after air exposure highlights the clear need for highly air-impermeable encapsulation of PV devices employing these absorbers.

Interestingly, Figure 5.1(c) shows that the air-induced acceleration of defect-related charge-carrier recombination affects the charge-carrier mobilities of $FA_{0.75}Cs_{0.25}SnI_3$ and

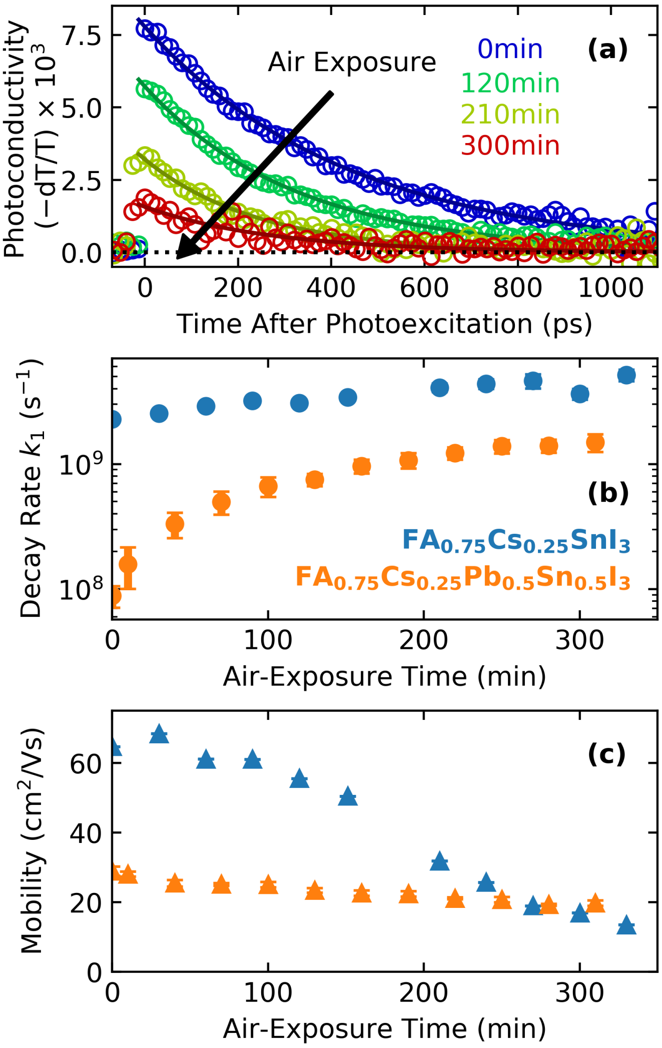

Figure 5.1: a) Photoconductivity decay transients obtained from optical-pump THz-probe photoconductivity measurements performed on $FA_{0.75}Cs_{0.25}SnI_3$ with 400 nm photoexcitation and fluence of 3.6 µJ cm^{-2} at discrete air-exposure (degradation) times in ambient air (full data set shown in Figure 5.2) and 5.3. b) Monomolecular charge-carrier recombination rates (k_1, shown in solid circles) and c) charge-carrier mobilities (solid triangles) of $FA_{0.75}Cs_{0.25}SnI_3$ (blue) and $FA_{0.75}Cs_{0.25}Pb_{0.5}Sn_{0.5}I_3$ (orange) thin films were extracted from THz photoconductivity measurements shown in (a) and Figure 5.2 and 5.3.

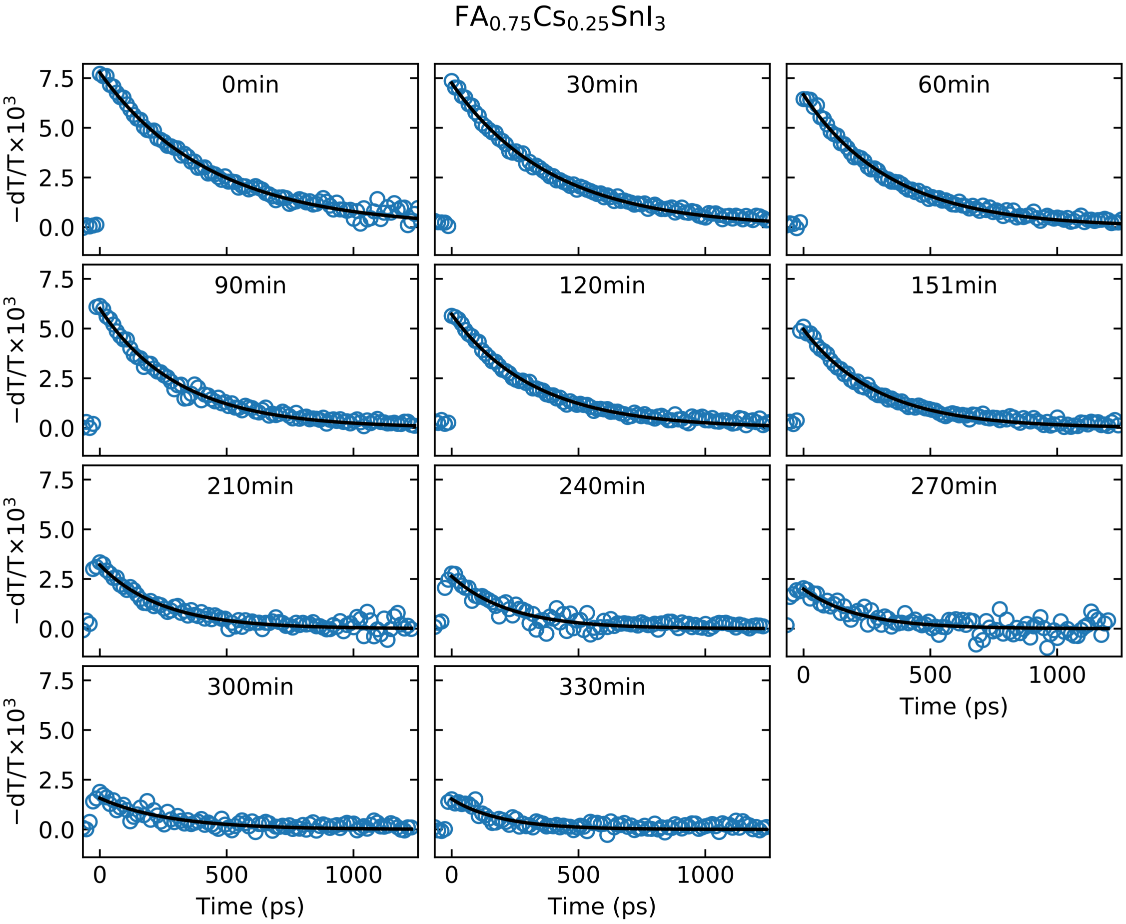

Figure 5.2: Photoconductivity decay transients of a $FA_{0.75}Cs_{0.25}SnI_3$ thin film at different degradation times with monoexponential fits (black solid lines) shown on top of the data (empty hoops). The samples were excited with a 400 nm wavelength laser pulse with fluence of 3.6 µJ cm^{-1}

$FA_{0.75}Cs_{0.25}Pb_{0.5}Sn_{0.5}I_3$ to different extents. In general, defect formation is expected to be accompanied by a decrease in charge-carrier mobility because of the introduction of scattering centers. However, while $FA_{0.75}Cs_{0.25}Pb_{0.5}Sn_{0.5}I_3$ exhibits the strongest increase in recombination rate (Figure 5.1(b)), its decline of mobilities (Figure 5.1(c)) with air exposure is much more gradual than that observed for $FA_{0.75}Cs_{0.25}SnI_3$. The tin-only $FA_{0.75}Cs_{0.25}SnI_3$ initially exhibits higher mobility prior to air exposure, which intrinsically results from fundamentally lower effective masses of charge carriers, and higher energies of the optical phonon mode in tin halide perovskites compared to lead-halide perovskites.[33,158] However, the charge-carrier mobility for $FA_{0.75}Cs_{0.25}SnI_3$ decreases

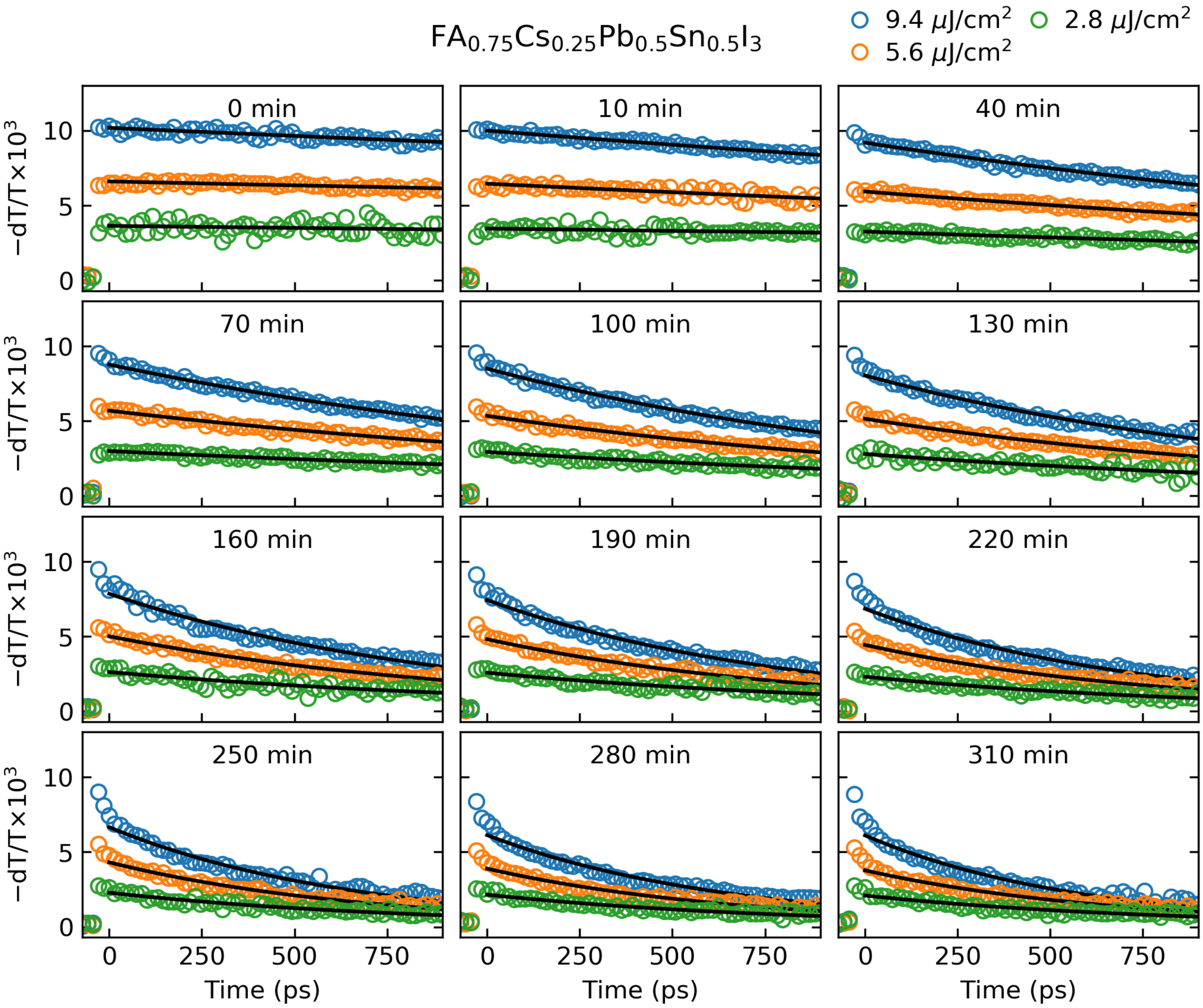

Figure 5.3: Photoconductivity decay transients of a $FA_{0.75}Cs_{0.25}Pb_{0.5}Sn_{0.5}I_3$ thin film measured for different fluences of the photoexcitation beam of 400 nm wavelength, as indicated in the legend. Transients are shown at different air exposure times indicated by the captions of sub-figures, with monoexponential fits in solid black line shown on top of the data (empty hoops).

drastically to only $\approx 20\,\%$ of its initial value over the first ≈ 300 min of air exposure, while for $FA_{0.75}Cs_{0.25}Pb_{0.5}Sn_{0.5}I_3$, this decline is much less severe, to $\approx 80\,\%$ its initial value after the same degradation time. This finding suggests that although both materials experience significant defect formation during air-induced degradation, the types of defects forming in tin-only MHPs are more detrimental to the charge-carrier mobility than those formed in mixed Pb-Sn perovskites.

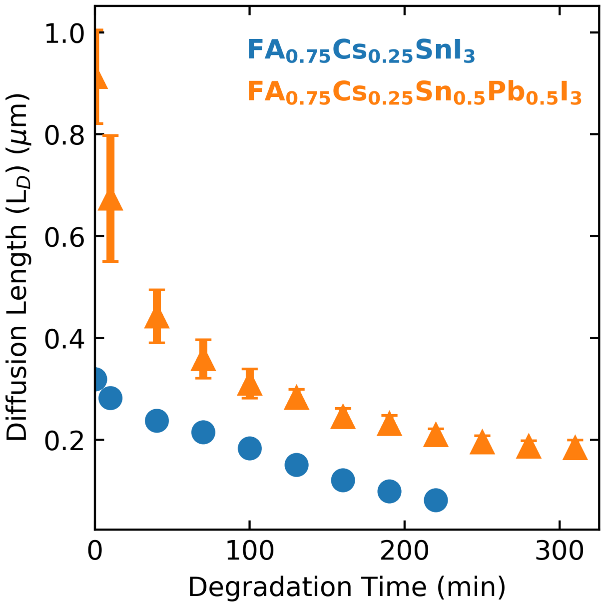

Figure 5.4: Charge-carrier diffusion lengths at different ambient air exposure times, derived from OPTP measurements of charge-carrier mobilities and recombination rates for thin films of tin-only $FA_{0.75}Cs_{0.25}SnI_3$ and mixed lead-tin $FA_{0.75}Cs_{0.25}Pb_{0.5}Sn_{0.5}I_3$ perovskites.

These observations provide clues to the differences in the defect chemistry of tin-rich and intermediate lead-tin halide perovskites. Tin-rich perovskites are prone to tin vacancy formation, which may be accompanied by tin oxidation and iodine interstitial formation.[30] Tin vacancies are known to cause background p-doping of the MHP material by introducing defect states within the valence band that capture electrons and therefore effectively release free holes into the semiconductor.[30] Such p-doping deteriorates optoelectronic properties of the material by increasing the charge-carrier recombination rates through the introduction of additional recombination pathways, for example through radiative recombination of photogenerated electrons with background holes that are present in high density.[80] Concurrently, such effects will reduce charge-carrier mobility because tin vacancies will be negatively charged following free hole release, making them particularly effective scattering centers to mobile charge carriers.[33,34] In addition, charge-carrier scattering with rates in the femtosecond regime[34] may reduce their mobilities in the presence of substantial hole densities resulting from such self-doping. In contrast, intermediate lead-tin iodide perovskites appear to exhibit a different type of degradation pathway for which the defects formed do not possess significant scattering cross-section, as evidenced by relatively unchanged charge-carrier mobility over the measurement time window accompanying the sharp increase in recombination rates. The significant increase in photoconductivity decay rate k_1 for $FA_{0.75}Cs_{0.25}Pb_{0.5}Sn_{0.5}I_3$ under air exposure is therefore most likely associated with the formation of defects that are charge-neutral, which would result in lower scattering cross-section and would not lead to electrical doping.

5.2.2 Absorption Spectra and Elliott Theory

To explore such differences in air-degradation mechanisms of $FA_{0.75}Cs_{0.25}SnI_3$ and $FA_{0.75}Cs_{0.25}Pb_{0.5}Sn_{0.5}I_3$ films further, I assessed the effect of air-exposure on their electronic structure. The absorption spectrum of a thin film provides an insight into the electronic structure of the material, enabling evaluation of the bandgap and exciton binding energies. In general, the absorption spectrum of a semiconductor displays a continuum band-to-band absorption above its bandgap energy E_g, which is enhanced by electron-hole Coulomb interactions, and a resonant absorption peak below E_g, owing to the formation of a bound electron-hole excitonic state. Changes to the bandgap of material would then lead to a shift of the whole spectrum in energy, whereas changes to the strength of exciton binding energies E_b would mostly moderate the absorption onset at low energies. Figure 5.5(a) and (c) show changes in the absorption spectrum over $\approx 15\,\mathrm{h}$ of air exposure for $FA_{0.75}Cs_{0.25}SnI_3$ and $FA_{0.75}Cs_{0.25}Pb_{0.5}Sn_{0.5}I_3$ films, respectively. The significant change observed for the low-energy part of the absorption spectrum of tin-only $FA_{0.75}Cs_{0.25}SnI_3$ could in principle be caused by either the Burstein-Moss effect or a decrease in the exciton binding energy. Burstein-Moss effects[33,159,160] are prominent in tin-rich perovskites[33,34,161] owing to the presence of high hole densities resulting from tin vacancies and the resulting unintentional doping, which lowers the Fermi level and partially depletes the valence band of electrons. As a result, light absorption is only possible from states deeper into the valence band, blue-shifting the absorption edge of the material without significantly affecting the continuum absorption at higher energies.[33,159,160] In addition, such an increase in the background hole density may also affect the exciton binding energy through enhanced electronic screening of the Coulomb attraction that binds excitons.[32,162] To unravel these effects, I performed fits according to Elliott theory[92] which describes the absorption of a semiconductor in the presence of Coulomb interactions (as detailed in Section 3.1.1, and the fits shown in Figure 5.6), with the resulting values for the bandgap E_g and exciton binding energy E_b displayed as a function of air-exposure time in Figure 5.5(b) and (d) for $\mathrm{FA_{0.75}Cs_{0.25}SnI_3}$ and $\mathrm{FA_{0.75}Cs_{0.25}Pb_{0.5}Sn_{0.5}I_3}$, respectively. The absorbance spectra in the pristine state was first fitted by the Elliot formula given in Section 3.1.1, varying all the parameters to achieve the best fit (using the Nelder-Mead method). Subsequently, most of the fitting parameters were fixed, and only the bandgap E_g and the exciton binding energy E_b were allowed to be varied as free parameters to optimize the fitting function for different exposure times.

My analysis demonstrates that for $\mathrm{FA_{0.75}Cs_{0.25}SnI_3}$, both Burstein-Moss effect and exciton screening gain significant prominence as the tin-only material is exposed to air, as revealed by an increase in the effective bandgap and a decrease of the binding energy. As explained above, these observations are consistent with a significant amount of electronic doping being introduced into the material during the degradation process, most likely arising from the tin-vacancy formation. For the mixed lead-tin $\mathrm{FA_{0.75}Cs_{0.25}Pb_{0.5}Sn_{0.5}I_3}$ perovskite, on the other hand, the evolution of the absorption spectrum and the corresponding Elliott fitting (Figure 5.5(c,d)) imply only very minor changes in the effective bandgap and exciton binding energies, even over long ($\approx 15\,\mathrm{h}$) air-exposure times. Thus, it is concluded that, in contrast to tin-only $\mathrm{FA_{0.75}Cs_{0.25}SnI_3}$, the defects in

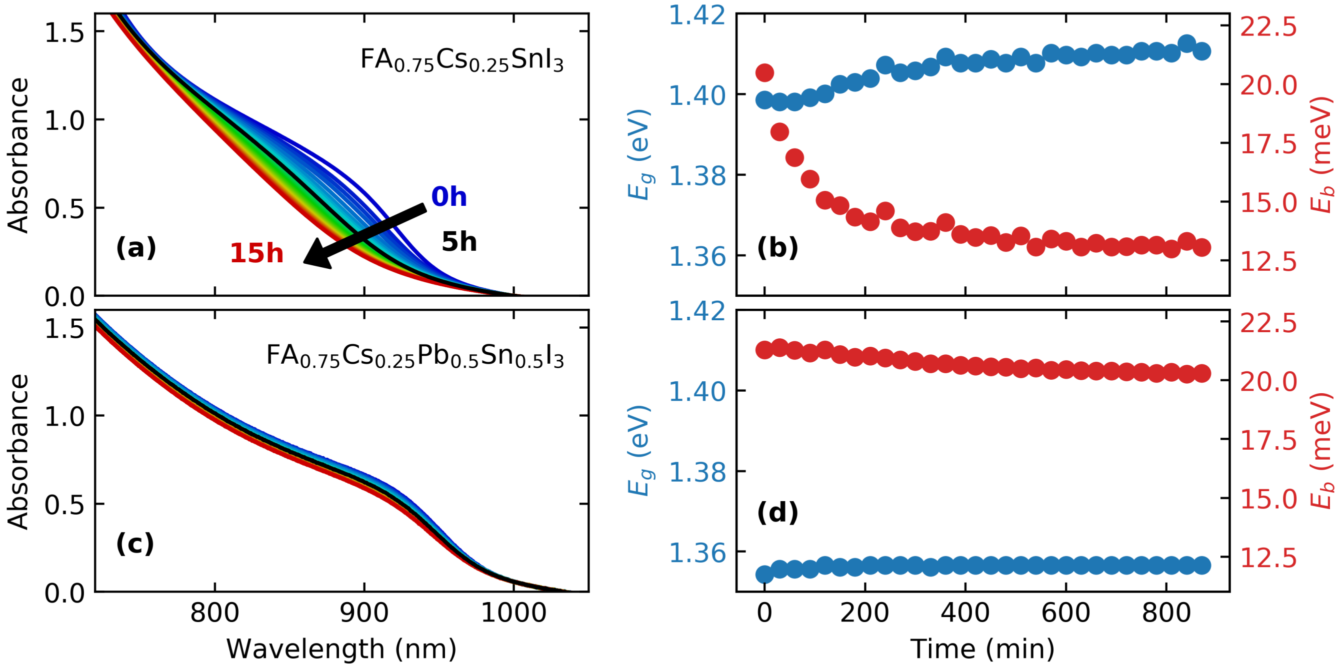

Figure 5.5: Absorbance spectra of an a) $FA_{0.75}Cs_{0.25}SnI_3$ and c) $FA_{0.75}Cs_{0.25}Pb_{0.5}Sn_{0.5}I_3$ thin-film recorded at 30 min intervals over ≈ 15 h of ambient-air exposure. The absorbance spectra at 5 h of exposure are highlighted in black solid lines for comparison with the time scales for OPTP data shown in Figure 5.1. The corresponding bandgap energy (E_g) and exciton binding energy (E_b) extracted for (c) $FA_{0.75}Cs_{0.25}SnI_3$ and d) $FA_{0.75}Cs_{0.25}Pb_{0.5}Sn_{0.5}I_3$ from Elliott fitting as detailed in Section 3.1.1.

mixed lead-tin $FA_{0.75}Cs_{0.25}Pb_{0.5}Sn_{0.5}I_3$ causing the observed optoelectronic degradation under air do not introduce free charge carriers into the conduction or valence bands. It is therefore proposed that accelerated charge-carrier recombination arising from air exposure of $FA_{0.75}Cs_{0.25}Pb_{0.5}Sn_{0.5}I_3$ is instead mediated by the introduction of a large density of deep trap states, whose energy level lies significantly further from the band edge than thermal energy at room temperature, and which do not electrically dope the material to a significant extent.[131]

5.2.3 THz Dark Conductivity

I further confirm the strongly enhanced presence of electrical doping in tin-only $FA_{0.75}Cs_{0.25}SnI_3$ in air, and the lack of major doping in its mixed lead-tin $FA_{0.75}Cs_{0.25}Pb_{0.5}Sn_{0.5}I_3$ counterpart, by performing measurements of THz conductivity spectra in the absence

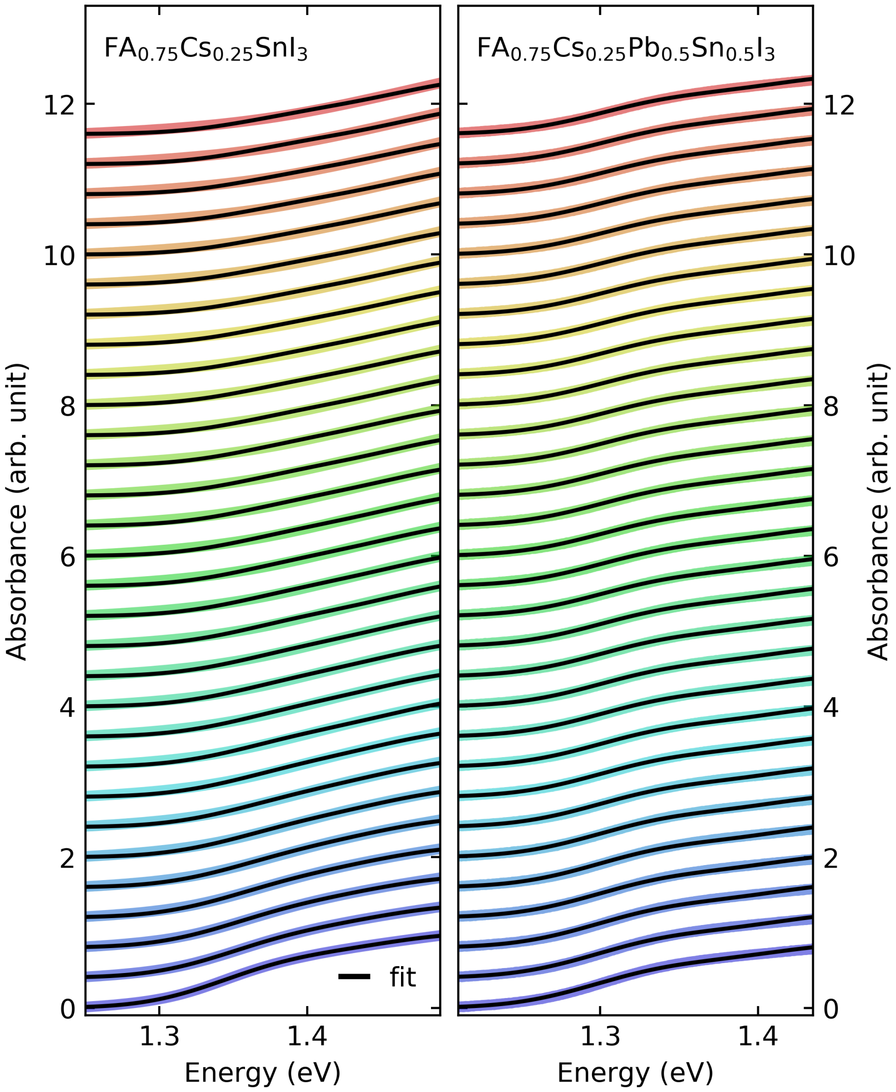

Figure 5.6: Elliott fits (black lines) to the absorption spectra (colored lines) of tin-only $FA_{0.75}Cs_{0.25}SnI_3$ and mixed lead-tin $FA_{0.75}Cs_{0.25}Pb_{0.5}Sn_{0.5}I_3$ perovskites for the first ≈ 15 h of ambient air exposure.

of photoexcitation during their degradation in ambient air. Dark conductivity spectra shown in Figure 5.7(a,b) confirm the monotonic increase of background doping density for $FA_{0.75}Cs_{0.25}SnI_3$ with air-exposure time, in contrast to $FA_{0.75}Cs_{0.25}Pb_{0.5}Sn_{0.5}I_3$ (Figure 5.7(d)) which did not exhibit signs of electric background doping or changes in dark conductivity with air exposure within my detection limit. It is noted that such dark THz conductivity spectra are equivalent to measurements of the dielectric function at THz frequencies. As such, these may provide information about not only the presence of a

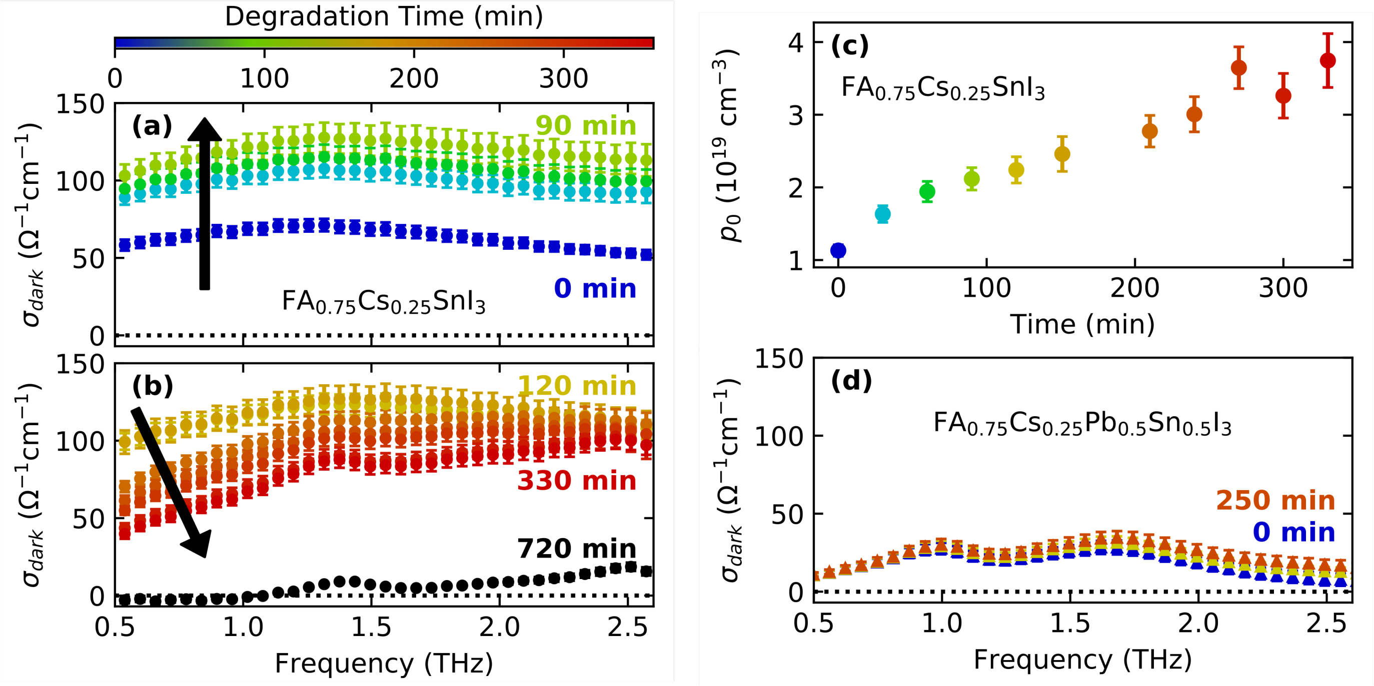

Figure 5.7: a,b) Dark conductivity spectra of a $FA_{0.75}Cs_{0.25}SnI_3$ thin film measured at different degradation times in ambient air as indicated by the color-coded legend. c) Estimated background hole density extracted from spectra in (a) and (b), as detailed Section B.2, plotted against exposure time in ambient air. d) Dark conductivity spectra of a $FA_{0.75}Cs_{0.25}Pb_{0.5}Sn_{0.5}I_3$ thin film at different degradation times in ambient air.

background charge-carrier density arising, e.g., from unintentional doping, but also on vibrational absorption falling into the THz frequency region. In the analysis below, I disentangle such effects (additional details are provided in Section B.2. Measurements of the dark conductivity spectra were performed with terahertz time-domain spectroscopy (THz-TDS) at different air-exposure times, as detailed in Section 3.4.1.

For tin iodide perovskites, a recent analysis of dark THz conductivity spectra has shown these to be dominated by relatively broad phonon modes and a strong free-charge response arising from a substantial hole background density.[33] Such Drude-like conductivity of charge carriers in metal halide perovskites is known to be spectrally flat across the THz frequency range, owing to the relatively fast momentum scattering time.[33,34] It is therefore expected that the dark conductivity response of tin iodide perovskites to shift vertically toward higher conductivities as the density of background charge carriers increases with air-exposure time, which is exactly what I observe for $FA_{0.75}Cs_{0.25}SnI_3$ for early degradation times (Figure 5.7(a)) over the first $\approx 90\,\mathrm{min}$ of air exposure. I note however that at later times beyond $\approx 120\,\mathrm{min}$ in air, the background conductivity decreases again in amplitude (Figure 5.7(b)) which I attribute to the decrease of the charge-carrier mobility observed in Figure 5.1(c) that accompanies a continued increase in background hole density arising from the tin-vacancy formation. To disentangle such effects, I separate the two contributions of the hole mobility μ_h and the background hole density p_0 to the dark conductivity, given by $\sigma = ep_0\mu_h$, considering the values of mobility extracted from OPTP measurements (Figure 5.1(c)) at various degradation times and selecting a spectral range for analysis where phonons make little contribution (as detailed in Section B.2). I present the background hole density extracted in this manner for $FA_{0.75}Cs_{0.25}SnI_3$ in Figure 5.7(c), and find that it exhibits a monotonic increase with degradation time in air, rising from 1×10^{19} to $4{\times}10^{19}\,\mathrm{cm}^{-3}$ after $\approx 5\,\mathrm{h}$ in air. This increase in unintentional doping further corroborates the formation of shallow defect acceptor states, such as tin vacancies, as the main air-degradation mechanism in tin-only $FA_{0.75}Cs_{0.25}SnI_3$.

Such background doping is in contrast to what is observed for the mixed lead-tin $FA_{0.75}Cs_{0.25}Pb_{0.5}Sn_{0.5}I_3$ film (Figure 5.7(d)), whose dark conductivity spectrum remains mostly unchanged with degradation time and simply displays two vibrational peaks associated with optical phonon modes of the metal-iodide sublattice.[33,34] The lack of change of these spectra with time and the absence of a spectrally flat Drude-like (free-charge) conductivity signature implies that for $FA_{0.75}Cs_{0.25}Pb_{0.5}Sn_{0.5}I_3$, any unintentional doping arising from tin vacancies is comparatively low ($<10^{18}\,\mathrm{cm}^{-3}$, according to my detection limit, as detailed in Section B.2), despite the high (50%) content of tin in the structure and the optoelectronic degradation observed in Figure 5.1. This result is consistent with the earlier finding that exciton screening and Burstein-Moss effects are not observed in the absorption spectra of this material. It is, therefore, concluded that the air degradation of $FA_{0.75}Cs_{0.25}Pb_{0.5}Sn_{0.5}I_3$ predominantly involves the formation of defect states deep within the bandgap, i.e., defects whose energy levels do not lie close to or within the bands. These deep traps effectively induce trap-mediated recombination, increasing the monomolecular recombination rates, but do not curtail the charge-carrier mobilities as severely as the charged tin vacancies prevalent in tin-only iodide perovskites.

Furthermore, the THz dark conductivity spectrum of tin-only $FA_{0.75}Cs_{0.25}SnI_3$ also allows us to garner additional information on its degradation products under prolonged air exposure. After 12 h in air (black dots in Figure 5.7(b)) the spectra reveal two new peaks appearing after degradation, which occur at higher frequencies (at 1.4 and 2.5 THz) than those associated with the optical modes of the metal-iodide perovskite sub-lattice[33] and therefore must be of a different origin. It is noted that the clear visibility of these peaks suggests that charge-carrier mobilities have now been so significantly impacted by degradation that any background hole densities present can no longer effectively contribute to the overall photoconductivity. I deduce that these new phonon modes arise from vacancy-ordered double perovskite formation in the material resulting from tin oxidation in the presence of air. Previously reported degradation products from the decomposition of $ASnI_3$ perovskites in ambient air include SnI_4, SnO_2 as well as a double-perovskite A_2SnI_6,[41,145,163,164] arising from the better stability of the 4+ oxidation state over the 2+ state in tin. Since every other metal site of the vacancy-ordered perovskite is empty, the equivalent reduced ionic mass of the crystalline structure is lower than for a standard ABX_3 perovskite. From a simplified picture of vibrations in a diatomic chain, this lowering of ionic reduced mass is expected to increase the frequency of oscillation (phonon) modes compared to those seen in the equivalent ABX_3 perovskite structure. The two peaks at 1.4 and 2.5 THz are therefore attributed to the optical phonon modes of the equivalent vacancy-order double perovskite, and it is noted that those frequencies indeed agree with the transverse-optical phonon modes of vacancy-ordered Cs_2SnI_6 previously reported,[165] as fully discussed in Section B.3. Therefore, prolonged air exposure of $FA_{0.75}Cs_{0.25}SnI_3$ ultimately leads to tin oxidation and chemical decomposition toward vacancy-ordered double perovskites, following on from the initial tin vacancy formation.

5.2.4 XRD Measurements

Finally, I investigate the structural properties of the $FA_{0.75}Cs_{0.25}SnI_3$ and $FA_{0.75}Cs_{0.25}Pb_{0.5}$ $Sn_{0.5}I_3$ films through X-ray diffraction (XRD) measurements, in order to assess changes occurring during their degradation in ambient air over a prolonged time of air exposure. The evolution of the second-order quasi-cubic (200) X-ray diffraction peaks is presented in Figure 5.8 over an air-exposure time window of 72 h (full XRD spectra over a wider 2θ range in Figure 5.9 and 5.10). It is found that both materials exhibit only relatively minor structural changes over the first few hours of air exposure, during which the optoelectronic properties of the film have been found to deteriorate significantly, as highlighted by the OPTP and THz-TDS measurements discussed above (Figure 5.1). This observation further confirms that the optoelectronic degradation I reported on for air exposure over the first ≈ 5 h was a result of point-defect formation, rather than full structural deterioration of the semiconductors. It is noted that for longer air exposure, however, the XRD peak amplitude decreases substantially, suggesting a loss of the perovskite structure and a potential formation of degradation products.

For tin-only $FA_{0.75}Cs_{0.25}SnI_3$, an extended air exposure (≈ 72 h) results in the (200) perovskite peak no longer being observable, but a broad, weak peak instead arises at a higher diffraction angle 2θ (Figure 5.8(a) inset). XRD peaks of vacancy-ordered double perovskites are expected to appear at a higher diffraction angle than those of their equivalent perovskite counterpart, since the enhanced oxidation state of tin ions decreases the lattice parameter, in agreement with previous reports.[145,163,164,166] Therefore, I attribute the broad peak observed for tin-only $FA_{0.75}Cs_{0.25}SnI_3$ to the

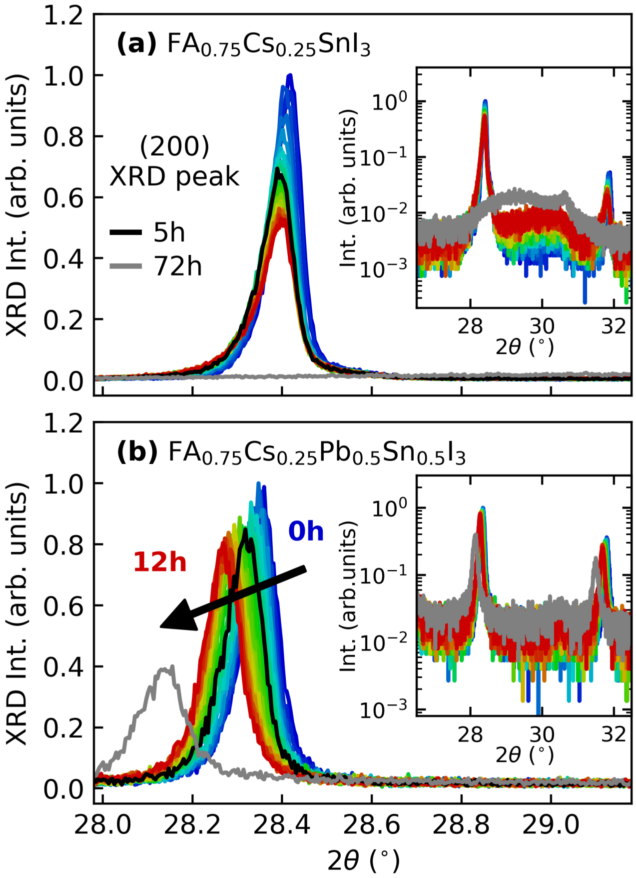

Figure 5.8: (200) X-ray diffraction peaks of a) $FA_{0.75}Cs_{0.25}SnI_3$ and b) $FA_{0.75}Cs_{0.25}Pb_{0.5}Sn_{0.5}I_3$ thin films measured at 30 min intervals over the first ≈ 12 h of ambient-air degradation and again at 72 h. Insets show the results of the same measurement over a broader angle range and plotted on a logarithmic scale. The spectra at 5 h exposure time are highlighted with a black solid line for comparison with OPTP and THz-TDS data, and the spectra at 72 h are denoted with gray lines.

formation of a vacancy-ordered double perovskite, in agreement with my analysis of dark conductivity spectra above. The broad nature of the peak indicates that the size of such double perovskite domains must be small, leading to X-ray diffraction off relatively few lattice planes for each such inclusion. Prolonged air-induced degradation of $FA_{0.75}Cs_{0.25}SnI_3$ therefore ultimately leads to a highly structurally, and most likely also compositionally, disordered material.

The mixed lead-tin $FA_{0.75}Cs_{0.25}Pb_{0.5}Sn_{0.5}I_3$ film, on the other hand, shows a much slower decrease in XRD peak amplitude (Figure 5.8(b)) and an absence of any discernable vacancy-ordered double perovskite, even after 72 h of ambient air exposure. The relatively

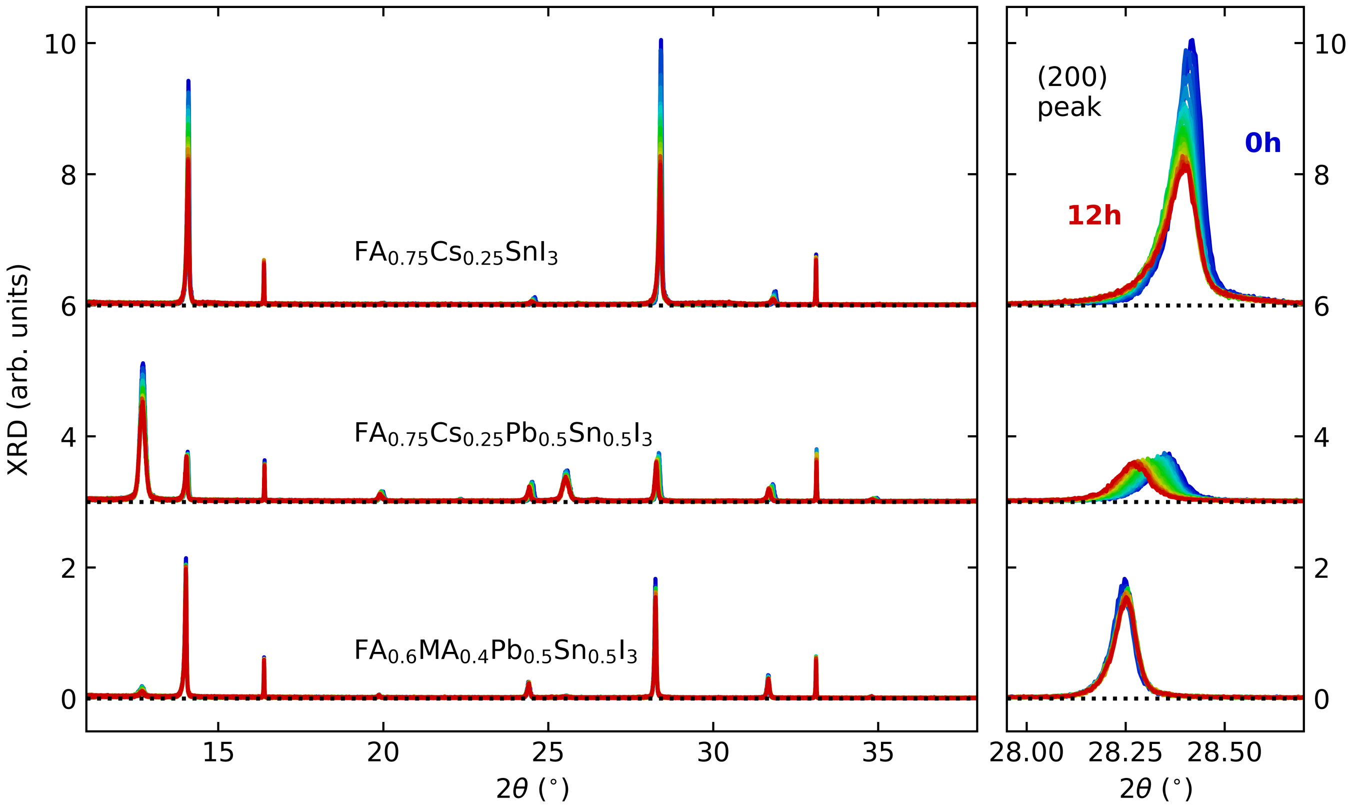

Figure 5.9: Continuously recorded XRD patterns over ≈ 12 h of ambient air exposure of thin films of $FA_{0.75}Cs_{0.25}SnI_3$, $FA_{0.75}Cs_{0.25}Pb_{0.5}Sn_{0.5}I_3$, and $FA_{0.6}MA_{0.4}Pb_{0.5}Sn_{0.5}I_3$ perovskite. The right-hand panel is a zoomed-in view of the (200) peak.

slow deterioration in its structure (Figure 5.8) in the presence of a much more rapid decline in its optoelectronic properties (Figure 5.1) again suggests that the former is caused by the introduction of point defects that leave the perovskite structure fundamentally intact. However, a small increase in the lattice parameter of the crystal structure with degradation is evidenced by the XRD peak shifting to a lower 2θ angle with prolonged air exposure. I attribute this shift to an effect related to the A-cation composition ($FA_{0.75}Cs_{0.25}$), given that the same measurements were conducted on a $FA_{0.6}MA_{0.4}Pb_{0.5}Sn_{0.5}I_3$ film (presented in 5.9 and 5.10) but reveal a lack of such lattice contraction.

To summarize, I have shown that tin-only $FA_{0.75}Cs_{0.25}SnI_3$ perovskite degrades in air via heavy p-type self-doping of the semiconductor, originating from the formation of a high density of shallow tin-vacancy point defects, in agreement with previous reports.[32–34,150]

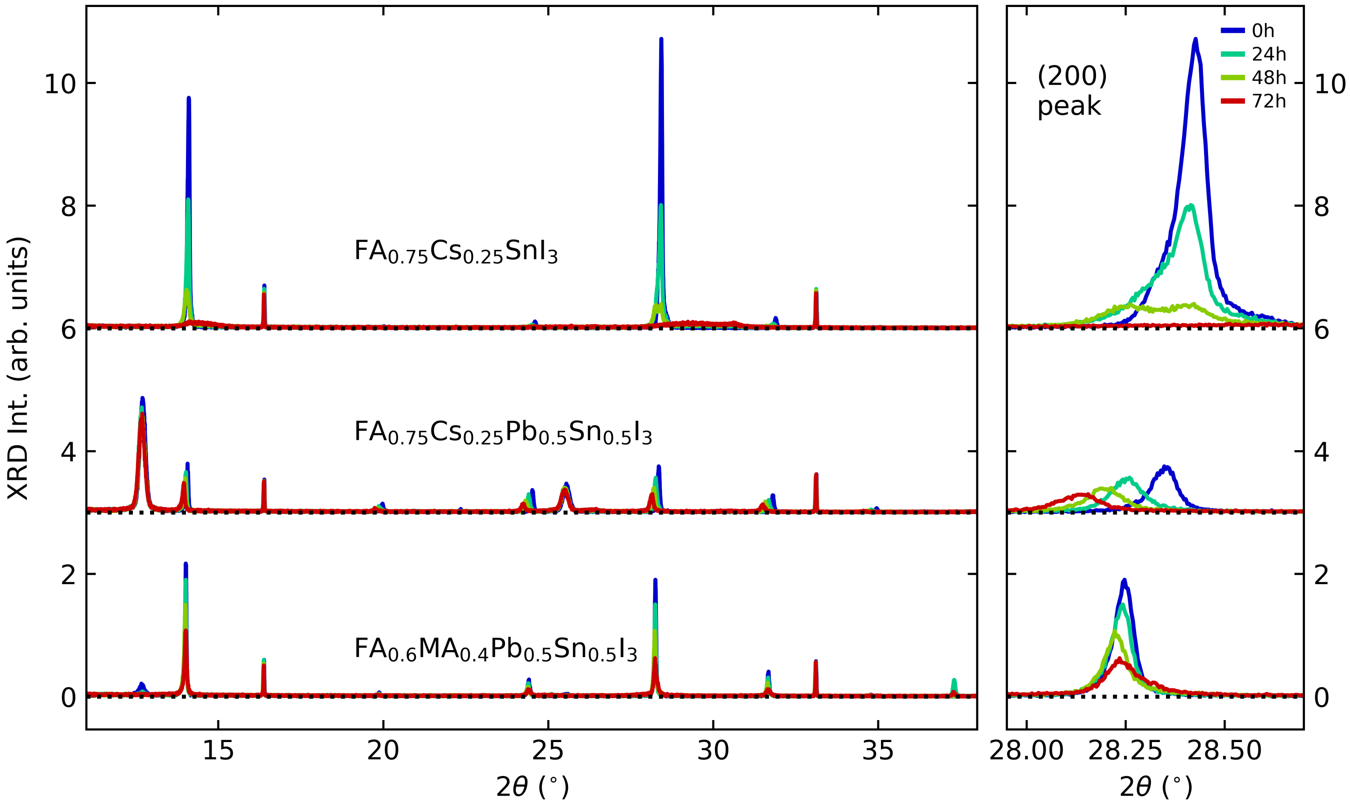

Figure 5.10: Continuously recorded XRD patterns over ≈ 72 h of ambient air exposure of thin films of $FA_{0.75}Cs_{0.25}SnI_3$, $FA_{0.75}Cs_{0.25}Pb_{0.5}Sn_{0.5}I_3$, and $FA_{0.6}MA_{0.4}Pb_{0.5}Sn_{0.5}I_3$ perovskite. The right-hand panel is a zoomed-in view of the (200) peak.

SnF_2 addition has been widely and successfully used as an additive to suppress such tin-vacancy formation during the deposition process.[33,161] However, my work here revealed that air degradation of mixed lead-tin $FA_{0.75}Cs_{0.25}Pb_{0.5}Sn_{0.5}I_3$ instead results in the formation of much deeper trap states, with electrical doping being far less prominent in the material than in the tin-only equivalent. There have been suggestions based on theoretical calculations[30] that mixed lead-tin perovskites (specifically $MAPb_{0.5}Sn_{0.5}I_3$) might potentially be free of trap states energetically situated near mid-bandgap. However, energy levels calculated for tin vacancies, iodide vacancies and tin interstitials in such mixed lead-tin perovskites all lie within the bandgap, and, importantly, are situated more than the thermal energy at room temperature ($k_bT \approx 25$ meV) away from the band edges,[30] therefore these are potential candidates for the trap-mediated recombination pathways observed herein. It is noted that the formation of tin and iodide vacancies is also consistent with a recent surface probe of the degradation of lead-tin perovskites employing X-ray photoelectron spectroscopy.[167] It is also noted that while tin vacancies are dominant shallow defect states in tin-only perovskites, the lowering of the valence band upon substitution of lead (owing to enhanced spin-orbit coupling) may turn such vacancies into deep trap states in mixed tin-lead perovskites,[30] thus trap-mediated recombination in the absence of significant self-doping may occur, as is observed. However, it has been postulated that tin-vacancy formation is suppressed once a significant fraction of tin has been replaced with lead in these perovskites.[30,32,41,158] Given that $FA_{0.75}Cs_{0.25}Pb_{0.5}Sn_{0.5}I_3$ shows substantially more rapid increase in charge-carrier recombination rates with air exposure than $FA_{0.75}Cs_{0.25}SnI_3$ (Figure 5.1(b)), it is therefore perhaps more likely that such deep-trap formation in intermediate tin-lead compositions is caused by iodide vacancies, which form prominent deep-level defects in lead iodide perovskites.[30,133,135,168] Overall, I highlight the differences I observe in the electronic behavior of these perovskites, contrasting shallow, hole-donating defect states formed in tin-only perovskites, with deep-trap states formed in mixed lead-tin perovskites, which do not significantly contribute to background doping, but lead to optoelectronic deterioration. I, therefore, suggest further investigation into novel fabrication methods of mixed lead-tin perovskites, including the exploration of an iodide-rich environment to prevent iodide vacancies, and further optimization of the tin-additive concentration in order to carefully balance the trade-off between tin-vacancy and tin-interstitial formation. It is also noted that a stronger focus is needed on eliminating tin inhomogeneities[29] as these may result in lead-tin perovskites with nominally optimized tin stoichiometry, but exhibiting a combination of locally tin-rich environments where tin interstitials are dominant, and locally tin-poor environment where tin vacancies are dominant. Since either defect type represents an electronic trap, a simple addition of SnF_2 may be insufficient if this treatment fails to induce fully homogeneous tin addition on the metal sites. An alternative possibility is the formation of SnO_2 within the mixed lead-tin perovskite structure during air-degradation, which has been suggested in previous reports and could also result in a deterioration of optoelectronic properties of the semiconductor.[32,41,145,149,167] Owing to the abundance of the defect states present within SnO_2 inclusions and at their interface with perovskite crystals,[169–175] even a relatively low density of SnO_2 may decrease the charge-carrier recombination rate, without much affecting the charge-carrier mobility measured with terahertz spectroscopy. The amorphous and disordered nature of these SnO_2 domains means that they can rarely be observed in XRD patterns, providing a plausible explanation for my findings of declined optoelectronic properties in tin-lead perovskites in the absence of discernable changes in XRD patterns.[176] It is noted that thin-film fabrication in a tin-poor environment may also be able to reduce such SnO_2 formation after air exposure.

5.3 Conclusion

In conclusion, I have investigated the differences in degradation pathways between $FA_{0.75}Cs_{0.25}SnI_3$ and $FA_{0.75}Cs_{0.25}Pb_{0.5}Sn_{0.5}I_3$ perovskite thin films in ambient air. I first identified self p-doping via tin-vacancy formation as the main degradation pathway in the tin-only perovskite, in agreement with previous reports. Such p-doping was evidenced by the Burstein-Moss effect and a decrease of exciton binding energy (E_b) of the tin-only perovskite observed during air exposure, as well as an increase in the Drude-like dark conductivity spectrum of the film from the enhancement of the free charge-carrier population. A vacancy-ordered double perovskite structure was also identified as a degradation product, as evidenced by its phonon modes and the appearance of new XRD peaks. The tin-only perovskite also simultaneously underwent deterioration of the optoelectronic properties resulting from charge-carrier recombination of doping-induced holes with photoexcited electrons. These holes, together with negatively charged tin-vacancy complements, act as additional scattering centers, decreasing the momentum scattering time of free charge carriers. Such optoelectronic degradation was observed as a decrease in the charge-carrier mobility (μ) and an increase in charge-carrier recombination rate (k_1), and correspondingly a decrease in the charge-carrier diffusion length (L_D). In contrast, air exposure of the mixed lead-tin perovskite predominantly resulted in the formation of deep trap states rather than significant electronic doping. The lack of any discernable change in the dark conductivity spectrum of the lead-tin perovskite, as well as only minor changes to its absorption spectrum during hours of air exposure, suggest that shallow, hole-donating defect states are not the most abundant defects forming in the mixed tin-lead perovskite upon air exposure. However, despite the lack of significant electronic doping or structural degradation, $FA_{0.75}Cs_{0.25}Pb_{0.5}Sn_{0.5}I_3$ exhibited deterioration of its optoelectronic properties upon air exposure, implying the formation of deep-level defect states that accelerate the monomolecular recombination of free carriers. SnF_2 addition has been successful in suppressing the tin-vacancy formation in tin-only perovskite, but my work suggests that this may not necessarily be the right approach for mixed lead-tin perovskites. The $FA_{0.75}Cs_{0.25}Pb_{0.5}Sn_{0.5}I_3$ films examined here were produced with a 10% SnF_2 addition, currently the standard for absorber layers incorporated in high-performing perovskite solar cells,[153–156] yet they are still liable to deep-trap formation in ambient air. Tin interstitials and iodide vacancies are likely the prominent defect states formed during air degradation of mixed lead-tin perovskites. In addition, given the shifts in predominantly the valance band, any remnant tin vacancies may now form traps deeper in the bandgap, rather than the shallow hole-donating defect states they constitute in tin-only counterparts.[30] I, therefore, suggest that the suppression of such defect states requires further investigation into iodine-rich fabrication environments, as well as precise balancing of tin content in combination with further exploration of treatments that allow for better tin homogeneity control. My study highlights the urgent need for the development of additional and alternative passivation methods tuned specifically toward mixed lead-tin perovskites. Such treatments will ultimately improve air stability, enabling all-perovskite tandem devices to become commercially viable with excellent long-term power conversion efficiencies.

6

Contrasting Ultra-Low Frequency Raman and Infrared Modes in Emerging Metal Halides

Contents

The work presented in this chapter has been published in:

Lim, V. J.-Y., Righetto, M., Yan, S., Patel, J. B., Siday, T., Putland, B., McCall, K. M., Sirtl, M. T., Kominko, Y., Peng, J., Lin, Q., Bein, T., Kovalenko, M., Snaith, H. J., Johnston, M. B., Herz, L. M. 'Contrasting Ultra-Low Frequency Raman and Infrared Modes in Emerging Metal Halides for Photovoltaics'. *ACS Energy Letters*, **2024**, 9, 41274135. (Ref. [177])

V. J. -Y. L. performed all the experiments and data analysis, and wrote the manuscript. M. R. and L. M. H. supervised. M. R. and T. S. helped with building the Raman setup.

S. Y., J. B. P., B. P., K. M. M., M. T. S., Y. K., and J. P. fabricated the samples. All authors discussed the results and reviewed the manuscript.

6.1 Introduction

Lattice vibrations influence a plethora of fundamental material properties, ranging from dielectric and elastic responses to thermal and electronic conductivities.[6] For semiconductors, coupling of phonons to charge carriers is critical to several photophysical processes–hot carrier cooling,[178,179] dynamic disorder,[180] and charge-carrier recombination[181] – and most importantly imposes fundamental limits on charge-carrier transport.[182] Metal-halide perovskites (MHPs) have attracted much attention for their excellent charge-carrier transport properties and their impressive potential in photovoltaic applications.[183] Electron–phonon coupling in MHPs has been the subject of intense debate, and has often been proposed as the origin of their exceptional properties.[184,185] Phonon frequencies in MHPs are lower compared to those in conventional inorganic semiconductors, as a result of heavier ions (e.g., Pb^{2+}, I˘) and mixed covalent-ionic bonds leading to a ‘soft’ lattice.[185] These low phonon frequencies have been stipulated to yield defect tolerance,[186] anharmonicity of phonons[187] and even a ‘liquid-like’ nature of the material.[188,189] In addition, charge-carrier properties are shown to be significantly influenced by structural fluctuations in MHPs, especially those induced by low-frequency vibrations.[184,190,191]

Understanding the role of the vibrational structure in determining the properties of MHPs is thus also crucial more generally for the development of a new family of high-performance semiconductors. Despite their ideal optoelectronic properties, MHPs can be affected by toxicity and structural, thermal and chemical instabilities.[192] As a result, alternative metal-halide compositions and related semiconductors, often referred to as ‘perovskite-inspired’ materials, are currently being discovered and explored for next-generation photovoltaic devices and other applications.[193] Therefore, identifying the vibrational fingerprints of a promising emergent semiconductor is a fundamental step in the quest for developing such next-generation materials.

Raman spectroscopy in the THz region, also known as ultra-low frequency (ULF) Raman, is a well-established approach for the study of lattice dynamics of MHPs. It has been widely reported that MHPs exhibit a broad Raman response in this region, known as the 'central Raman peak',[194–196] that increases in magnitude toward the elastically scattered (zero-frequency) light peak. Despite several studies on the low-frequency Raman response of MHPs, a consensus on the origin of this phenomenon has not yet been reached. There have been some initial assignments of this phenomenon to the 'liquid-like' nature of the perovskite lattice[188,189,197] causing local polar fluctuations,[194] temperature-activated A-cation rotation,[198] or octahedral tilting from cation lone pairs.[199] IR and Raman spectroscopies can provide access to complementary information on the vibrational structure of semiconductors and a detailed comparison can be of unique value to a full understanding of the vibrational properties of MHPs. Crucially, the central Raman response visible in Raman spectra has not been reported in IR spectra,[200,201] for reasons unexamined to date. However, the different nature of these responses–Raman is a light-scattering measurement, while IR spectroscopy measures light absorption–requires a careful comparison that considers the different transition matrices and the selection rules associated with these two techniques.

In this chapter, I systematically investigated the low-frequency vibrational spectra recorded for a range of metal-halide semiconductors with relevance to photovoltaic applications. This work elucidates the origin of the low-frequency vibrational response from these materials through a careful combined analysis of Raman and IR spectra. By studying a wide range of metal-halide compositions–in both thin film and single crystal form–and leveraging combined IR and Raman information, I was able to examine the origin of the central Raman response, and could rule out several potential explanations, including extrinsic defects, a double-well instability that may arise from octahedral tilting and cation lone pairs, and a boson peak that may be associated with a soft, 'liquid-like' nature of the lattice. I suggested that instead, differences in the decay channels for Raman- and IR-active phonons, as well as a thermal population factor affecting solely the Raman intensity spectrum, are responsible for the peculiar low-frequency Raman response observed in many of these semiconductors.

6.2 Results and Discussion

To investigate the central Raman response, I employed ultra-low frequency (ULF) ($>10\,\mathrm{cm}^{-1}$, $0.3\,\mathrm{THz}$) Raman and THz time-domain spectroscopy (THz-TDS), ideal techniques for probing Raman- and IR-active phonon modes in this range. For ULF Raman, a continuous wave (CW) pump laser with 900 nm wavelength was used, corresponding to photon energies below the band gap energy for all materials investigated, to avoid degradation from photoexcitation and contributions from resonant Raman conditions which may skew the intensities of certain modes.[202] For THz-TDS, the transmission of THz-frequency pulses through thin films deposited on z-cut quartz was measured using electro-optic detection in the time domain, and the transients were Fourier transformed to yield the THz spectrum. Full descriptions of the spectroscopic techniques are given in Section 3.2 and 3.3. Here, I investigated a range of metal halide semiconductors currently being explored for photovoltaic and optoelectronic applications, including the lead-halide perovskites $\mathrm{MAPbI_3}$, $\mathrm{FAPbI_3}$, $\mathrm{MAPbBr_{1.5}I_{1.5}}$, $\mathrm{MAPbBr_3}$, $\mathrm{CsPbBr_3}$ and their precursor $\mathrm{PbI_2}$, and the emerging metal halides $\mathrm{Cs_2AgBiBr_6}$ and $\mathrm{Cu_2AgBiI_6}$, as well as AgI for comparison. I note that in the literature, single crystals have been preferred for Raman investigations owing to their higher Raman scattering intensity and possibility for polarization-dependent measurements.[194,196,198,199,203,204] However, to obtain an analysis more relevant to photovoltaic devices, I here explored thin films deposited on z-cut quartz, while also demonstrating comparison with single crystals for a subset of the materials investigated - fabrication details can be found in Section C.1.

6.2.1 ULF Raman Spectra

I examined the ULF Raman spectra of the various metal-halide semiconductor thin films to probe for the presence of the central Raman response, as shown in Figure 6.1. All the MHPs ($MAPbI_3$, $FAPbI_3$, $MAPbBr_{1.5}I_{1.5}$, $MAPbBr_3$, $CsPbBr_3$) exhibit such a central Raman peak, as do Cu_2AgBiI_6 and AgI, while PbI_2 shows only a weak low-frequency response in that region. $Cs_2AgBiBr_6$ does not exhibit any central Raman peak, in agreement with reports by Cohen et al.[203] For clarity, a zoomed-in plot of the Raman spectra of AgI and $Cs_2AgBiBr_6$ can be found in Figure 6.2. It is worth noting that from ideal point-group analysis, materials with perfect cubic perovskite structure should not possess any Raman-active phonons.[205] Therefore, for MHPs to exhibit a strong low-frequency Raman response, some disorder or anharmonicity needs to be present.[206,207] Alternatively, this low-frequency response could be caused by multiphonon processes,[208,209] but no higher harmonics of this response appear visible in the Raman spectra. Moreover, I note that sharp features in the Raman response of the metal-halide thin films are superimposed with the broad central Raman response, similar in appearance to optical phonon modes apparent in IR spectra discussed below. This coexistence of a broad feature with more sharply defined phonon peaks suggests that not just one type of lattice dynamic causes the low-frequency Raman response of MHPs.

I start by discussing and assessing–based on the Raman data reported in Figure 6.1 and prior studies–the main factors proposed in the literature as origins of the central Raman response for MHPs, in the following order: the presence of a double-well potential from A-cation lone pairs or octahedral tilting, extrinsic disorder from defects and impurities, and a boson peak response arising from a soft ‘liquid-like’ nature of the structure.

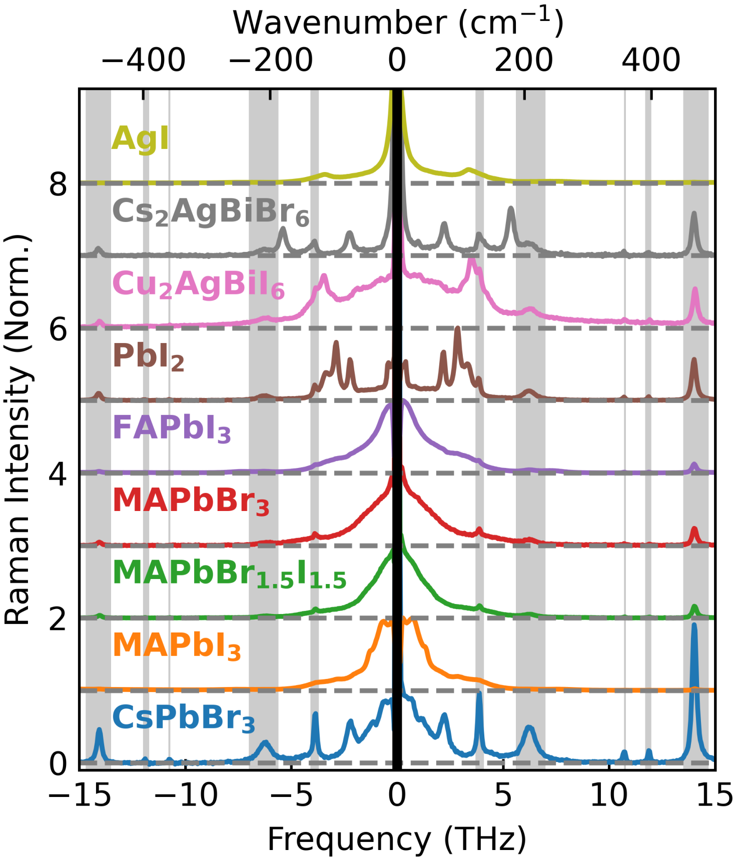

Figure 6.1: Raman spectra of a set of thin-film metal halides, as indicated. The central Rayleigh scattering peak is hidden with black, and the phonon responses of the z-cut quartz substrate are indicated with gray throughout the spectra. A CW laser with wavelength of 900 nm was used as the light source, and the Raman signal was collected in a backscattering geometry. Rayleigh scatter was suppressed with volume-Bragg notch filters. Experimental details can be found in Section 3.3.

The presence of a double potential well in the lead halide octahedral cage $[\mathrm{PbX_6}]^{-4}$ and the dynamic instability associated with this lattice potential has been intensely discussed in the literature for MHPs.[206,210–213] Structural distortion in the perovskite lattice associated with this potential could explain the presence of the low-frequency Raman response, as a result of deviation from the perfect cubic structure. Recently, the double-potential-well model has also been invoked to account for the anomalous temperature dependence of the Raman intensity of some oxide and metal-halide perovskite materials.[206] Here, I note that the presence of a double-well potential in MHPs can be intimately connected with a stereochemically expressed $6s^2$ lone pair from the $\mathrm{Pb^{2+}}$

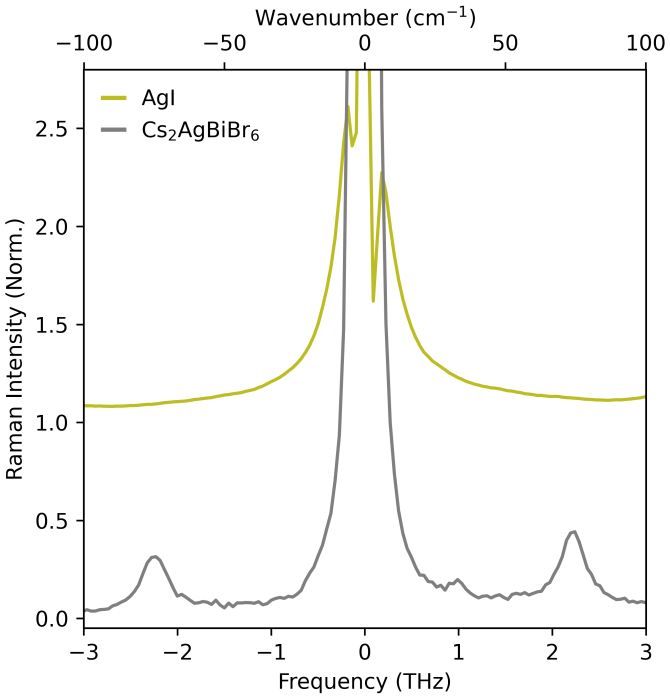

Figure 6.2: Normalised Raman intensity spectra of AgI and $Cs_2AgBiBr_6$ thin films, focusing on the narrow range close to the central, elastically scattered peak. A CW laser with wavelength 900 nm was used as the light source, and the Raman signal was collected in a back-scattering geometry. Rayleigh scatter was suppressed with volume-Bragg notch filters. Experimental details can be found in Section 3.3

cation.[212–214] Interestingly, no similar double-well potential is expected for AgI and for $CsSrBr_3$,[215] given the electronic configuration of the Ag^+ and Sr^{2+} cations ($[Kr]4d^{10}5s^0$) and ($[Kr]5s^0$) lack such ns^2 lone pairs. However, these materials also exhibit a broad low-frequency Raman response (see Figure 6.1 for AgI and Ref [215] for $CsSrBr_3$). As recently shown, $CsSrBr_3$ shows close structural similarity with $CsPbBr_3$, but unlike the latter exhibits no lone pair, yet both exhibit a broad central Raman response in their high-temperature cubic phase.[215] Overall, I therefore rule out the stereochemical activity of heavy cation lone pairs as the primary factor in determining the presence of a central Raman response in these metal halide semiconductors.

Octahedral tilting has been proposed as an alternative possible cause of instabilities related to double-well potentials in MHPs.[191,210,211] This effect is closely related to the Goldschmidt tolerance factor and therefore the choice of A-cation; when A-cations are smaller than the optimal size for bonding with BX_3, octahedral tilting may occur to compensate.[216–218] Octahedral tilting has been associated with zone-boundary vibrational instabilities giving rise to anharmonic double-well potentials;[216–218] therefore different A-cations are expected to cause octahedral tilting and double-well potentials to different extents. However, I observe that MHPs differing only in their A-cations (i.e., MA, FA and Cs in Figure 6.1, as well as MHy[196] and 2D MHPs[219] reported in the literature, with differing values of the Goldschmidt tolerance factor) exhibit a very similar central Raman response. I therefore suggest that octahedral tilting cannot play a major role in the appearance of a central Raman feature either.

Another possible source of disorder may arise from extrinsic factors related to processing conditions, i.e. defects and interstitials, chemical inhomogeneity,[220] or crystallinity/grain boundaries. It has indeed been shown that defects and impurities can influence the low-frequency Raman response.[221,222] A defect can distort a unit cell which can oscillate between unit cells with different symmetries,[221] or an impurity can cause a strain field surrounding it, so both may in principle cause a central Raman response.[222] I aim to examine the presence of such effects in MHPs by comparing Raman measurements on thin films with those of single crystals, for materials with the same nominal composition, but with distinctly different defect densities. For MHPs in particular defect densities have been reported to be of the order of $\approx 10^{17}\,\mathrm{cm}^{-3}$ for thin films[223] and $\approx 10^{10}\,\mathrm{cm}^{-3}$ for single crystals,[133,223] therefore I contrasted ULF Raman spectra measured both for thin films and single crystals of $CsPbBr_3$ and $MAPbI_3$ in Figure 6.3(a, b). It can be seen that both forms of the same material exhibit very similar responses in the low-frequency region of the Raman spectra, for both compositions. I therefore conclude that such extrinsic sources of disorder are unlikely to be related to the central Raman response in MHPs.

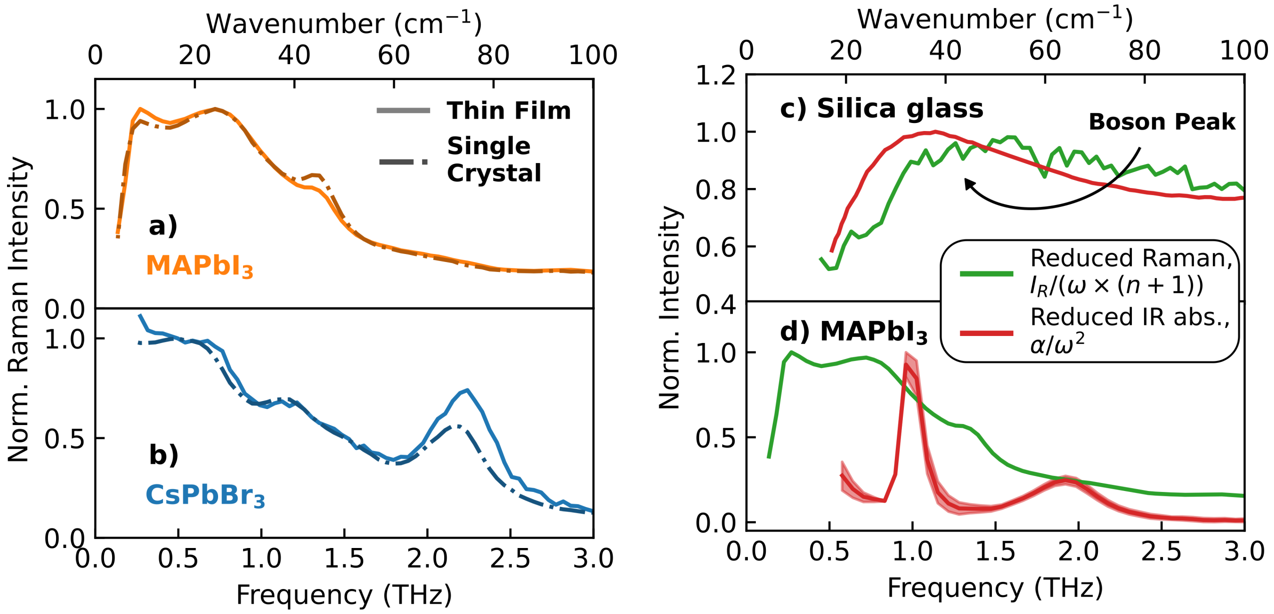

Figure 6.3: Normalized Raman spectra of thin films (solid lines) and single crystals (dash-dot lines) of (a) MAPbI$_3$ and (b) CsPbBr$_3$. (c) Reduced Raman (scheme 2) and reduced IR absorption spectra of amorphous silica glass, with the peak near 1 THz being the Boson peakarising from the liquid-like nature of amorphous silica glass. IR absorption data were taken from Ref [224]. (d) Normalized reduced Raman andreduced IR absorption spectra of MAPbI$_3$ thin film on z-cut quartz. The reduced Raman spectrum is given by $I_{\mathrm{R}/(\omega\times(\mathrm{n}+1))}$, where IR is the measured Raman intensity, and the reduced IR spectrum is given by α/ω_2, where α is the measured THz IR spectrum (scheme 2). A laser wavelength of 900 nm was used for non-resonant Raman spectroscopy, and THz-TDS was employed for acquisition of the IR absorption spectrum, as detailed in Section 3.2 and 3.3. IR spectra for further metal-halide semiconductors are provided in Figure 6.4.

6.2.2 Comparison Between Raman and IR Spectra

I further probe whether the central Raman peak may form as a result of a ‘liquid-like’ nature that has been postulated for MHPs[188,189] owing to their exceptionally soft lattice.[225] An amorphous material may exhibit a low-frequency Raman response, known as the Boson peak,[226–231] because if disorder within a material is sufficiently high, selection rules will be lifted since each mode will no longer be localized in momentum space and cannot be characterized by a single wavevector.[232,233] Therefore, both optical and acoustic modes will contribute to the vibrational density of states (vDoS),[232,233] giving rise to an excess vDoS adding onto the Debye vDoS ($\propto \omega^2$).[229–231] This phenomenon has been identified as the primary cause for the presence of a low-frequency Boson peak

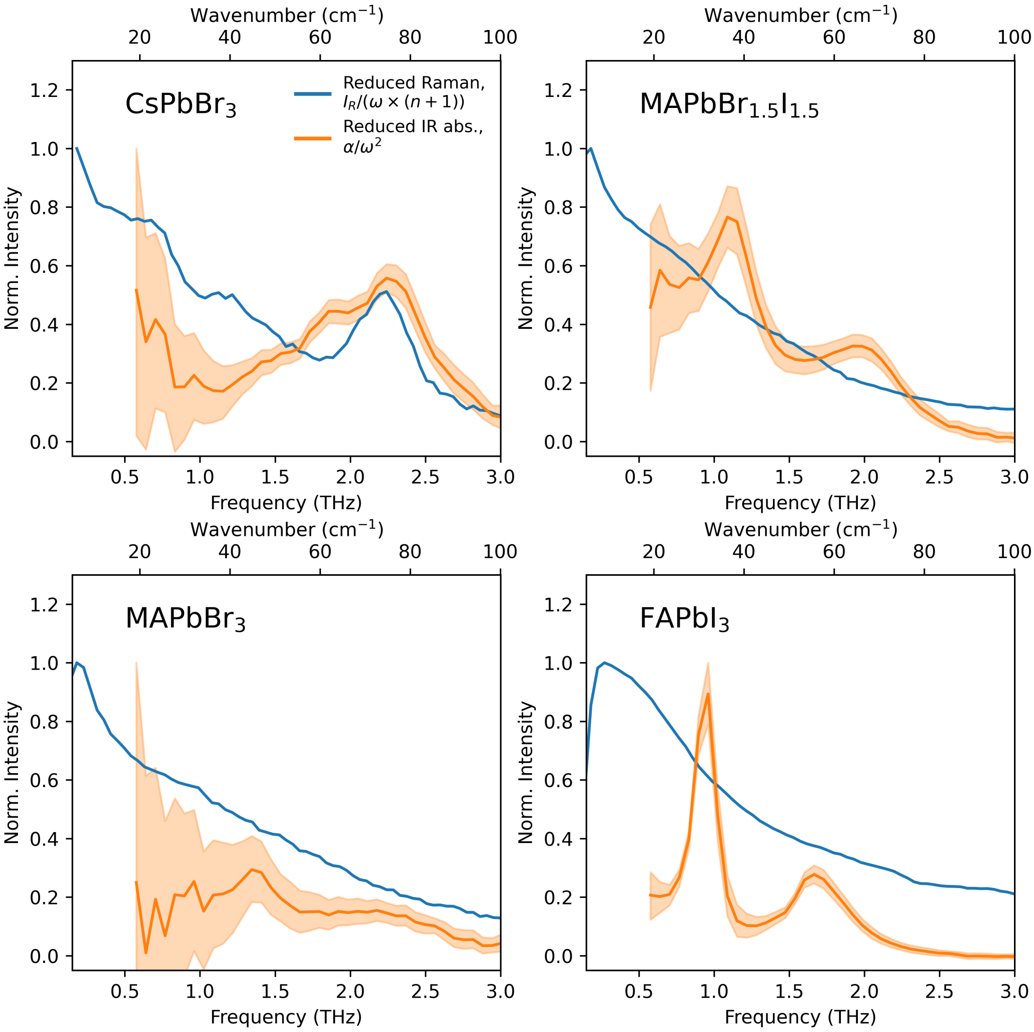

Figure 6.4: Normalised reduced Raman and reduced IR absorption spectra of CsPbBr$_3$, MAPbBr$_{1.5}$I$_{1.5}$, MAPbBr$_3$ and FAPbI$_3$ thin film on z-cut quartz. The reduced Raman spectrum is given by $I_{\mathrm{R}/(\omega\times(\mathrm{n}+1))}$, where I_{R} is the measured Raman intensity, and the reduced I_{R} spectrum is given by α/ω^2, where α is the measured THz IR spectrum. A laser wavelength of 900 nm was used for non-resonant Raman spectroscopy and THz-TDS was employed for acquisition of the IR absorption spectrum, as detailed in Section 3.2 and 3.3. The equivalent spectra for MAPbI$_3$ thin films are shown in Figure 6.3.

in amorphous materials such as silica glass.[224,231] Crucially, the lifting of selection rules implies that this additional vDOS contributes to signal amplitudes in both Raman and IR spectra.[229] However, to allow for clear observation of the Boson peak and for an accurate comparison between Raman and IR spectra, a spectral reduction must first be applied to the experimentally measured Raman and IR spectra to account for differences in the measurement techniques and yield a spectrum accurately describing the vDOS.

The intensity of the Raman signal generated by harmonic oscillators is proportional to $\omega/(n+1)$, and for disordered materials with short spatial correlation length, the Raman susceptibility χ'' can thus be described by the relation:[229,232,233]

$$\omega\chi'' = C_{\mathrm{Raman}} g = \frac{\omega I_{\mathrm{R}}}{n+1} \tag{6.1}$$

where C_{Raman} is the Raman coupling coefficient, g is the vDoS, I_{R} is the Raman intensity (as measured), and n is the Bose–Einstein distribution. I label this reduction scheme as scheme 1. The IR absorption spectrum has a simpler form:[229]

$$C_{\mathrm{IR}} g = \alpha \tag{6.2}$$

where C_{IR} is the IR coupling factor, and α is the IR absorption spectrum (as measured). I note that $I_{\mathrm{R},\alpha,\chi'',\mathrm{C_{Raman}},\mathrm{C_{IR}},\mathrm{g}}$, and n all depend on the frequency ω of the transmitted or scattered photon. Importantly, after the appropriate spectral reduction is applied to the measured signals, the reduced IR and Raman spectra are both representative of the vDoS, apart from the application of symmetry-related selection rules that may differ between the two techniques. In order to more clearly observe the Boson peak on top of a Debye vDoS ($\propto \omega^2$), I follow the standard literature approach to further reduce the IR and Raman intensities to α/ω^2 and $I/[\omega(n+1)]$, respectively, which are both proportional to g/ω^2,[226–229] and I label this as scheme 2.

There have been literature reports postulating a 'liquid-like' nature of MHPs, based on large phonon dynamics and polaron formation.[188,189] Such 'liquid-like' nature was also postulated as a possible cause for the central Raman response.[194,198,199] If MHPs are 'liquid-like', i.e. they have almost the response of an amorphous material, the Boson peak should be visible, and may indeed be the cause of the central Raman response.[229,234] I thus examine this question by comparing reduced Raman and IR spectra.[229,234] To ensure my method is correctly implemented, I first examine silica glass, an established amorphous material. As Figure 6.3(c) shows, for silica glass, the reduced IR and Raman spectra are indeed very similar (IR spectrum taken from Ref [224]) with the Boson peak visible at $\approx 1\,\mathrm{THz}$, with minor deviation attributed to differences in coupling coefficients.[229,234] In contrast, for all MHPs, I instead observe clear deviations between the reduced IR and Raman spectra (see Figure 5.5(d) for $MAPbI_3$ and Figure 6.4 for other MHPs). I note that the deviations between the two types of reduced spectra cannot be attributed solely to differences in the coupling coefficients applying to Raman and IR signals. The clear differences between the broadness of the measured peaks, as well as their shape and position suggest more profound causes for the divergence between the Raman and IR responses. Overall, I thus conclude that the central Raman response in MHPs does not originate from the appearance of a Boson peak, or a 'quasi-amorphous' nature of the material.

It is evident that the Raman and IR responses are very distinct in MHPs, although they should both operate based on the same vDoS, albeit with different selection rules. I continue to explore potential reasons for the discrepancy between Raman and IR spectra, focusing in particular on the differences in the central, low-frequency Raman response. To contrast the spectra appropriately, I use the reduction schemes for Raman and IR spectra discussed above, which have been shown to be effective for amorphous,[229,235] as well as crystalline materials.[236–238] Figure 6.5 shows the reduced Raman and IR spectra for a range of metal halide semiconductors, but the spectral shapes are clearly very different. (I note that following convention, the reduction scheme here is scheme 1 and therefore different to the scheme 2 applied to data shown in Figure 6.3(c,d) in order to highlight the Boson peak.) Reduced Raman spectra shown in Figure 6.5(a) exhibit broad, almost linear, responses toward zero frequency, whereas IR absorption spectra of the same semiconductors in Figure 6.5(b) generally show well-defined phonon peaks with little signal toward zero frequency (AgI, $Cs_2AgBiBr_6$ and Cu_2AgBiI_6 do not present strongly IR-active phonons in

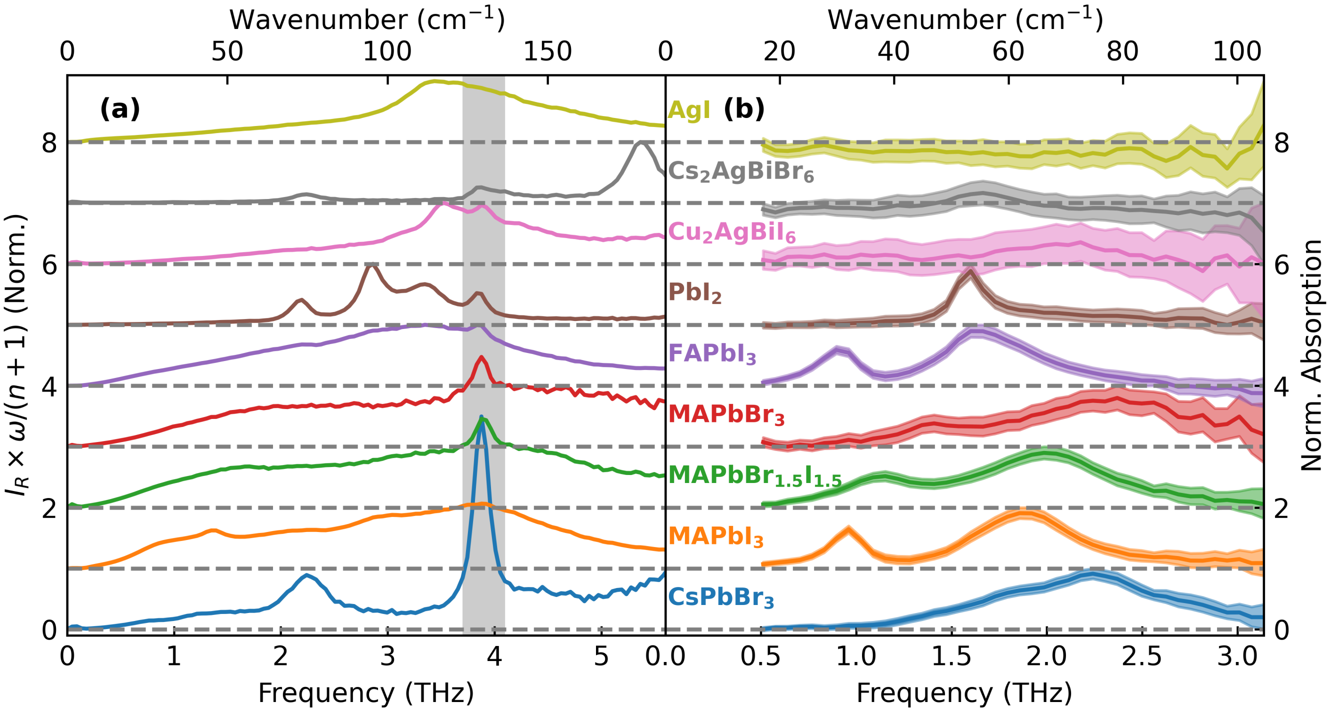

Figure 6.5: (a) Normalized reduced Raman spectra (scheme 1) of metal halides deposited as thin films on z-cut quartz. The phonon response from the quartz substrate is highlighted in gray. (b) Normalized IR absorption of the same metal halides (equivalent to the reduced Raman spectra, as can be seen from eqs 6.1 and 6.2), acquired with THz-TDS.

this range). Some of the differences in Raman and IR spectra will clearly be caused by changes in coupling coefficients for specific modes. Determination of coupling coefficients for metal-halide semiconductors are still ongoing, either thorough experimental studies, i.e. neutron scattering and heat capacity measurements, or theoretical studies.[239–241] Nevertheless, beyond such effects, it is evident from the data in Figure 6.5 that the broadening of the Raman and the IR responses differs significantly.

6.2.3 Different Broadening Mechanisms

I proceed by exploring the hypothesis that the central Raman response is caused by the broadness of the specific phonon responses observable in Raman spectra covering the ultra-low frequency region, along with the Bose–Einstein population factor which significantly amplifies Raman signals toward zero frequencies. Both for MHPs[195,199] and other materials,[242,243] Raman spectra have been approximated with a series of damped harmonic oscillators (described by the Lorentz model) multiplied by the Bose–Einstein $(n(\omega)+1)$ term, where $n(\omega) = 1/(e^{\hbar\omega/k_{\mathrm{b}}\mathrm{T}-1)}$, and $\hbar, k_{\mathrm{b,T}}$ are reduced Planck's constant, Boltzmann constant and absolute temperature, respectively. Within the above formalism (eq 6.1), this is equivalent to the assumption that the Raman coupling coefficient is linear in frequency, i.e. $C_{\mathrm{R}\propto\omega}$.[239–241] I also adopt this approach, and employ the Lorentz damped harmonic oscillator model, which predicts a scattering cross-section per oscillator mode i as

$$S_i(\omega) = A_i(n(\omega)+1) \times \mathrm{Im}(1/(\omega_1^2 - \omega^2 - i\Gamma_i\omega)) \tag{6.3}$$

where A_i, n, ω_i, and Γ_i are the amplitude, Bose–Einstein factor, harmonic oscillator frequency, and damping coefficient, respectively. I fitted the ULF Raman spectra (up to 3 THz) of MA-based MHPs, shown in Figure 6.1, to the sum of three phonon resonances with scattering cross sections described by eq 6.3, as shown in Figure C.1.[195] The above Lorentz equation, but without the $(n(\omega)+1)$ Bose–Einstein term and with two phonon resonances, was also fitted to the IR absorption spectra, also shown in Figure C.1. To quantify the extracted broadening of these phonon modes, I calculate and show the ratio Γ/ω_0 in Figure 6.6(a), which reveals that the lattice response observed in Raman spectra at ultra-low frequencies is significantly broader than that evident in IR spectra. This discrepancy may arise from the types of modes probed by the two techniques. As shown in various computational studies on lead halide perovskites, the ultra-low frequency range ($<100\,\mathrm{cm}^{-1}$) hosts a large number of IR- and Raman-active modes.[204,244–248] These have primarily been associated with different types of motions of the lead-halide sublattice, in agreement with the blueshift observed in the Raman and IR spectra for the phonon frequencies of MA-based MHPs when the bromide composition increases, as shown in Figures 6.7. Thus, the significantly enhanced broadening of the ULF Raman modes compared to the IR modes in the same range may result from different Raman- and IR-coupling rules for different types of modes.

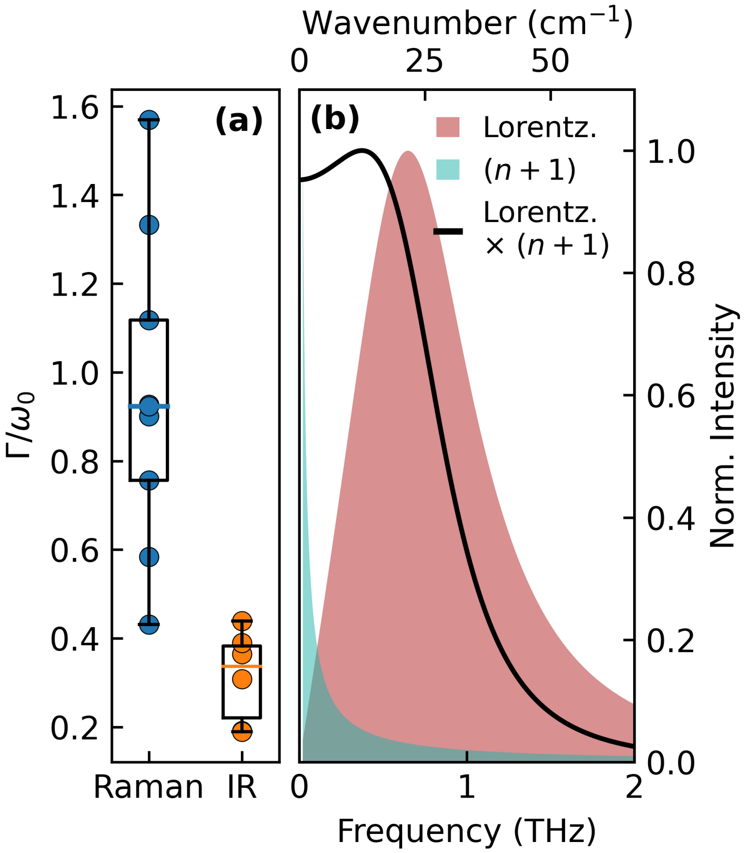

Figure 6.6: (a) Box plot showing the broadening, quantified by Γ/ω_0, of lattice vibrations in the THz-frequency range determined for MA-based metal-halide perovskites ($MAPbI_3$, $MAPbBr_{1.5}I_{1.5}$, $MAPbBr_3$) from Raman or THz-TDS IR absorption measurements, as detailed in Section 3.2 and 3.3. (b) Illustration of a damped harmonic oscillator response (Lorentz model, eq 6.3), Bose–Einstein population factor $(n(\omega)+1)$, where $n(\omega) = 1/(e^{\hbar\omega/k_{\mathrm{b}}\mathrm{T}-1)}$, and the multiplication of the two, demonstrating the expected Raman response for a single low-frequency mode according to the damped harmonic oscillator model. Parameters used were $\omega_0 = 0.8$ THz, $= 1$ THz, and $T = 300$ K.

In this context, it is important to note that while Raman can (if symmetry permits) probe both transverse optical (TO) and longitudinal optical (LO) phonons and modes,[204] THz-TDS conducted at near-normal incidence only probes transverse optical phonons since the electric field of the THz wave oscillates perpendicularly to its direction of propagation,[201] though IR measurements conducted at a significant angle can provide some access to IR-active LO phonons.[249] From a very general perspective, differences in line widths observed in Raman and IR spectra may thus arise from variations in the decay channels operating for LO and TO phonons. LO and TO phonons share some

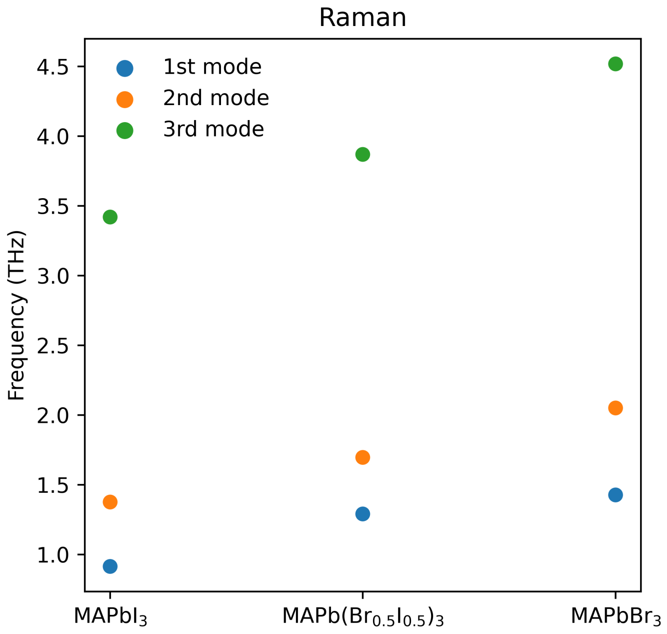

(a)

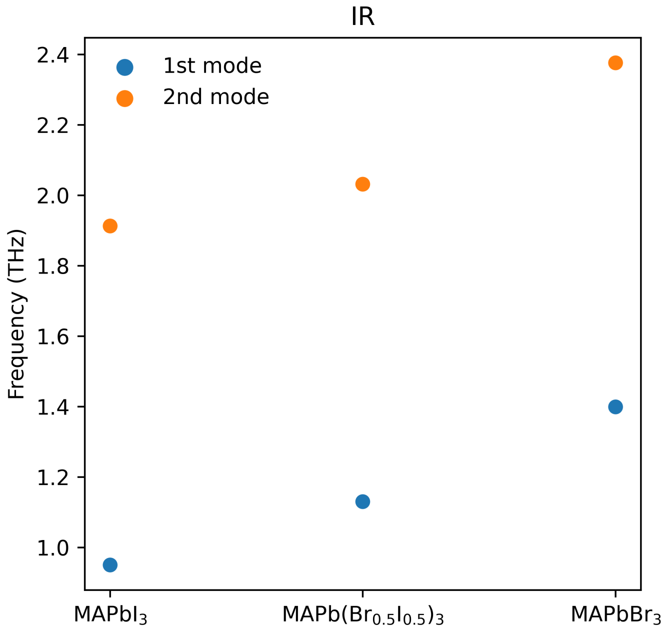

(b)

Figure 6.7: Mode frequencies extracted from fits of the damped harmonic oscillator model to the (a) Raman spectra and (b) IR spectra of $MAPbI_3$, $MAPbBr_{1.5}I_{1.5}$ and $MAPbBr_3$ thin films.

similar decay mechanisms, i.e. decay to acoustic phonons,[250] or through phonon–phonon scattering.[251] However, their decay rates will differ, since LO and TO phonons will decay into a range of different acoustic phonons.[252] LO phonons have also been reported to transform into one optical mode and one acoustic mode,[253,254] and can additionally experience Fröhlich coupling[244,255] to intrinsic charge carriers, which may shorten phonon lifetimes and thus broaden the Raman response further.

More specifically to lead-halide perovskites, accurate calculations of phonon mode frequencies have often been hindered by softness and structural flexibility of the lattice. While first-principles calculations agree that ULF modes in lead-iodide perovskites originate from Pb–I–Pb rocking and bending modes,[204,244–248] they often suffer from significant shifts in calculated peak frequencies compared to experimental data,[204,248] or do not capture[244] the experimentally observed[204,248] ultra-low frequency peaks near 10 - 20 cm^{-1}. Such discrepancies may arise from lattice anharmonicity, which has been proposed to be substantial in metal halide perovskites.[211,256–258] Moreover, the perfect cubic perovskite structure does not have any Raman-active modes,[205] but anharmonicity can cause deviation from the perfect cubic structure, and therefore lift the Raman selection rules. Indeed, Figure 6.6(a) indicates that the phonon mode broadening Γ approaches the value of its frequency ω_0 for Raman-active ULF soft modes in lead halide perovskites, a clear signature of anharmonic effects. The anharmonic low-frequency motions were investigated with molecular dynamics (MD) calculations for lead-halide perovskites that revealed lattice dynamics arising from head-to-head motion of A-cations in the cuboctahedral voids of the perovskite structure and octahedral distortions.[194] Anharmonic polar rotation motions of hybrid A-cations have also been identified.[259] Such MD simulations revealed particularly low (subpicosecond) phonon lifetimes associated with these ULF modes, that further shortened as frequencies were lowered from 3 to 1 THz.[260] While further work is needed to assign and contrast the Raman and IR intensities of soft lattice modes from such MD calculations, such information may ultimately hold the key to understanding the differences in broadening observed for ULF Raman- and IR-active modes.

Overall, I therefore posit that the central Raman response of many metal halide perovskites results from an interplay of the significant broadening of Raman-active broad soft phonon modes in the low-frequency region, amplified by the $(n+1)$ Bose–Einstein population factor, which becomes substantial at low frequencies (see Figure 6.6(b)). As a simple demonstration of these two effects, Figure 6.6(b) shows the response for a single oscillator mode according to the Lorentz model together with the Bose–Einstein population factor, along with the multiplication of the two. This should be comparable to the Raman response, with the assumption of $C_{\mathrm{R}\propto\omega}$[239–241] within the formalism in eq 6.1. The resulting function represented by the black line is clearly very comparable in shape to the central Raman response experimentally observed. In particular, I note that this simulated spectrum accurately reflects the peculiarity of ULF Raman spectra of lead-halide perovskites, i.e., the presence of both peak-like features and a seemingly continuous background heading to large amplitude toward lower frequencies. The broad central Raman response toward zero scattering frequencies is thus the result of the particularly low-energy lattice vibrations in these materials, which tail into the frequency-range where the population factor becomes significant. As such, it therefore does not reflect a continuum of vibrational frequencies, but rather the presence of individually defined but very broad modes. I also note that such broad low-frequency Raman response of MHPs has been shown to increase with temperature,[194,203,219] agreeing well with my hypothesis. On the other hand, the IR response does not show such low-frequency response because of two combined effects: first, IR measurements are light absorption measurements, in which one IR photon is converted into a phonon, so do not depend on the initial population of vibrational modes. In contrast, Raman scattering requires interaction with an existing ground- or higher state phonon population, and therefore the Bose–Einstein population factor becomes prominent in Raman scattering. Second, the IR-active TO phonon modes exhibit far narrower line widths stemming from different decay mechanisms compared to those operating for the lowest-frequency, most anharmonic Raman-active modes. I thus conclude that the central Raman response results from the presence of significantly broadened low-energy Raman-active lattice modes whose anharmonic response is amplified by the Bose–Einstein population factor, and that the existence of these modes is the criterion for such central Raman response.

6.3 Conclusion

In conclusion, I examined the lattice responses in the low-frequency THz regime across a range of metal halide semiconductors, contrasting Raman- and IR-active vibrations. I employed ultra-low frequency Raman and THz-TDS IR spectroscopy, observing clear discrepancies in the spectra obtained. While Raman spectra exhibit a broad central response rising toward zero frequency, no such response is visible in the IR spectra, which only display well-defined resonance peaks. I systematically examined the cause behind the central Raman response, and the observed discrepancies between Raman and IR spectra. I excluded the following possibilities as the primary causes of the central Raman response: a Boson peak arising from a proposed ‘liquid-like’ nature of these materials, dynamic disorder originating from A-cations, lone pairs, or octahedral tilting, and static disorder associated with extrinsic defects. Instead, I attribute the central Raman peak to a combination of particularly strongly broadened low-energy Raman-active modes whose response thus tails into the range where the Bose–Einstein factor governing phonon population becomes very significant. The IR response of these metal halide semiconductors, on the other hand, does not show an equivalent feature near zero frequencies because the line widths of the TO phonons governing IR absorption is narrower, and the Bose–Einstein population factor does not contribute. Overall, my findings reveal the complexities of light-matter interactions in soft metal-halide semiconductors governed by significant low-energy lattice dynamics. Understanding such lattice dynamics in soft semiconductors will help discover and engineer next-generation novel materials for photovoltaic applications.

7

Conclusion and Outlook

This thesis has focused on understanding the photophysics and structural dynamics of metal-halide perovskites for solar photovoltaic applications. The fundamentals of semiconductor physics through a tight-binding model, and those of vibrational physics through monatomic and diatomic chains were presented in Chapter 2, as well as a background overview and literature review of MHPs and their photophysics. The work presented in this thesis utilised various spectroscopic techniques, including absorption spectroscopy, photoluminescence, X-ray diffraction, terahertz spectroscopy, and ultra-low frequency Raman, which were introduced and discussed in Chapter 3.

In Chapter 4, I investigated halide anion migration under illumination, using in-situ XRD and PL techniques. It focused on the effects of a hole-transport layer (HTL) and an ionic additive passivation agent on halide segregation. This chapter showed that when there is a HTL present, PL and XRD point to seemingly contrasting conclusions: PL changes more for MHP with a HTL, suggesting more halide segregation occurs with a HTL, but XRD changes more for MHP without a HTL, suggesting the opposite. I explain this apparent discrepancy with a model where holes are first swept into the HTL, before preferentially back-transferring into iodide-rich regions near the MHP/HTL interface. Further, the slowing down of halide segregation with the introduction of a HTL was due to the depletion of holes into the HTL. This result shows that the use of PL alone may be misleading when investigating halide segregation, especially when there is a charge-transport layer (CTL) present. It is therefore recommended to employ a structural measurement, for example XRD, in addition to PL, when investigating halide segregation. Additionally, I investigated the effects of an ionic additive on halide segregation, identified potential defects the ionic additive may be passivating, and concluded that the specific nature of traps determines their role in halide segregation. The work presented in this chapter highlights the importance of selective passivation techniques on halide segregation.

Chapter 5 focused on different degradation mechanisms of tin-only and mixed lead-tin iodide perovskites in ambient air. I confirmed that both of these perovskites undergo severe optoelectronic and structural degradation during ambient air exposure; however the specific pathways and fundamental mechanisms differ. For both of the perovskites, the monomolecular decay rate increased with air-exposure time, but the sum charge-carrier mobility decreased much more slowly for mixed lead-tin perovskite. Through absorption measurements, I also determined that Burstein-Moss effects and a decrease of the exciton binding energy were present in tin-only perovskite under ambient air exposure, but these were not significant for mixed lead-tin perovskites. These results indicate that tin-only perovskites degrade via p-doping and that mixed lead-tin perovskites do not undergo doping during degradation. To confirm, I performed THz-TDS measurements to quantify the background doping density, which agreed with earlier results from absorption measurements. Therefore, I concluded that tin-only perovskites degrade through the formation of shallow defect states which contributes to doping of the valence band, whereas mixed lead-tin perovskites degrade through the formation of deep trap states, which do not dope the bulk semiconductor significantly. I was further able to identify potential degradation products through XRD. This chapter highlights the difference in degradation mechanisms between tin-only and mixed lead-tin perovskites, and I suggest that more specific passivation technique would be useful for mixed lead-tin perovskite in order to further improve their stability and photovoltaic device performances.

In Chapter 6, I studied the low-frequency vibrational properties of various metal halides, including MHP, using THz and ultra-low-frequency Raman spectroscopies. MHPs have been reported to have an intriguing response in the low-frequency region in Raman spectra, where the response is very broad. However, this broad response is not visible in IR spectra, where there are well-defined peaks from phonons. The exact mechanism and origin of this central Raman peak is still under debate in the literature, and especially the discrepancy between Raman and IR responses has not been resolved. There have been a number of hypotheses explaining the central Raman peak. In this chapter, I systematically discussed and assessed these hypotheses, through Raman and IR measurements of various metal-halide semiconductors, as well as data available from the literature. I was able to rule out the following hypotheses: extrinsic defects, octahedral tilting, cation lone pairs, and ‘liquid-like’ Boson peaks. Instead, I suggested an alternate explanation for such central Raman peak, and a reconciliation with IR spectra, through appropriate reduction procedures. I proposed that the central Raman response is a result of an interplay of broad Raman-active, low-frequency vibrational modes with Bose-Einstein population factor. However, IR-active vibrational modes have narrower broadening due to differing broadening mechanisms from Raman-active counterparts, and the Bose-Einstein population factor does not apply to IR spectra. This chapter elucidates the complexities involved with low-frequency lattice vibrations, which is particularly of importance for emerging soft metal-halide semiconductors for photovoltaics.

Overall, the work presented in this thesis focused on the fundamental aspect of photophysics and structural dynamics of metal-halide perovskites. I have showcased that investigation of these materials requires careful consideration of the choice of techniques as well as appropriate data analysis, for future research. I have also addressed more specific questions in the research field, namely: the effects of a hole-transport layer and passivation on halide segregation, the differences in degradation mechanisms between tin-only and mixed lead-tin perovskites in ambient air, and the origins of low-frequency Raman responses in metal-halide perovskites. Further research should be directed into understanding the full mechanisms of halide segregation, potentially with structural as well as optical techniques. Novel methods to further impede self p-doping of tin-based MHPs need to be developed before successful commercialisation. Additionally, the anharmonicity of MHPs need to be further investigated in order to fully understand the properties of MHPs.

Appendices

A

Supplementary Analysis for Chapter 4

Contents

A.1 Sample fabrication

Samples used in this study were fabricated by R. D. J. Oliver.

$FA_{0.83}Cs_{0.17}Pb(Br_{0.4}I_{0.6})_3$ metal-halide perovskite (MHP) thin-film samples were fabricated in line with a previous report,[121] with slight modification to account for the different substrate area. In summary, the precursors salts (formamidinium iodide, FAI, GreatCell Solar; cesium iodide, CsI, 99.99 %, Alfa-Aesar; lead iodide, PbI_2, 99.9 %, TCI; lead bromide, $PbBr_2$, >98 %, Alfa-Aesar) were weighed stoichiometrically in an N_2 filled glovebox. The precursor salts were dissolved in a 4:1 ratio by volume of N,N-dimethylformamide (DMF, Sigma Aldrich) to dimethyl sulfoxide (DMSO, Sigma Aldrich), to a concentration of 1.3 mol. The solution was stirred overnight before deposition. The ionic additive 1-butyl-1-methylpiperidinium tetrafluoroborate ($[BMP]^+[BF_4]^-$, purity 99 %), purchased from Sigma Aldrich, was dissolved in a 4:1 volume ratio of dimethylformamide (DMF) and dimethylsulfoxide (DMSO) and shaken overnight at room temperature. To mix the ionic additive into the precursor solution, an appropriate volume of the ionic additive solution was added to the perovskite precursor solution to obtain a perovskite concentration of 1.3 mol for the precursor and 0.5 mg mL^{-1} of the ionic additive. Substrates made of z-cut quartz (area 1.3 cm^2) were cleaned by subsequent sonication in Decon90 (1 vol% in deionised water), deionised water, acetone (Sigma Aldrich) and isopropanol (Sigma Aldrich) for 10 min each. The substrates were then dried using an N_2 gun before being treated with a UV-O_3 plasma for 12 min. The substrates were then immediately transferred into an N_2 filled glovebox prior to deposition of the perovskite layer. The perovskite films were fabricated using the following spincoating recipe: 50 µL of precursor solution was deposited dynamically onto the quartz substrate spinning at 1000 rpm. After 5 s, the substrate accelerated at 800 $rpms^{-1}$, until it reached a final spin speed of 5000 rpm where it remained for 30 s. An antisolvent quench using 50 μL of Anisole (Sigma Aldrich) was performed 5s before the end of this step. The films were then annealed at 100 °C for 30 min. PMMA (poly(methyl methacrylate), Sigma Aldrich, mean molar weight

A.2 Further XRD/PL Data

Further XRD/PL data are presented; XRD/PL measurements on samples without any capping layer are presented in Figure A.1, and those on samples with additive with PMMA or PTAA coating are presented in Figure A.2.

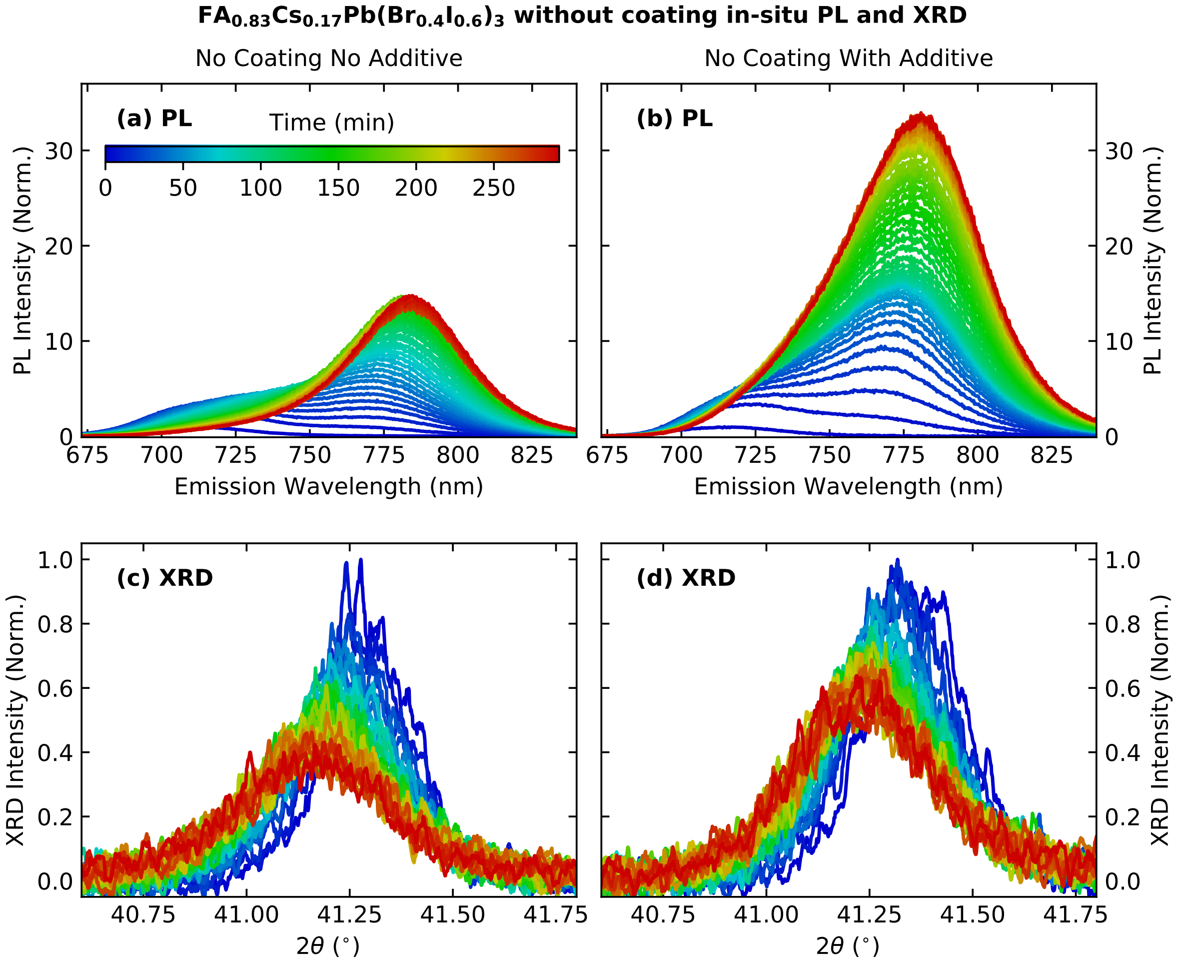

Figure A.1: Evolution under illumination (470 nm continuous wave (CW) illumination with 190 mW cm^{-2} intensity for ≈ 5 hours) of the PL spectra (top) and the second-order XRD peak recorded in-situ for uncoated $FA_{0.83}Cs_{0.17}Pb(Br_{0.4}I_{0.6})_3$ thin films without (left) and with (right) piperidinium ionic salt having been added during perovskite fabrication.

A.3 XRD Angle Change

Knight et al. recently examined the evolution of the XRD pattern to show that PMMA-coated methylammonium (MA)-based MHPs segregate differently to FACs-based MHPs.[57] The XRD peak of $MAPb(Br_{0.5}I_{0.5})_3$ MHP decreased in amplitude as it underwent halide segregation, keeping the same central peak position. On the other hand, the XRD peak of $FA_{0.83}Cs_{0.17}Pb(Br_{0.4}I_{0.6})_3$ MHP, the same composition as investigated in this study, also decreased in amplitude during halide segregation, but the XRD peak shifted to lower angles while widening. The MA-based MHP also exhibited a growth in the

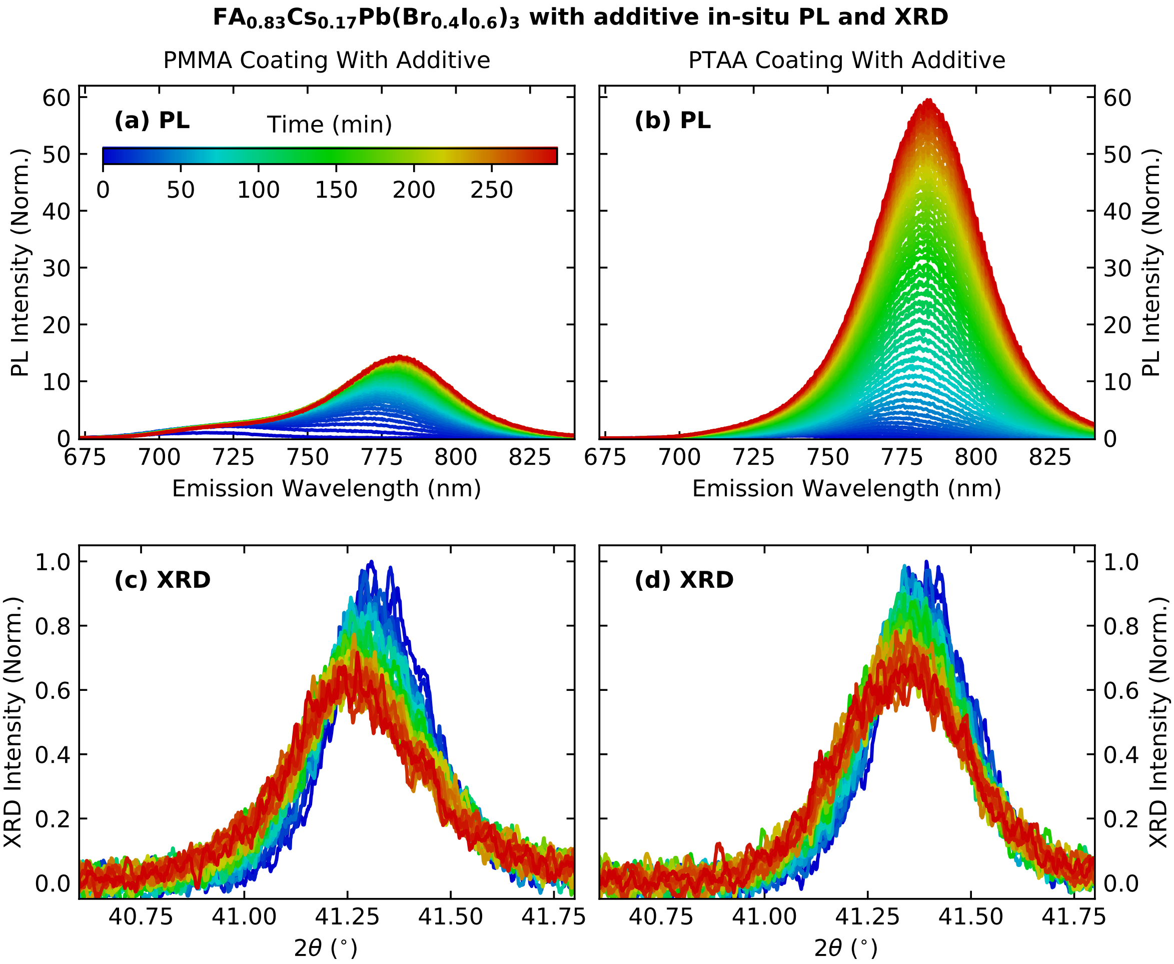

Figure A.2: Evolution under illumination (470 nm continuous wave (CW) illumination with 190 mW cm^{-2} intensity for $\approx$ 5 hours) of the PL spectra (top) and the second-order XRD peak recorded in-situ for $FA_{0.83}Cs_{0.17}Pb(Br_{0.4}I_{0.6})_3$ thin films with PMMA (left) and PTAA (right) coating with piperidinium ionic salt having been added during perovskite fabrication.

tail regions of the XRD peak, further away from the central peak position. This was attributed to boundary-mediated halide segregation evolution, which does not affect the bulk of the MHP and therefore keeps the central peak position constant. In contrast to the lack of angle change in MA-based MHP, a bulk-mediated halide segregation in the FACs-based MHP affects the full volume of the material, causing a structural change throughout the MHP, shifting the XRD peak angle.

As can be seen from Figure 4.2(d) in the main text, the PTAA-coated MHP without piperidinium additive does not show much, if any, angle change during the $\approx$ 5-hour illumination process. This lack of angle change is in contrast with the rest of the sample

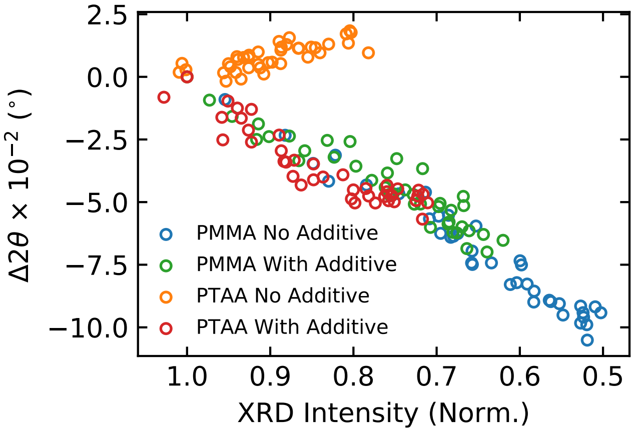

Figure A.3: The change in 2θ XRD angle, plotted against the peak amplitude of the (220) XRD peak for all four sample combinations under consideration, $FA_{0.83}Cs_{0.17}Pb(Br_{0.4}I_{0.6})_3$ thin films fabricated with or without piperidinium ionic additive and with either PTAA or PMMA top coating, recorded over the $\approx$ 5-hour illumination period.

set, whose (220) XRD 2θ all decreased with halide segregation, and this decrease in angle is consistent with previous observations.[57] Interestingly, this difference implies that upon the addition of piperidinium additive to a PTAA-coated MHP, its halide segregation behavior became comparable to that of PMMA-coated MHPs.

The 2θ XRD angle change is plotted in Figure A.3 against the normalised XRD peak intensity of the (220) XRD peak for all sample combinations during the $\approx$ 5-hour illumination, clearly revealing different types of halide segregation behavior. The 2θ XRD angle and the XRD intensity were extracted through fits of a Gaussian function to each XRD pattern. The PTAA-coated MHP without piperidinium ionic additive shows a very constant 2θ XRD angle over illumination time, or even a very minor angle increase if there is any, and this is very similar to the boundary-mediated segregation dynamics observed in the methylammonium-based MHP by Knight *et al.*[57] This observation further corroborates the halide segregation dynamics in the PTAA-coated $FA_{0.83}Cs_{0.17}Pb(Br_{0.4}I_{0.6})_3$ film without piperidinium ionic additive occur only at the MHP-PTAA boundary. The other three samples, $FA_{0.83}Cs_{0.17}Pb(Br_{0.4}I_{0.6})_3$ with piperidinium ionic additive and

PTAA coating, and both films with PMMA coating, qualitatively follow the same behavior (Figure A.3). This similarity shows that a PTAA-coated MHP changes its halide segregation behavior to that of PMMA films upon the addition of piperidinium ionic additive, exhibiting a bulk-mediated halide segregation behavior. When piperidinium salt is added to $FA_{0.83}Cs_{0.17}Pb(Br_{0.4}I_{0.6})_3$ with PTAA coating, the trap states at the PTAA MHP interface are passivated.[121] Although there is still expected to be some charge-carrier accumulation at the interface owing to Coulombic interaction, the lack of such interfacial trap states leads to a higher total charge-carrier population, on average and across the bulk, thereby causing halide segregation in the bulk as well.

A.4 PLQY Measurements

PLQY measurements were performed by R. D. J. Oliver.

Photoluminescence quantum yield (PLQY) measurements were performed following the procedure reported previously.[261] In brief, the samples were placed in an integrating sphere and photoexcited by a 532 nm continuous wave laser. The photoluminescence was coupled into a fibre and collected by a QEPro spectrometer. The integrating sphere and fibre were calibrated using a lamp of known spectrum. The illumination intensity was $30\,\mathrm{mW\,cm^{-2}}$ which corresponds to approximately 0.5 suns equivalent absorbed photon flux[262] at a bandgap of 1.6 eV, therefore the PLQY values presented here are underestimates of their value at one-sun equivalent conditions.

Sample Composition	Coating Layer	Ionic Additive	PLQY (%)
$FA_{0.83}Cs_{0.17}Pb(Br_{0.4}I_{0.6})_3$	Uncoated	No	0.221 †
$FA_{0.83}Cs_{0.17}Pb(Br_{0.4}I_{0.6})_3$	Uncoated	Yes	0.579 †
$FA_{0.83}Cs_{0.17}Pb(Br_{0.4}I_{0.6})_3$	PTAA	No	3.84×10^{-3} †
$FA_{0.83}Cs_{0.17}Pb(Br_{0.4}I_{0.6})_3$	PTAA	Yes	4.59×10^{-2} †
$FA_{0.83}Cs_{0.17}Pb(Br_{0.1}I_{0.9})_3$	Uncoated	No	1.87
$FA_{0.83}Cs_{0.17}Pb(Br_{0.1}I_{0.9})_3$	Uncoated	Yes	2.48
$FA_{0.83}Cs_{0.17}Pb(Br_{0.1}I_{0.9})_3$	PTAA	No	0.17
$FA_{0.83}Cs_{0.17}Pb(Br_{0.1}I_{0.9})_3$	PTAA	Yes	0.89

Table A.1: PLQY measurements of uncoated and PTAA-coated $FA_{0.83}Cs_{0.17}Pb(Br_{0.4}I_{0.6})_3$ and $FA_{0.83}Cs_{0.17}Pb(Br_{0.1}I_{0.9})_3$ thin films with and without piperidinium ionic additive. (†) The PLQY data for $FA_{0.83}Cs_{0.17}Pb(Br_{0.4}I_{0.6})_3$ was taken from Oliver *et al.*[122]

B

Supplementary Analysis for Chapter 5

Contents

B.1 Sample fabrication

Samples used in this study were fabricated by C. Kamaraki.

Materials

Lead (II) iodide (PbI_2, ultra-dry, 99.999% mesh beads), tin (II) iodide (SnI_2, ultra-dry, 99.999% mesh beads), were purchased from Alfa Aesar. Cesium iodide (CsI, 99.9%), N,N-dimethylformamide (DMF, anhydrous), dimethyl sulfoxide (DMSO, anhydrous) and anisole (anhydrous) were sourced from Sigma Aldrich. Tin (II) fluoride (SnF_2, 99%) was purchased from Thermo Scientific Acros, while methylammonium iodide (MAI) and formamidinium Iodide (FAI) were sourced from Greatcell Solar. Solution preparation and sample fabrication processes were adapted from Klug et al.[263] and the details can be found below.

Solution Preparation

Three precursor solutions of $FA_{0.75}Cs_{0.25}SnI_3$, $FA_{0.75}Cs_{0.25}Pb_{0.5}Sn_{0.5}I_3$ and $FA_{0.6}MA_{0.4}Pb_{0.5}Sn_{0.5}I_3$ were prepared the day before thin-film deposition. In addition to the main precursor materials, 10 % molar excess of tin fluoride was added in all precursor solutions with respect to each of their tin content. A mixed solvent system of DMF:DMSO of 4:1 volumetric ratio was used to dissolve the precursor materials for all three solutions. A solution of 1.2 M of $FA_{0.75}Cs_{0.25}SnI_3$ was prepared by dissolving 1341.07 mg of SnI_2, 464.31 mg of FAI, 233.82 mg of CsI and 56.4 mg of SnF_2 in 3 mL DMF:DMSO. A 1.2 M solution of $FA_{0.75}Cs_{0.25}Pb_{0.5}Sn_{0.5}I_3$ was prepared by dissolving 670.53 mg of SnI_2, 829.81 mg of PbI_2, 464.31 mg of FAI, 233.82 mg of CsI and 28.2 mg of SnF_2 in 3 mL of mixed DMF:DMSO. A 1.2 M of $FA_{0.6}MA_{0.4}Pb_{0.5}Sn_{0.5}I_3$ was prepared by dissolving 670.53 mg of SnI_2, 829.81 mg of PbI_2, 371.45 mg of FAI, 228.91 mg of MAI and 28.2 mg of SnF_2 in 3 mL of DMF:DMSO. Prior to spin coating, the perovskite solutions were filtered with a 0.2 µm PTFE syringe filter.

Sample Fabrication

z-cut quartz disks (2 mm thick, 13 mm diameter) were used as substrates, which were cleaned with sequential sonication in acetone and isopropanol and treated with O_2-plasma for 5 min just before processing. Then, substrates were transferred to a nitrogen-filled glovebox, where the perovskite deposition took place. A one-step deposition method with antisolvent-quenching (anisole) was employed. 50 µL of each solution was dropped onto the substrate and spun statically with 4500 rpm with a 6 s ramp for 14 s. 100 µL of anisole was dispensed on the substrate 13 s after spinning begun. Right after the spin-coating program finished, N_2 gas flow was applied to the substrate for 10 s, during which the film darkened. The annealing step followed, for which the substrates were transferred onto a hotplate for 10 min. $FA_{0.75}Cs_{0.25}SnI_3$ and $FA_{0.75}Cs_{0.25}Pb_{0.5}Sn_{0.5}I_3$ were annealed at 120 °C, while $FA_{0.6}MA_{0.4}Pb_{0.5}Sn_{0.5}I_3$ was cured at 100 °C. After annealing, all samples were stored in a nitrogen-filled glovebox.

B.2 Background Doping Density Determination

I estimated the background hole doping density in the tin-only MHP using the evolution of dark conductivity spectrum and the charge-carrier mobility from Figure 5.7 and 5.1 respectively. It was assumed that the hole mobility is the same as the electron mobility from similar effective masses of electrons and holes,[264,265] so I used $\mu_h = \mu_{sum}/2$. I also employed the relation $\sigma = ep_0\mu_h$, where e is the elementary charge, and p_0 the background hole density. The dark conductivity contribution from the background holes was estimated by averaging the dark conductivity in the low frequency region $(0.4 - 0.7\,\mathrm{THz})$, where the phonon contribution from optical modes is insignificant. The detection limit of the background doping density was estimated from the signal to noise level of my measurement and the relation $\sigma = ep_0\mu_h$, obtaining $p_0^{lim} \approx 10^{18}\,\mathrm{cm}^{-3}$ as my detection limit.

B.3 Discussion on Vacancy-Ordered Double Perovskite

In agreement with previous reports,[145,163,164] I suggest that vacancy-ordered double perovskite is a possible degradation product of tin-only $FA_{0.75}Cs_{0.25}SnI_3$ in ambient air, based on the dark conductivity measurement shown in Figure 5.7 and XRD measurement shown in Figure 5.8 of Chapter 5. The phonon peaks evident in the dark conductivity measurements at prolonged degradation times for $FA_{0.75}Cs_{0.25}SnI_3$ agree closely with those of previously reported transverse optical phonon modes of Cs_2SnI_6.[165] The corresponding phonon modes of $(FA_{0.75}Cs_{0.25})_2SnI_6$ or FA_2SnI_6 have not been reported in the literature so far. The lowest frequency transverse optical modes that we observe have been identified previously to be a lattice vibration involving the A-cation, which would imply that the frequency is expected to vary with different A-cation composition; from the difference in mass between FA^+ and Cs^+ it would be expected a notable difference in phonon mode frequencies, which however appears absent here. I suggest that the Cs^+ submode could possess a higher cross section for interaction with respect to the THz excitation compared to FA^+, however, modelling of THz interactions with such modes in real-world structures would require calculations beyond the scope of this study.

The XRD patterns presented in Figure 5.8 of Chapter 5 provide further evidence to the formation of such vacancy-ordered double perovskite. An appearance of the broad XRD peak at a higher angle is attributed to this degradation product. The lattice parameter of the vacancy-ordered double perovskite is expected to be lower than for the pristine $FA_{0.75}Cs_{0.25}SnI_3$, since the 4+ oxidation state of tin would lead to an enhanced Coulomb attraction with the rest of the structure.[166] It would therefore also be expected that there is a mismatch in lattice parameters between the MHP and double perovskite domains, causing strains, in accordance with the broad peaks that is observed. This broadening, however, may also arise from the presence of very small crystalline domains of the vacancy-ordered double perovskites.

C

Supplementary Analysis for Chapter 6

Contents

C.1 Sample fabrication

$MAPbI_3$, $MAPbBr_{1.5}I_{1.5}$ and $MAPbBr_3$ thin films

$MAPbI_3$, $MAPbBr_{1.5}I_{1.5}$ and $MAPbBr_3$ thin films were fabricated by J. B. Patel and S. Yan.

$MAPbI_3$, $MAPbBr_{1.5}I_{1.5}$ and $MAPbBr_3$ thin films were prepared using the acetonitrile route as reported previously.[52,266] In brief, MAI (Greatcell), MABr (Greatcell), PbI_2 (TCI Chemicals 99.99%) and $PbBr_2$ (Thermo Scientific 98%) were weighed out and dissolved in a methylamine/acetonitrile (Merck Chemicals) solvent system to give a 0.5 M perovskite solution as described by Noel et al.[266] The solutions were then statically spincoated onto quartz substrates in a nitrogen filled drybox at 2000 rpm for 45 s. The films were then annealed for 90 minutes at 100 °C.

$MAPbI_3$ single crystals

$MAPbI_3$ single crystals were fabricated by J. Peng.

The $MAPbI_3$ perovskite single crystals were fabricated via inverse temperature crystallization.[267,268] Typically, 1.3 M $CH_3NH_3PbI_3$ precursors were prepared by adding 2.3 g PbI_2 and 0.8 g MAI into 3.85 mL γ–butyrolactone, heated at 90 °C for 2 hours with stirring. Then, the precursor solutions were filtered with syringe filters (0.22 µm pore size) and transferred to clean containers, which were kept on a stable hot-plate and heated at 130 °C for 3 hours. Crystals were formed on the bottom of the containers. Finally, the crystals were collected and dried at 60 °C in glovebox for 2 hours.

$FAPbI_3$ thin films

$FAPbI_3$ thin films were fabricated by S. Yan.

FAI and PbI_2 were co-evaporated with the molar ratio of FAI:PbI_2=1:1 on the z-cut quartz substrate in a custom-built thermal evaporator chamber. During the evaporation, the pressure was typically $< 5 \times 10^{-6}$ mbar. The sublimation rate of the precursors was controlled using gold-plated quartz microbalances adjacent to the crucible and a PID-loop-control software. Unless specified otherwise, all samples were annealed in an N_2 glovebox at 150 °C for 5 minutes and at 135 °C for 25 minutes. After cooling down to room temperature, films were ready to use.

$CsPbBr_3$ thin films

$CsPbBr_3$ thin films were fabricated by Y. Kominko.

A Bridgman-grown single crystal of $CsPbBr_3$ was gently ground into a fine powder in a nitrogen-filled glove box. The starting material was placed in a thermal evaporator crucible. Quartz substrates were ultrasonically cleaned in Hellmanex III (2% in water), deionized water, acetone, and isopropanol for 15 min at each stage, followed by UV ozone treatment for 10 min. The thickness of the fabricated films was controllable by the mass of the deposition material (200 mg of starting material to obtain 100 nm perovskite film). The vacuum of the evaporation chamber was reduced to 10^{-6} Torr. The substrate temperature was typically 20 °C. The deposition temperature was in the range 400-500 °C. The deposition rate was 0.6 $\text{Å}\,\text{s}^{-1}$. The substrate rotation velocity was 10 rpm. After the evaporation, the films were aged at room temperature in a nitrogen-filled glove box for one month.

$CsPbBr_3$ single crystals

$CsPbBr_3$ single crystals were fabricated by K. M. McCall.

Synthesis and Purification Runs

6.423 g of CsBr (ChemCraft, 99.999%) and 11.077 g of $PbBr_2$ (Sigma Aldrich, 99.999%) were mixed and ground together thoroughly using a mortar in an Ar glovebox. This material was then flame-sealed under 1.4×10^{-2} mbar vacuum into a fused silica ampule with a sharp tip. This ampule was placed in the hot zone of a custom-built 3-zone Bridgman furnace (HTM Reetz), and the temperatures were set to 675 °C, 400 °C, and 400 °C. The sample was left overnight, then moved through the furnace at a speed of 0.081 mm/min while undergoing 0.3 rpm rotation. The resulting ingot had black impurities near the top, so the sample was reset and the same temperature profile applied, and moved through the furnace more slowly (0.042 mm/min, 2.52 mm/hr) to fully segregate these impurities. The resulting ingot was opened in the Ar glovebox and the black regions at the top of the ingot were cut off and discarded, and the material was broken into chunks and flame-sealed under 1.1×10^{-2} mbar vacuum into a new fused silica ampule with a sharp tip. A final purification run, with identical conditions to the previous run (0.042 mm/min, 0.3 rpm, temperatures of 675 °C - 400 °C - 400 °C).

Bridgman Crystal Growth

The Vertical Bridgman method was used to grow the large single crystals of $CsPbBr_3$. The ampule was reset to the hot zone for the Bridgman Growth. The zone 1 temperature was set to 650 °C with a 150 °C/hr ramp rate, and held for 12 hours to ensure a full melt before sample motion occurred. The zone 2 and 3 temperatures were set to 375 °C and held for 350 hours while the ampule was moved through the furnace at a rate of 0.015 mm/min (0.9 mm/hr) under 0.3 rpm rotation. After the motion had ceased, the zone 1 temperature ramped to 375 °C. The cooling program was set to slow during the phase transitions occurring near 120 and 90 °C, with a 10 °C/hr cooling rate from 375 °C to 175 °C, a 2.5 °C/hr slow cooling rate from 175 °C to 75 °C, and a 10 °C/hr rate to 30 °C.

Crystal Processing

The ingot was opened in an Ar glovebox and cut into 2 mm-thick wafers using a Crystal Systems Corporation Cu-02 Desktop Crystal Cutter with Goniometer operating at 60 rpm. The surfaces of these wafers were polished using a Crystal Systems Corporation TP-02 Polisher operating at 20 rpm, with MicroMesh SiC cutting papers used to get successively finer surfaces with a final polish of 12000 grit.

PbI_2 thin films

PbI_2 thin films were fabricated by S. Yan.

PbI_2 was evaporated with the deposition rate of $0.2\,\text{Å}\,\text{s}^{-1}$ on the z-cut quartz substrate in a custom-built thermal evaporator chamber. During the evaporation, the pressure was typically $< 5 \times 10^{-6}$ mbar. The source rates were kept constant using gold-plated quartz microbalances and a PID-loop-control software.

$Cs_2AgBiBr_6$ thin films

$Cs_2AgBiBr_6$ thin films were fabricated by M. T. Sirtl.

The stock solution was prepared by dissolving CsBr (Alpha Aesar, 99.999% metals basis), $BiBr_3$ (Alpha Aesar, 99.9% metals basis) and AgBr (Alpha Aesar, 99.998% metals basis) in 1 mL DMSO (Sigma Aldrich, anhydrous, ≥99.9%) by vigorous stirring at 130 °C for 60 minutes to obtain a 0.5 M solution. All steps were performed in a nitrogen-filled glovebox with controlled atmosphere. The substrates were cleaned with a detergent (Hellmanex), followed by washing with acetone and ethanol and dried under an air stream. Afterwards, the substrates were cleaned with oxygen plasma for 5 minutes and immediately transferred into the glovebox. Prior to the spincoating step, the substrates and the solution were placed on a hotplate (Heidolph with internal temperature sensor) at 60 °C to be preheated. The stock solution was constantly stirred. The thin films were fabricated by spincoating the warm solution dynamically (1000 rpm for 10 s, followed by a second step at 6000 rpm for 35 seconds) onto the preheated substrates (70 µL of the solution were dropped immediately after the substrate started to spin at 1000 rpm). After the spincoating, the thin films were annealed at 275 °C for 5 minutes, and the preheating was set at 60 °C.

Cu_2AgBiI_6 thin films

Cu_2AgBiI_6 thin films were fabricated by B. Putland.

Thin films of Cu_2AgBiI_6 were fabricated by vacuum evaporating (BOC Edwards Auto 306) and co-depositing bismuth(III) iodide (Alpha Aesar Puratronic, 99.999%), silver(I) iodide (Alpha Aesar Premion, 99.999%), and copper(I) iodide (Alpha Aesar Puratronic, 99.998%) precursors from three separate, $2.4\,\mathrm{cm}^3$ alumina crucibles and thermal sources. The crucibles and sources were custom-made by Moorfield Nanotechnology. The precursors were heated to the temperature corresponding to the following evaporation rates: CuI, AgI, $BiI_3 = 0.33\,\text{Å}\,\mathrm{s}^{-1}$ (370 °C), $0.18\,\text{Å}\,\mathrm{s}^{-1}$ (475 °C), and $0.50\,\text{Å}\,\mathrm{s}^{-1}$ (230 °C), respectively.

Cu_2AgBiI_6 films were 250 nm thick, as measured by a Veeko Dektak 150 profilometer. The rates were measured using three quartz crystal microbalances (QCM) positioned off centre to each sources' vapour cone and an Inficon SQC-310 deposition controller. All depositions were carried out under vacuum ($\approx 2 \times 10^{-6}$ mbar). The substrates were protected during the heating and cooling process by a mechanical shutter, and the substrates were rotated during deposition. No intentional substrate heating was applied, but the substrates reached a maximum temperature of approximately 60 °C during co-deposition due to heat transfer from the sources.

AgI thin films

AgI thin films were fabricated by B. Putland.

Thin films of silver iodide were fabricated by depositing (using a BOC Edwards Auto 306 evaporator) silver(I) iodide (Alpha Aesar Premion, 99.999%) precursor from 2.4 cm^3 alumina crucibles and thermal sources. The crucibles and sources were custom-made by Moorfield Nanotechnology. The precursor was heated to the temperature corresponding to the desired evaporation rates, with the rates measured using a quartz crystal microbalance positioned off centre to the source's vapour cone and an Inficon SQC-310 deposition controller. All depositions were carried out under vacuum (10^{-6} mbar). The substrates were protected during the heating and cooling process by a mechanical shutter, and the substrates were rotated during deposition. Films were annealed post deposition in a nitrogen glovebox for 15 minutes at 180 °C. The evaporation rate was 0.2 Å s^{-1}.

C.2 Fitting of Raman and THz IR Spectra

Figure C.1 shows the fitting done for Raman and IR spectra for MA-based MHPs. For the Raman spectra, three phonons and a quasi-elastic scattering contribution[195] were fit, and for the IR spectra two phonons were fit.

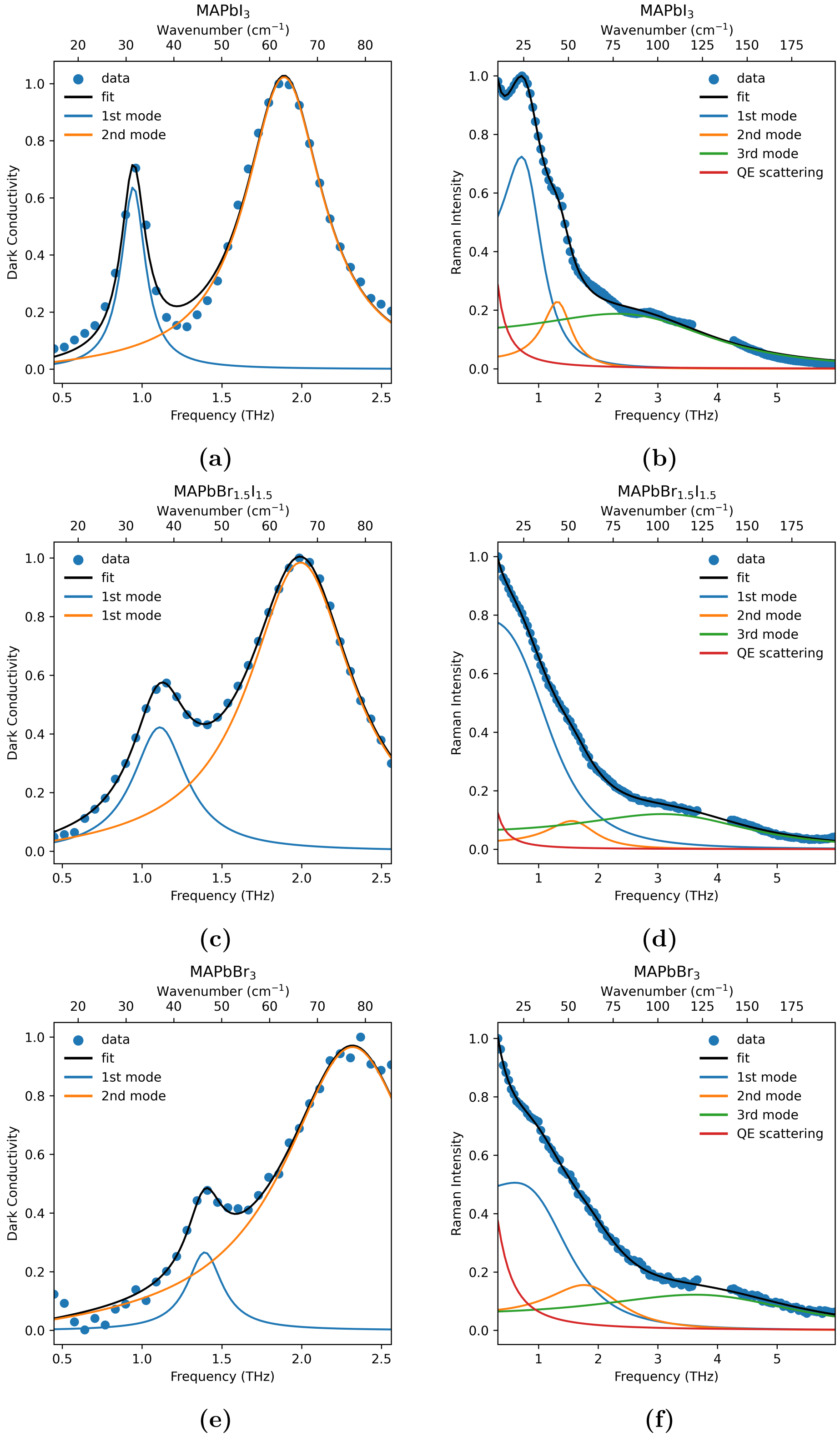

(a) (b) (c) (d) (e) (f)

Figure C.1: Damped harmonic oscillator model fits (solid lines) to the experimentally recorded (solid circles) IR response in the THz region for (a) MAPbI$_3$, (c)MAPbBr$_{1.5}$I$_{1.5}$, (e) MAPbBr$_3$ thin films. Fits reflect the sum over two phonon modes. Damped harmonic oscillator model fits (solid lines) to the experimentally recorded (solid circles) Raman response of (b) MAPbI$_3$, (d) MAPbBr$_{1.5}$I$_{1.5}$, (f) MAPbBr$_3$ thin films. Fits reflect the sum over three phonon modes, together with a small quasi-elastic (QE) scattering response.

References

[1] *IPCC Climate Change 2023 Synthesis Report*. `www.ipcc.ch/report/ar6/syr/`. Accessed: 2024-08-14.

[2] *Renewable Energy Statistics 2024*. `www.irena.org/Publications/2024/Jul/Renewable-energy-statistics-2024`. Accessed: 2024-08-14.

[3] *COP28 Tripling Renewable Capacity Pledge*. `www.iea.org/reports/cop28-tripling-renewable-capacity-pledge`. Accessed: 2024-08-14.

[4] *Best Research-Cell Efficiency Chart*. `www.nrel.gov/pv/cell-efficiency.html`. Accessed: 2024-07-17.

[5] Polman, A.; Knight, M.; Garnett, E. C.; Ehrler, B. and Sinke, W. C. 'Photovoltaic Materials: Present Efficiencies and Future Challenges'. *Science*, 2016, **352**, aad4424.

[6] Kittel, C. and McEuen, P. *Introduction to solid state physics*. John Wiley & Sons, 2004.

[7] Simon, S. H. *The Oxford solid state basics*. Oxford University Press, 2013.

[8] Singleton, J. *Band Theory and Electronic Properties of Solids*. Oxford University Press, 2001.

[9] Fakharuddin, A.; Gangishetty, M. K.; Abdi-Jalebi, M.; Chin, S.-H.; Mohd Yusoff, A. R. bin; Congreve, D. N.; Tress, W.; Deschler, F.; Vasilopoulou, M. and Bolink, H. J. 'Perovskite Light-emitting Diodes'. *Nat. Electron.*, 2022, **5**, 203–216.

[10] Stranks, S. D. and Snaith, H. J. 'Metal-Halide Perovskites for Photovoltaic and Light-Emitting Devices'. *Nat. Nanotechnol.*, 2015, **10**, 391–402.

[11] Shockley, W and Queisser, H. 'Detailed Balance Limit of Efficiency of p-n Junction Solar Cells'. *J. Appl. Phys.*, 1961, **32**, 510.

[12] Eperon, G. E.; Leijtens, T.; Bush, K. A.; Prasanna, R.; Green, T.; Wang, J. T.-W.; McMeekin, D. P.; Volonakis, G.; Milot, R. L.; May, R.; Palmstrom, A.; Slotcavage, D. J.; Belisle, R. A.; Patel, J. B.; Parrott, E. S.; Sutton, R. J.; Ma, W.; Moghadam, F.; Conings, B.; Babayigit, A.; Boyen, H.-G.; Bent, S.; Giustino, F.; Herz, L. M.; Johnston, M. B. *et al.* 'Perovskite-Perovskite Tandem Photovoltaics with Optimized Band Gaps'. *Science*, 2016, **354**, 861–865.

[13] Herz, L. M. 'Charge-Carrier Dynamics in Organic-Inorganic Metal Halide Perovskites'. *Ann. Phys. Chem.*, 2016, **67**, 65–89.

[14] Boyd, C. C.; Cheacharoen, R.; Leijtens, T. and McGehee, M. D. 'Understanding Degradation Mechanisms and Improving Stability of Perovskite Photovoltaics'. *Chem. Rev.*, 2018, **119**, 3418–3451.

[15] Knight, A. J. and Herz, L. M. 'Preventing Phase Segregation in Mixed-Halide Perovskites: A Perspective'. *Energy Environ. Sci.*, 2020, **13**, 2024–2046.

[16] Hoke, E. T.; Slotcavage, D. J.; Dohner, E. R.; Bowring, A. R.; Karunadasa, H. I. and McGehee, M. D. 'Reversible Photo-Induced Trap Formation in Mixed-Halide Hybrid Perovskites for Photovoltaics'. *Chem. Sci.*, 2015, **6**, 613–617.

[17] Goldschmidt, V. M. 'Die Gesetze der Krystallochemie'. *Naturwissenschaften*, 1926, **14**, 477–485.

[18] Zhang, Z.; Liu, Y.; Sun, Q.; Ban, H.; Liu, Z.; Yu, H.; Li, X.; Dai, L.; Yang, W.; Shen, Y. *et al.* 'The Importance of Elemental Lead To Perovskites Photovoltaics'. *Chem. Inorg. Mater.*, 2023, **1**, 100017.

[19] Xiao, Z. and Yan, Y. 'Progress in Theoretical Study of Metal Halide Perovskite Solar Cell Materials'. *Adv. Energy Mater.*, 2017, **7**, 1701136.

[20] Davies, C. L.; Filip, M. R.; Patel, J. B.; Crothers, T. W.; Verdi, C.; Wright, A. D.; Milot, R. L.; Giustino, F.; Johnston, M. B. and Herz, L. M. 'Bimolecular Recombination in Methylammonium Lead Triiodide Perovskite Is an Inverse Absorption Process'. *Nat. Commun.*, 2018, **9**, 293.

[21] Conings, B.; Drijkoningen, J.; Gauquelin, N.; Babayigit, A.; D'Haen, J.; D'Olieslaeger, L.; Ethirajan, A.; Verbeeck, J.; Manca, J.; Mosconi, E.; Angelis, F. D. and Boyen, H.-G. 'Intrinsic Thermal Instability of Methylammonium Lead Trihalide Perovskite'. *Adv. Energy Mater.*, 2015, **5**, 1500477.

[22] Prasanna, R.; Gold-Parker, A.; Leijtens, T.; Conings, B.; Babayigit, A.; Boyen, H.-G.; Toney, M. F. and McGehee, M. D. 'Band Gap Tuning via Lattice Contraction and Octahedral Tilting in Perovskite Materials for Photovoltaics'. *J. Am. Chem. Soc.*, 2017, **139**, 11117–11124.

[23] McMeekin, D. P.; Sadoughi, G.; Rehman, W.; Eperon, G. E.; Saliba, M.; Hörantner, M. T.; Haghighirad, A.; Sakai, N.; Korte, L.; Rech, B.; Johnston, M. B.; Herz, L. M. and Snaith, H. J. 'A Mixed-Cation Lead Mixed-Halide Perovskite Absorber for Tandem Solar Cells'. *Science*, 2016, **351**, 151–155.

[24] Rehman, W.; McMeekin, D. P.; Patel, J. B.; Milot, R. L.; Johnston, M. B.; Snaith, H. J. and Herz, L. M. 'Photovoltaic Mixed-Cation Lead Mixed-Halide Perovskites: Links Between Crystallinity, Photo-Stability and Electronic Properties'. *Energy Environ. Sci.*, 2017, **10**, 361–369.

[25] Saliba, M.; Matsui, T.; Seo, J.-Y.; Domanski, K.; Correa-Baena, J.-P.; Nazeeruddin, M. K.; Zakeeruddin, S. M.; Tress, W.; Abate, A.; Hagfeldt, A. *et al.* 'Cesium-Containing Triple Cation Perovskite Solar Cells: Improved Stability, Reproducibility and High Efficiency'. *Energy Environ. Sci.*, 2016, **9**, 1989–1997.

[26] Ponti, C.; Nasti, G.; Di Girolamo, D.; Cantone, I.; Alharthi, F. A. and Abate, A. 'Environmental Lead Exposure From Halide Perovskites in Solar Cells'. *Trends Ecol. Evol.*, 2022, **37**, 281–283.

[27] Ke, W. and Kanatzidis, M. G. 'Prospects for Low-Toxicity Lead-Free Perovskite Solar Cells'. *Nat. Commun.*, 2019, **10**, 965.

[28] Yu, B.-B.; Chen, Z.; Zhu, Y.; Wang, Y.; Han, B.; Chen, G.; Zhang, X.; Du, Z. and He, Z. 'Heterogeneous 2D/3D Tin-Halides Perovskite Solar Cells With Certified Conversion Efficiency Breaking 14%'. *Adv. Mater.*, 2021, **33**, 2102055.

[29] Bowman, A. R.; Klug, M. T.; Doherty, T. A.; Farrar, M. D.; Senanayak, S. P.; Wenger, B.; Divitini, G.; Booker, E. P.; Andaji-Garmaroudi, Z.; Macpherson, S. *et al.* 'Microsecond Carrier Lifetimes, Controlled P-Doping, and Enhanced Air Stability in Low-Bandgap Metal Halide Perovskites'. *ACS Energy Lett.*, 2019, **4**, 2301–2307.

[30] Meggiolaro, D.; Ricciarelli, D.; Alasmari, A. A.; Alasmary, F. A. and De Angelis, F. 'Tin Versus Lead Redox Chemistry Modulates Charge Trapping and Self-Doping in Tin/Lead Iodide Perovskites'. *J. Phys. Chem. Lett.*, 2020, **11**, 3546–3556.

[31] Kumar, M. H.; Dharani, S.; Leong, W. L.; Boix, P. P.; Prabhakar, R. R.; Baikie, T.; Shi, C.; Ding, H.; Ramesh, R.; Asta, M. *et al.* 'Lead-Free Halide Perovskite Solar Cells With High Photocurrents Realized Through Vacancy Modulation'. *Adv. Mater.*, 2014, **26**, 7122–7127.

[32] Savill, K. J.; Ulatowski, A. M. and Herz, L. M. 'Optoelectronic Properties of Tin–Lead Halide Perovskites'. *ACS Energy Lett.*, 2021, **6**, 2413–2426.

[33] Savill, K. J.; Ulatowski, A. M.; Farrar, M. D.; Johnston, M. B.; Snaith, H. J. and Herz, L. M. 'Impact of Tin Fluoride Additive on the Properties of Mixed Tin-Lead Iodide Perovskite Semiconductors'. *Adv. Funct. Mater.*, 2020, **30**, 2005594.

[34] Milot, R. L.; Klug, M. T.; Davies, C. L.; Wang, Z.; Kraus, H.; Snaith, H. J.; Johnston, M. B. and Herz, L. M. 'The Effects of Doping Density and Temperature on the Optoelectronic Properties of Formamidinium Tin Triiodide Thin Films'. *Adv. Mater.*, 2018, **30**, 1804506.

[35] Prasanna, R.; Leijtens, T.; Dunfield, S. P.; Raiford, J. A.; Wolf, E. J.; Swifter, S. A.; Werner, J.; Eperon, G. E.; Paula, C. de; Palmstrom, A. F. *et al.* 'Design of Low Bandgap Tin–Lead Halide Perovskite Solar Cells to Achieve Thermal, Atmospheric and Operational Stability'. *Nat. Energy*, 2019, **4**, 939–947.

[36] Parrott, E. S.; Green, T.; Milot, R. L.; Johnston, M. B.; Snaith, H. J. and Herz, L. M. 'Interplay of Structural and Optoelectronic Properties in Formamidinium Mixed Tin–Lead Triiodide Perovskites'. *Adv. Funct. Mater.*, 2018, **28**, 1802803.

[37] Rajagopal, A.; Stoddard, R. J.; Hillhouse, H. W. and Jen, A. K.-Y. 'On Understanding Bandgap Bowing and Optoelectronic Quality in Pb–Sn Alloy Hybrid Perovskites'. *J. Mater. Chem. A*, 2019, **7**, 16285–16293.

[38] Hao, F.; Stoumpos, C. C.; Chang, R. P. and Kanatzidis, M. G. 'Anomalous Band Gap Behavior in Mixed SN and Pb Perovskites Enables Broadening of Absorption Spectrum in Solar Cells'. *J. Am. Chem. Soc.*, 2014, **136**, 8094–8099.

[39] Kapil, G.; Bessho, T.; Sanehira, Y.; Sahamir, S. R.; Chen, M.; Baranwal, A. K.; Liu, D.; Sono, Y.; Hirotani, D.; Nomura, D. *et al.* 'Tin–Lead Perovskite Solar Cells Fabricated on Hole Selective Monolayers'. *ACS Energy Lett.*, 2022, **7**, 966–974.

[40] Seo, J.; Song, T.; Rasool, S.; Park, S. and Kim, J. Y. 'An Overview of Lead, Tin, and Mixed Tin–Lead-Based ABI_3 Perovskite Solar Cells'. *Adv. Energy Sustainability Res.*, 2023, **4**, 2200160.

[41] Leijtens, T.; Prasanna, R.; Gold-Parker, A.; Toney, M. F. and McGehee, M. D. 'Mechanism of Tin Oxidation and Stabilization by Lead Substitution in Tin Halide Perovskites'. *ACS Energy Lett.*, 2017, **2**, 2159–2165.

[42] Walsh, A. 'Principles of Chemical Bonding and Band Gap Engineering in Hybrid Organic–Inorganic Halide Perovskites'. *J. Phys. Chem. C*, 2015, **119**, 5755–5760.

[43] Protesescu, L.; Yakunin, S.; Bodnarchuk, M. I.; Krieg, F.; Caputo, R.; Hendon, C. H.; Yang, R. X.; Walsh, A. and Kovalenko, M. V. 'Nanocrystals of Cesium Lead Halide Perovskites ($CsPbX_3$, X = Cl, Br, and I): Novel Optoelectronic Materials Showing Bright Emission with Wide Color Gamut'. *Nano Lett.*, 2015, **15**, 3692–3696.

[44] Noh, J. H.; Im, S. H.; Heo, J. H.; Mandal, T. N. and Seok, S. I. 'Chemical Management for Colorful, Efficient, and Stable Inorganic–Organic Hybrid Nanostructured Solar Cells'. *Nano Lett.*, 2013, **13**, 1764–1769.

[45] Beal, R. E.; Slotcavage, D. J.; Leijtens, T.; Bowring, A. R.; Belisle, R. A.; Nguyen, W. H.; Burkhard, G. F.; Hoke, E. T. and McGehee, M. D. 'Cesium Lead Halide Perovskites with Improved Stability for Tandem Solar Cells'. *J. Phys. Chem. Lett.*, 2016, **7**, 746–751.

[46] Chen, Z.; Brocks, G.; Tao, S. and Bobbert, P. A. 'Unified Theory for Light-Induced Halide Segregation in Mixed Halide Perovskites'. *Nat. Commun.*, 2021, **12**, 2687.

[47] Draguta, S.; Sharia, O.; Yoon, S. J.; Brennan, M. C.; Morozov, Y. V.; Manser, J. S.; Kamat, P. V.; Schneider, W. F. and Kuno, M. 'Rationalizing the Light-Induced Phase Separation of Mixed Halide Organic–Inorganic Perovskites'. *Nat. Commun.*, 2017, 200.

[48] Tao, S.; Schmidt, I.; Brocks, G.; Jiang, J.; Tranca, I.; Meerholz, K. and Olthof, S. 'Absolute Energy Level Positions in Tin- and Lead-Based Halide Perovskites'. *Nat. Commun.*, 2019, **10**, 2560.

[49] Endres, J.; Kulbak, M.; Zhao, L.; Rand, B. P.; Cahen, D.; Hodes, G. and Kahn, A. 'Electronic Structure of the $CsPbBr_3$/Polytriarylamine (PTAA) System'. *J. Appl. Phys.*, 2017, **121**, 035304.

[50] Braly, I. L.; Stoddard, R. J.; Rajagopal, A.; Uhl, A. R.; Katahara, J. K.; Jen, A. K.-Y. and Hillhouse, H. W. 'Current-Induced Phase Segregation in Mixed Halide Hybrid Perovskites and Its Impact on Two-Terminal Tandem Solar Cell Design'. *ACS Energy Lett.*, 2017, 1841–1847.

[51] Mao, W.; Hall, C. R.; Bernardi, S.; Cheng, Y.-B.; Widmer-Cooper, A.; Smith, T. A. and Bach, U. 'Light-Induced Reversal of Ion Segregation in Mixed-Halide Perovskites'. *Nat. Mater.*, 2021, **20**, 55–61.

[52] Knight, A. J.; Patel, J. B.; Snaith, H. J.; Johnston, M. B. and Herz, L. M. 'Trap States, Electric Fields, and Phase Segregation in Mixed-Halide Perovskite Photovoltaic Devices'. *Adv. Energy Mater.*, 2020, **10**, 1903488.

[53] Samu, G. F.; Janáky, C. and Kamat, P. V. 'A Victim of Halide Ion Segregation. How Light Soaking Affects Solar Cell Performance of Mixed Halide Lead Perovskites'. *ACS Energy Lett.*, 2017, **2**, 1860–1861.

[54] Duong, T.; Mulmudi, H. K.; Wu, Y.; Fu, X.; Shen, H.; Peng, J.; Wu, N.; Nguyen, H. T.; Macdonald, D.; Lockrey, M.; White, T. P.; Weber, K. and Catchpole, K. 'Light and Electrically Induced Phase Segregation and Its Impact on the Stability of Quadruple Cation High Bandgap Perovskite Solar Cells'. *ACS Appl. Mater. Interfaces*, 2017, **9**, 26859–26866.

[55] Mahesh, S.; Ball, J. M.; Oliver, R. D. J.; McMeekin, D. P.; Nayak, P. K.; Johnston, M. B. and Snaith, H. J. 'Revealing the Origin of Voltage Loss in Mixed-Halide Perovskite Solar Cells'. *Energy Environ. Sci.*, 1 2020, **13**, 258–267.

[56] Motti, S. G.; Patel, J. B.; Oliver, R. D.; Snaith, H. J.; Johnston, M. B. and Herz, L. M. ‘Phase Segregation in Mixed-Halide Perovskites Affects Charge-Carrier Dynamics While Preserving Mobility’. *Nat. Commun.*, 2021, **12**, 1–9.

[57] Knight, A. J.; Borchert, J.; Oliver, R. D. J.; Patel, J. B.; Radaelli, P. G.; Snaith, H. J.; Johnston, M. B. and Herz, L. M. ‘Halide Segregation in Mixed-Halide Perovskites: Influence of A-Site Cations’. *ACS Energy Lett.*, 2021, **6**, 799–808.

[58] Mathew, P. S.; Samu, G. F.; Janáky, C. and Kamat, P. V. ‘Iodine (I) Expulsion at Photoirradiated Mixed Halide Perovskite Interface. *Should I Stay or Should I Go?*’ *ACS Energy Lett.*, 2020, 1872–1880.

[59] Elmelund, T.; Scheidt, R. A.; Seger, B. and Kamat, P. V. ‘Bidirectional Halide Ion Exchange in Paired Lead Halide Perovskite Films with Thermal Activation’. *ACS Energy Lett.*, 2019, 1961–1969.

[60] Shao, Y.; Fang, Y.; Li, T.; Wang, Q.; Dong, Q.; Deng, Y.; Yuan, Y.; Wei, H.; Wang, M.; Gruverman, A.; Shield, J. and Huang, J. ‘Grain Boundary Dominated Ion Migration in Polycrystalline Organic–Inorganic Halide Perovskite Films’. *Energy Environ. Sci.*, 2016, 1752–1759.

[61] Yang, B.; Brown, C. C.; Huang, J.; Collins, L.; Sang, X.; Unocic, R. R.; Jesse, S.; Kalinin, S. V.; Belianinov, A.; Jakowski, J.; Geohegan, D. B.; Sumpter, B. G.; Xiao, K. and Ovchinnikova, O. S. ‘Enhancing Ion Migration in Grain Boundaries of Hybrid Organic–Inorganic Perovskites by Chlorine’. *Adv. Funct. Mater.*, 2017, **27**, 1700749.

[62] Yun, J. S.; Seidel, J.; Kim, J.; Soufiani, A. M.; Huang, S.; Lau, J.; Jeon, N. J.; Seok, S. I.; Green, M. A. and Ho-Baillie, A. ‘Critical Role of Grain Boundaries for Ion Migration in Formamidinium and Methylammonium Lead Halide Perovskite Solar Cells’. *Adv. Energy Mater.*, 2016, **6**, 1600330.

[63] Abdi-Jalebi, M.; Andaji-Garmaroudi, Z.; Cacovich, S.; Stavrakas, C.; Philippe, B.; Richter, J. M.; Alsari, M.; Booker, E. P.; Hutter, E. M.; Pearson, A. J.; Lilliu, S.; Savenije, T. J.; Rensmo, H.; Divitini, G.; Ducati, C.; Friend, R. H. and Stranks, S. D. ‘Maximizing and Stabilizing Luminescence from Halide Perovskites with Potassium Passivation’. *Nature*, 2018, **555**, 497–501.

[64] Belisle, R. A.; Bush, K. A.; Bertoluzzi, L.; Gold-Parker, A.; Toney, M. F. and McGehee, M. D. ‘Impact of Surfaces on Photoinduced Halide Segregation in Mixed-Halide Perovskites’. *ACS Energy Lett.*, 2018, **3**, 2694–2700.

[65] Wang, Z.; Wang, Y.; Nie, Z.; Ren, Y. and Zeng, H. ‘Laser Induced Ion Migration in All-Inorganic Mixed Halide Perovskite Micro-Platelets’. *Nanoscale Adv.*, 2019, **1**, 4459–4465.

[66] Balakrishna, R. G.; Kobosko, S. M. and Kamat, P. V. ‘Mixed Halide Perovskite Solar Cells. Consequence of Iodide Treatment on Phase Segregation Recovery’. *ACS Energy Lett.*, 2018, **3**, 2267–2272.

[67] Li, W.; Rothmann, M. U.; Liu, A.; Wang, Z.; Zhang, Y.; Pascoe, A. R.; Lu, J.; Jiang, L.; Chen, Y.; Huang, F.; Peng, Y.; Bao, Q.; Etheridge, J.; Bach, U. and Cheng, Y.-B. ‘Phase segregation enhanced ion movement in efficient inorganic CsPbIBr2 solar cells’. *Adv. Energy Mater.*, 2017, **7**, 1700946.

[68] Tang, X.; Berg, M. van den; Gu, E.; Horneber, A.; Matt, G. J.; Osvet, A.; Meixner, A. J.; Zhang, D. and Brabec, C. J. ‘Local Observation of Phase Segregation in Mixed-Halide Perovskite’. *Nano Lett.*, 2018, **18**, 2172–2178.

[69] Knight, A. J.; Wright, A. D.; Patel, J. B.; McMeekin, D. P.; Snaith, H. J.; Johnston, M. B. and Herz, L. M. 'Electronic Traps and Phase Segregation in Lead Mixed-Halide Perovskite'. *ACS Energy Lett.*, 2019, **4**, 75–84.

[70] Brivio, F.; Caetano, C. and Walsh, A. 'Thermodynamic Origin of Photoinstability in the $CH_3NH_3Pb(I_{1-x}Br_x)_3$ Hybrid Halide Perovskite Alloy'. *J. Phys. Chem. Lett*, 2016, **7**, 1083–1087.

[71] Bischak, C. G.; Wong, A. B.; Lin, E.; Limmer, D. T.; Yang, P. and Ginsberg, N. S. 'Tunable Polaron Distortions Control the Extent of Halide Demixing in Lead Halide Perovskites'. *J. Phys. Chem. Lett.*, 2018, **9**, 3998–4005.

[72] Bischak, C. G.; Hetherington, C. L.; Wu, H.; Aloni, S.; Ogletree, D. F.; Limmer, D. T. and Ginsberg, N. S. 'Origin of Reversible Photoinduced Phase Separation in Hybrid Perovskites'. *Nano Lett.*, 2017, **17**, 1028–1033.

[73] Samu, G. F.; Balog, Á.; De Angelis, F.; Meggiolaro, D.; Kamat, P. V. and Janáky, C. 'Electrochemical Hole Injection Selectively Expels Iodide From Mixed Halide Perovskite Films'. *J. Am. Chem. Soc.*, 2019, **141**, 10812–10820.

[74] Kerner, R. A.; Xu, Z.; Larson, B. W. and Rand, B. P. 'The Role of Halide Oxidation in Perovskite Halide Phase Separation'. *Joule*, 2021, **5**, 2273–2295.

[75] DuBose, J. T. and Kamat, P. V. 'TiO_2-Assisted Halide Ion Segregation in Mixed Halide Perovskite Films'. *J. Am. Chem. Soc.*, 2020, **142**, 5362–5370.

[76] Kojima, A.; Teshima, K.; Shirai, Y. and Miyasaka, T. 'Organometal Halide Perovskites as Visible-Light Sensitizers for Photovoltaic Cells'. *J. Am. Chem. Soc.*, 2009, **131**, 6050–6051.

[77] Liu, M.; Johnston, M. B. and Snaith, H. J. 'Efficient Planar Heterojunction Perovskite Solar Cells by Vapor Deposition'. *Nature*, 2013, **501**, 395–398.

[78] Mora-Seró, I. 'How Do Perovskite Solar Cells Work?' *Joule*, 2018, **2**, 585–587.

[79] Wehrenfennig, C.; Liu, M.; Snaith, H. J.; Johnston, M. B. and Herz, L. M. 'Charge-carrier Dynamics in Vapour-deposited Films of the Organolead Halide Perovskite $CH_3NH_3PbI_{3-x}Cl_x$'. *Energy Environ. Sci.*, 2014, **7**, 2269–2275.

[80] Milot, R. L.; Eperon, G. E.; Green, T.; Snaith, H. J.; Johnston, M. B. and Herz, L. M. 'Radiative Monomolecular Recombination Boosts Amplified Spontaneous Emission in $HC(NH_2)_2SnI_3$ Perovskite Films'. *J. Phys. Chem. Lett.*, 2016, **7**, 4178–4184.

[81] Crothers, T. W.; Milot, R. L.; Patel, J. B.; Parrott, E. S.; Schlipf, J.; Muller-Buschbaum, P.; Johnston, M. B. and Herz, L. M. 'Photon Reabsorption Masks Intrinsic Bimolecular Charge-Carrier Recombination in $CH_3NH_3PbI_3$ Perovskite'. *Nano Lett.*, 2017, **17**, 5782–5789.

[82] Lin, Q.; Wang, Z.; Snaith, H. J.; Johnston, M. B. and Herz, L. M. 'Hybrid Perovskites: Prospects for Concentrator Solar Cells'. *Adv. Sci.*, 2018, **5**, 1700792.

[83] Jiang, Y.; Cui, M.; Li, S.; Sun, C.; Huang, Y.; Wei, J.; Zhang, L.; Lv, M.; Qin, C.; Liu, Y. *et al.* 'Reducing the Impact of Auger Recombination in Quasi-2D Perovskite Light-Emitting Diodes'. *Nat. Commun.*, 2021, **12**, 336.

[84] Mosconi, E.; Meggiolaro, D.; Snaith, H. J.; Stranks, S. D. and De Angelis, F. 'Light-Induced Annihilation of Frenkel Defects in Organo-Lead Halide Perovskites'. *Energy Environ. Sci.*, 2016, **9**, 3180–3187.

[85] Castro-Méndez, A.-F.; Hidalgo, J. and Correa-Baena, J.-P. 'The Role of Grain Boundaries in Perovskite Solar Cells'. *Adv. Energy Mater.*, 2019, **9**, 1901489.

[86] Park, K.; Lee, J.-H. and Lee, J.-W. 'Surface Defect Engineering of Metal Halide Perovskites for Photovoltaic Applications'. *ACS Energy Lett.*, 2022, **7**, 1230–1239.

[87] Steirer, K. X.; Schulz, P.; Teeter, G.; Stevanovic, V.; Yang, M.; Zhu, K. and Berry, J. J. 'Defect Tolerance in Methylammonium Lead Triiodide Perovskite'. *ACS Energy Lett.*, 2016, **1**, 360–366.

[88] Kang, J. and Wang, L.-W. 'High Defect Tolerance in Lead Halide Perovskite $CsPbBr_3$'. *J. Phys. Chem. Lett.*, 2017, **8**, 489–493.

[89] Leijtens, T.; Eperon, G. E.; Barker, A. J.; Grancini, G.; Zhang, W.; Ball, J. M.; Kandada, A. R. S.; Snaith, H. J. and Petrozza, A. 'Carrier Trapping and Recombination: the Role of Defect Physics in Enhancing the Open Circuit Voltage of Metal Halide Perovskite Solar Cells'. *Energy Environ. Sci.*, 2016, **9**, 3472–3481.

[90] Urbach, F. 'The Long-Wavelength Edge of Photographic Sensitivity and of the Electronic Absorption of Solids'. *Phys. Rev.*, 1953, **92**, 1324.

[91] De Wolf, S.; Holovsky, J.; Moon, S.-J.; Löper, P.; Niesen, B.; Ledinsky, M.; Haug, F.-J.; Yum, J.-H. and Ballif, C. 'Organometallic Halide Perovskites: Sharp Optical Absorption Edge and Its Relation to Photovoltaic Performance'. *J. Phys. Chem. Lett.*, 2014, **5**, 1035–1039.

[92] Elliott, R. 'Intensity of Optical Absorption by Excitons'. *Phys. Rev.*, 1957, **108**, 1384.

[93] Wright, A. D.; Volonakis, G.; Borchert, J.; Davies, C. L.; Giustino, F.; Johnston, M. B. and Herz, L. M. 'Intrinsic Quantum Confinement in Formamidinium Lead Triiodide Perovskite'. *Nat. Mater.*, 2020, **19**, 1201–1206.

[94] Ball, J. M.; Buizza, L.; Sansom, H. C.; Farrar, M. D.; Klug, M. T.; Borchert, J.; Patel, J.; Herz, L. M.; Johnston, M. B. and Snaith, H. J. 'Dual-Source Coevaporation of Low-Bandgap $FA_{1-x}Cs_xSn_{1-y}Pb_yI_3$ Perovskites for Photovoltaics'. *ACS Energy Lett.*, 2019, **4**, 2748–2756.

[95] Ulatowski, A. M.; Elmestekawy, K. A.; Patel, J. B.; Noel, N. K.; Yan, S.; Kraus, H.; Huggard, P. G.; Johnston, M. B. and Herz, L. M. 'Contrasting Charge-Carrier Dynamics across Key Metal-Halide Perovskite Compositions through In Situ Simultaneous Probes'. *Adv. Funct. Mater.*, 2023, **33**, 2305283.

[96] Zhu, Y.; Cui, Q.; Chen, J.; Chen, F.; Shi, Z.; Zhao, X. and Xu, C. 'Inhomogeneous Trap-State-Mediated Ultrafast Photocarrier Dynamics in $CsPbBr_3$ Microplates'. *ACS Appl. Mater. Interfaces*, 2021, **13**, 6820–6829.

[97] Savill, K. J.; Klug, M. T.; Milot, R. L.; Snaith, H. J. and Herz, L. M. 'Charge-Carrier Cooling and Polarization Memory Loss in Formamidinium Tin Triiodide'. *J. Phys. Chem. Lett.*, 2019, **10**, 6038–6047.

[98] Seifert, T.; Jaiswal, S; Martens, U; Hannegan, J; Braun, L.; Maldonado, P.; Freimuth, F; Kronenberg, A; Henrizi, J; Radu, I *et al.* 'Efficient Metallic Spintronic Emitters of Ultrabroadband Terahertz Radiation'. *Nat. Photonics*, 2016, **10**, 483–488.

[99] Lim, V. J.-Y.; Ulatowski, A. M.; Kamaraki, C.; Klug, M. T.; Miranda Perez, L.; Johnston, M. B. and Herz, L. M. 'Air-Degradation Mechanisms in Mixed Lead-Tin Halide Perovskites for Solar Cells'. *Adv. Energy Mater.*, 2023, **13**, 2200847.

[100] Ulatowski, A. M.; Herz, L. M. and Johnston, M. B. ‘Terahertz Conductivity Analysis for Highly Doped Thin-Film Semiconductors’. *J. Infrared Millim. Terahertz Waves*, 2020, **41**, 1431–1449.

[101] Tinkham, M. ‘Energy Gap Interpretation of Experiments on Infrared Transmission through Superconducting Films’. *Phys. Rev.*, 1956, **104**, 845.

[102] Glover III, R. and Tinkham, M. ‘Conductivity of Superconducting Films for Photon Energies between 0.3 and $40kT_c$’. *Phys. Rev.*, 1957, **108**, 243.

[103] Davies, C. L.; Patel, J. B.; Xia, C. Q.; Herz, L. M. and Johnston, M. B. ‘Temperature-Dependent Refractive Index of Quartz at Terahertz Frequencies’. *J. Infrared Millim. Terahertz Waves*, 2018, **39**, 1236–1248.

[104] Glebov, A. L.; Mokhun, O.; Rapaport, A.; Vergnole, S.; Smirnov, V. and Glebov, L. B. ‘Volume Bragg Gratings as Ultra-Narrow and Multiband Optical Filters’. *Proc. SPIE*, 2012, **8428**, 84280C.

[105] Long, D. A. *‘The Raman Effect: A Unified Treatment of the Theory of Raman Scattering by Molecules’.* Wiley, 2002.

[106] Lim, V. J.-Y.; Knight, A. J.; Oliver, R. D.; Snaith, H. J.; Johnston, M. B. and Herz, L. M. ‘Impact of Hole-Transport Layer and Interface Passivation on Halide Segregation in Mixed-Halide Perovskites’. *Adv. Funct. Mater.*, 2022, **32**, 2204825.

[107] Juarez-Perez, E. J.; Wu*β*ler, M.; Fabregat-Santiago, F.; Lakus-Wollny, K.; Mankel, E.; Mayer, T.; Jaegermann, W. and Mora-Sero, I. ‘Role of the Selective Contacts in the Performance of Lead Halide Perovskite Solar Cells’. *J. Phys. Chem. Lett*, 2014, **5**, 680–685.

[108] Le Corre, V. M.; Stolterfoht, M.; Perdigón Toro, L.; Feuerstein, M.; Wolff, C.; Gil-Escrig, L.; Bolink, H. J.; Neher, D. and Koster, L. J. A. ‘Charge Transport Layers Limiting the Efficiency of Perovskite Solar Cells: How To Optimize Conductivity, Doping, and Thickness’. *ACS Appl. Energy Mater.*, 2019, **2**, 6280–6287.

[109] Azpiroz, J. M.; Mosconi, E.; Bisquert, J. and Angelis, F. D. ‘Defect Migration in Methylammonium Lead Iodide and Its Role in Perovskite Solar Cell Operation’. *Energy Environ. Sci.*, 2015, **8**, 2118–2127.

[110] Wolff, C. M.; Caprioglio, P.; Stolterfoht, M. and Neher, D. ‘Nonradiative Recombination in Perovskite Solar Cells: The Role of Interfaces’. *Adv. Mater.*, 2019, **31**, 1902762.

[111] Gharibzadeh, S.; Fassl, P.; Hossain, I. M.; Rohrbeck, P.; Frericks, M.; Schmidt, M.; Khan, M. R.; Abzieher, T.; Nejand, B. A.; Schackmar, F. *et al.* ‘Two Birds With One Stone: Dual Grain-Boundary and Interface Passivation Enables >22% Efficient Inverted Methylammonium-Free Perovskite Solar Cells’. *Energy Environ. Sci.*, 2021, **14**, 5875–5893.

[112] Vashishtha, P. and Halpert, J. E. ‘Field-Driven Ion Migration and Color Instability in Red-Emitting Mixed Halide Perovskite Nanocrystal Light-Emitting Diodes’. *Chem. Mater.*, 2017, **29**, 5965–5973.

[113] Leijtens, T.; Bush, K. A.; Prasanna, R. and McGehee, M. D. ‘Opportunities and Challenges for Tandem Solar Cells Using Metal Halide Perovskite Semiconductors’. *Nat. Energy*, 2018, **3**, 828–838.

[114] Bush, K. A.; Palmstrom, A. F.; Yu, Z. J.; Boccard, M.; Cheacharoen, R.; Mailoa, J. P.; McMeekin, D. P.; Hoye, R. L. Z.; Bailie, C. D.; Leijtens, T.; Peters, I. M.; Minichetti, M. C.; Rolston, N.; Prasanna, R.; Sofia, S.; Harwood, D.; Ma, W.; Moghadam, F.; Snaith, H. J.; Buonassisi, T.; Holman, Z. C.; Bent, S. F. and McGehee, M. D. '23.6%-Efficient Monolithic Perovskite/Silicon Tandem Solar Cells with Improved Stability'. *Nat. Energy*, 2017, **2**, 17009.

[115] Xiao, K.; Lin, R.; Han, Q.; Hou, Y.; Qin, Z.; Nguyen, H. T.; Wen, J.; Wei, M.; Yeddu, V.; Saidaminov, M. I.; Gao, Y.; Luo, X.; Wang, Y.; Gao, H.; Zhang, C.; Xu, J.; Zhu, J.; Sargent, E. H. and Tan, H. 'All-Perovskite Tandem Solar Cells with 24.2% Certified Efficiency and Area over 1cm^2 Using Surface-Anchoring Zwitterionic Antioxidant'. *Nat. Energy*, 2020, **5**, 870–880.

[116] Ünlü, F.; Jung, E.; Haddad, J.; Kulkarni, A.; Öz, S.; Choi, H.; Fischer, T.; Chakraborty, S.; Kirchartz, T. and Mathur, S. 'Understanding the Interplay of Stability and Efficiency in A-Site Engineered Lead Halide Perovskites'. *APL Mater.*, 2020, **8**, 070901.

[117] Tian, Y.; Peter, M.; Unger, E.; Abdellah, M.; Zheng, K.; Pullerits, T.; Yartsev, A.; Sundström, V. and Scheblykin, I. G. 'Mechanistic Insights into Perovskite Photoluminescence Enhancement: Light Curing with Oxygen Can Boost Yield Thousandfold'. *Phys. Chem. Chem. Phys.*, 2015, **17**, 24978–24987.

[118] Galisteo-López, J. F.; Anaya, M.; Calvo, M. E. and Míguez, H. 'Environmental Effects on the Photophysics of Organic–Inorganic Halide Perovskites'. *J. Phys. Chem. Lett*, 2015, **6**, 2200–2205.

[119] Godding, J. S.; Ramadan, A. J.; Lin, Y.-H.; Schutt, K.; Snaith, H. J. and Wenger, B. 'Oxidative Passivation of Metal Halide Perovskites'. *Joule*, 2019, **3**, 2716–2731.

[120] Brenes, R.; Eames, C.; Bulović, V.; Islam, M. S. and Stranks, S. D. 'The Impact of Atmosphere on the Local Luminescence Properties of Metal Halide Perovskite Grains'. *Adv. Mater.*, 2018, **30**, 1706208.

[121] Lin, Y.-H.; Sakai, N.; Da, P.; Wu, J.; Sansom, H. C.; Ramadan, A. J.; Mahesh, S.; Liu, J.; Oliver, R. D. J.; Lim, J.; Aspitarte, L.; Sharma, K.; Madhu, P. K.; Morales-Vilches, A. B.; Nayak, P. K.; Bai, S.; Gao, F.; Grovenor, C. R. M.; Johnston, M. B.; Labram, J. G.; Durrant, J. R.; Ball, J. M.; Wenger, B.; Stannowski, B. and Snaith, H. J. 'A Piperidinium Salt Stabilizes Efficient Metal-Halide Perovskite Solar Cells'. *Science*, 2020, **369**, 96–102.

[122] Oliver, R. D. J.; Caprioglio, P.; Peña-Camargo, F.; Buizza, L. R. V.; Zu, F.; Ramadan, A. J.; Motti, S. G.; Mahesh, S.; McCarthy, M. M.; Warby, J. H.; Lin, Y.-H.; Koch, N.; Albrecht, S.; Herz, L. M.; Johnston, M. B.; Neher, D.; Stolterfoht, M. and Snaith, H. J. 'Understanding and Suppressing Non-radiative Losses in Methylammonium-Free Wide-Bandgap Perovskite Solar Cells'. *Energy Environ. Sci.*, 2 2022, **15**, 714–726.

[123] Brennan, M. C.; Draguta, S.; Kamat, P. V. and Kuno, M. 'Light-Induced Anion Phase Segregation in Mixed Halide Perovskites'. *ACS Energy Lett.*, 2018, **3**, 204–213.

[124] Nandi, P.; Giri, C.; Swain, D.; Manju, U.; Mahanti, S. D. and Topwal, D. 'Temperature Dependent Photoinduced Reversible Phase Separation in Mixed-Halide Perovskite'. *ACS Appl. Energy Mater.*, 2018, **1**, 3807–3814.

[125] Krückemeier, L.; Krogmeier, B.; Liu, Z.; Rau, U. and Kirchartz, T. 'Understanding Transient Photoluminescence in Halide Perovskite Layer Stacks and Solar Cells'. *Adv. Energy Mater.*, 2021, **11**, 2003489.

[126] Jacobsson, T. J.; Correa-Baena, J.-P.; Pazoki, M.; Saliba, M.; Schenk, K.; Grätzel, M. and Hagfeldt, A. 'Exploration of the Compositional Space for Mixed Lead Halogen Perovskites for High Efficiency Solar Cells'. *Energy Environ. Sci.*, 2016, **9**, 1706–1724.

[127] Caprioglio, P.; Caicedo-Davila, S.; Yang, T. C.-J.; Wolff, C. M.; Pena-Camargo, F.; Fiala, P.; Rech, B.; Ballif, C.; Abou-Ras, D.; Stolterfoht, M. *et al.* 'Nano-emitting Heterostructures Violate Optical Reciprocity and Enable Efficient Photoluminescence in Halide-Segregated Methylammonium-Free Wide Bandgap Perovskites'. *ACS Energy Lett.*, 2021, **6**, 419–428.

[128] Stolterfoht, M.; Caprioglio, P.; Wolff, C. M.; Márquez, J. A.; Nordmann, J.; Zhang, S.; Rothhardt, D.; Hörmann, U.; Amir, Y.; Redinger, A.; Kegelmann, L.; Zu, F.; Albrecht, S.; Koch, N.; Kirchartz, T.; Saliba, M.; Unold, T. and Neher, D. 'The Impact of Energy Alignment and Interfacial Recombination on the Internal and External Open-Circuit Voltage of Perovskite Solar Cells'. *Energy Environ. Sci.*, 2019, **12**, 2778–2788.

[129] Sum, T. C.; Righetto, M. and Lim, S. S. 'Quo Vadis, Perovskite Emitters?' *J. Chem. Phys.*, 2020, **152**, 130901.

[130] Zhou, Q.; Qiu, J.; Wang, Y.; Yu, M.; Liu, J. and Zhang, X. 'Multifunctional Chemical Bridge and Defect Passivation for Highly Efficient Inverted Perovskite Solar Cells'. *ACS Energy Lett.*, 2021, **6**, 1596–1606.

[131] Ball, J. M. and Petrozza, A. 'Defects in Perovskite-Halides and Their Effects in Solar Cells'. *Nat. Energy*, 2016, **1**, 1–13.

[132] Ran, C.; Xu, J.; Gao, W.; Huang, C. and Dou, S. 'Defects in Metal Triiodide Perovskite Materials Towards High-Performance Solar Cells: Origin, Impact, Characterization, and Engineering'. *Chem. Soc. Rev.*, 2018, **47**, 4581–4610.

[133] Jin, H.; Debroye, E.; Keshavarz, M.; Scheblykin, I. G.; Roeffaers, M. B. J.; Hofkens, J. and Steele, J. A. 'It's a Trap! On the Nature of Localised States and Charge Trapping in Lead Halide Perovskites'. *Mater. Horiz.*, 2020, **7**, 397–410.

[134] Meggiolaro, D. and De Angelis, F. 'First-Principles Modeling of Defects in Lead Halide Perovskites: Best Practices and Open Issues'. *ACS Energy Lett.*, 2018, **3**, 2206–2222.

[135] Meggiolaro, D.; Motti, S. G.; Mosconi, E.; Barker, A. J.; Ball, J.; Andrea Riccardo Perini, C.; Deschler, F.; Petrozza, A. and De Angelis, F. 'Iodine Chemistry Determines the Defect Tolerance of Lead-Halide Perovskites'. *Energy Environ. Sci.*, 2018, **11**, 702–713.

[136] Kim, G. and Petrozza, A. 'Defect Tolerance and Intolerance in Metal-Halide Perovskites'. *Adv. Energy Mater.*, 2020, **10**, 2001959.

[137] Barker, A. J.; Sadhanala, A.; Deschler, F.; Gandini, M.; Senanayak, S. P.; Pearce, P. M.; Mosconi, E.; Pearson, A. J.; Wu, Y.; Srimath Kandada, A. R.; Leijtens, T.; De Angelis, F.; Dutton, S. E.; Petrozza, A. and Friend, R. H. 'Defect-Assisted Photoinduced Halide Segregation in Mixed-Halide Perovskite Thin Films'. *ACS Energy Lett.*, 2017, 1416–1424.

[138] Yang, J.-N.; Song, Y.; Yao, J.-S.; Wang, K.-H.; Wang, J.-J.; Zhu, B.-S.; Yao, M.-M.; Rahman, S. U.; Lan, Y.-F.; Fan, F.-J. and Yao, H.-B. 'Potassium Bromide Surface Passivation on $CsPbI_{3-x}Br_x$ Nanocrystals for Efficient and Stable Pure Red Perovskite Light-Emitting Diodes'. *J. Am. Chem. Soc.*, 2020, **142**, 2956–2967.

[139] Ruth, A.; Brennan, M. C.; Draguta, S.; Morozov, Y. V.; Zhukovskyi, M.; Janko, B.; Zapol, P. and Kuno, M. 'Vacancy-Mediated Anion Photosegregation Kinetics in Mixed Halide Hybrid Perovskites: Coupled Kinetic Monte Carlo and Optical Measurements'. *ACS Energy Lett.*, 2018, **3**, 2321–2328.

[140] Yoon, S. J.; Kuno, M. and Kamat, P. V. 'Shift Happens. How Halide Ion Defects Influence Photoinduced Segregation in Mixed Halide Perovskites'. *ACS Energy Lett.*, 2017, **2**, 1507–1514.

[141] Brennan, M. C.; Ruth, A.; Kamat, P. V. and Kuno, M. 'Photoinduced Anion Segregation in Mixed Halide Perovskites'. *Trends Chem.*, 2020, **2**, 282–301.

[142] Gu, S.; Lin, R.; Han, Q.; Gao, Y.; Tan, H. and Zhu, J. 'Tin and Mixed Lead–Tin Halide Perovskite Solar Cells: Progress and Their Application in Tandem Solar Cells'. *Adv. Mater.*, 2020, **32**, 1907392.

[143] Sahare, S.; Pham, H. D.; Angmo, D.; Ghoderao, P.; MacLeod, J.; Khan, S. B.; Lee, S.-L.; Singh, S. P. and Sonar, P. 'Emerging Perovskite Solar Cell Technology: Remedial Actions for the Foremost Challenges'. *Adv. Energy Mater.*, 2021, **11**, 2101085.

[144] Wang, C.; Song, Z.; Li, C.; Zhao, D. and Yan, Y. 'Low-Bandgap Mixed Tin-Lead Perovskites and Their Applications in All-Perovskite Tandem Solar Cells'. *Adv. Funct. Mater.*, 2019, **29**, 1808801.

[145] Lanzetta, L.; Webb, T.; Zibouche, N.; Liang, X.; Ding, D.; Min, G.; Westbrook, R. J.; Gaggio, B.; Macdonald, T. J.; Islam, M. S. *et al.* 'Degradation Mechanism of Hybrid Tin-Based Perovskite Solar Cells and the Critical Role of Tin (IV) Iodide'. *Nat. Commun.*, 2021, **12**, 2853.

[146] Lanzetta, L.; Aristidou, N. and Haque, S. A. 'Stability of Lead and Tin Halide Perovskites: The Link Between Defects and Degradation'. *J. Phys. Chem. Lett.*, 2020, **11**, 574–585.

[147] Yao, H.; Zhou, F.; Li, Z.; Ci, Z.; Ding, L. and Jin, Z. 'Strategies for Improving the Stability of Tin-Based Perovskite ($ASnX_3$) Solar Cells'. *Adv. Sci.*, 2020, **7**, 1903540.

[148] Marshall, K. P.; Walker, M.; Walton, R. I. and Hatton, R. A. 'Enhanced Stability and Efficiency in Hole-Transport-Layer-Free $CsSnI_3$ Perovskite Photovoltaics'. *Nat. Energy*, 2016, **1**, 1–9.

[149] Ricciarelli, D.; Meggiolaro, D.; Ambrosio, F. and De Angelis, F. 'Instability of Tin Iodide Perovskites: Bulk p-Doping Versus Surface Tin Oxidation'. *ACS Energy Lett.*, 2020, **5**, 2787–2795.

[150] Noel, N. K.; Stranks, S. D.; Abate, A.; Wehrenfennig, C.; Guarnera, S.; Haghighirad, A.-A.; Sadhanala, A.; Eperon, G. E.; Pathak, S. K.; Johnston, M. B. *et al.* 'Lead-Free Organic–Inorganic Tin Halide Perovskites for Photovoltaic Applications'. *Energy Environ. Sci.*, 2014, **7**, 3061–3068.

[151] Takahashi, Y.; Obara, R.; Lin, Z.-Z.; Takahashi, Y.; Naito, T.; Inabe, T.; Ishibashi, S. and Terakura, K. 'Charge-Transport in Tin-Iodide Perovskite $CH_3NH_3SnI_3$: Origin of High Conductivity'. *Dalton Trans.*, 2011, **40**, 5563–5568.

[152] Nasti, G. and Abate, A. 'Tin Halide Perovskite (ASnX$_3$) Solar Cells: A Comprehensive Guide Toward the Highest Power Conversion Efficiency'. *Adv. Energy Mater.*, 2020, **10**, 1902467.

[153] Li, G.; Su, Z.; Li, M.; Yang, F.; Aldamasy, M. H.; Pascual, J.; Yang, F.; Liu, H.; Zuo, W.; Di Girolamo, D. *et al.* 'Ionic Liquid Stabilizing High-Efficiency Tin Halide Perovskite Solar Cells'. *Adv. Energy Mater.*, 2021, **11**, 2101539.

[154] Meng, X.; Wang, Y.; Lin, J.; Liu, X.; He, X.; Barbaud, J.; Wu, T.; Noda, T.; Yang, X. and Han, L. 'Surface-Controlled Oriented Growth of Fasni$_3$ Crystals for Efficient Lead-Free Perovskite Solar Cells'. *Joule*, 2020, **4**, 902–912.

[155] He, L.; Gu, H.; Liu, X.; Li, P.; Dang, Y.; Liang, C.; Ono, L. K.; Qi, Y. and Tao, X. 'Efficient Anti-solvent-Free Spin-Coated and Printed Sn-Perovskite Solar Cells With Crystal-Based Precursor Solutions'. *Matter*, 2020, **2**, 167–180.

[156] Liu, G.; Liu, C.; Lin, Z.; Yang, J.; Huang, Z.; Tan, L. and Chen, Y. 'Regulated Crystallization of Efficient and Stable Tin-Based Perovskite Solar Cells via a Self-Sealing Polymer'. *ACS Appl. Mater. Interfaces*, 2020, **12**, 14049–14056.

[157] Herz, L. M. 'Charge-Carrier Mobilities in Metal Halide Perovskites: Fundamental Mechanisms and Limits'. *ACS Energy Lett.*, 2017, **2**, 1539–1548.

[158] Stoumpos, C. C.; Malliakas, C. D. and Kanatzidis, M. G. 'Semiconducting Tin and Lead Iodide Perovskites With Organic Cations: Phase Transitions, High Mobilities, and Near-Infrared Photoluminescent Properties'. *Inorg. Chem.*, 2013, **52**, 9019–9038.

[159] Burstein, E. 'Anomalous Optical Absorption Limit In InSb'. *Phys. Rev.*, 1954, **93**, 632.

[160] Moss, T. S. 'The Interpretation of the Properties of Indium Antimonide'. *Proc. Phys. Soc. Sect. B*, 1954, **67**, 775.

[161] Handa, T.; Yamada, T.; Kubota, H.; Ise, S.; Miyamoto, Y. and Kanemitsu, Y. 'Photocarrier Recombination and Injection Dynamics in Long-Term Stable Lead-Free CH$_3$NH$_3$SnI$_3$ Perovskite Thin Films and Solar Cells'. *J. Phys. Chem. C*, 2017, **121**, 16158–16165.

[162] Chernikov, A.; Van Der Zande, A. M.; Hill, H. M.; Rigosi, A. F.; Velauthapillai, A.; Hone, J. and Heinz, T. F. 'Electrical Tuning of Exciton Binding Energies in Monolayer WS$_2$'. *Phys. Rev. Lett.*, 2015, **115**, 126802.

[163] Qiu, X.; Cao, B.; Yuan, S.; Chen, X.; Qiu, Z.; Jiang, Y.; Ye, Q.; Wang, H.; Zeng, H.; Liu, J. *et al.* 'From Unstable CsSnI$_3$ to Air-Stable Cs$_2$SnI$_6$: A Lead-Free Perovskite Solar Cell Light Absorber With Bandgap of 1.48 eV and High Absorption Coefficient'. *Sol. Energy Mater.*, 2017, **159**, 227–234.

[164] Kontos, A. G.; Kaltzoglou, A.; Siranidi, E.; Palles, D.; Angeli, G. K.; Arfanis, M. K.; Psycharis, V.; Raptis, Y. S.; Kamitsos, E. I.; Trikalitis, P. N. *et al.* 'Structural Stability, Vibrational Properties, and Photoluminescence in CSSNI3 Perovskite Upon the Addition of SnF$_2$'. *Inorg. Chem.*, 2017, **56**, 84–91.

[165] Kaltzoglou, A.; Perganti, D.; Antoniadou, M.; Kontos, A. G. and Falaras, P. 'Stress Tests on Dye-Sensitized Solar Cells With the Cs$_2$SnI$_6$ Defect Perovskite as Hole-Transporting Material'. *Energy Procedia*, 2016, **102**, 49–55.

[166] El Ajjouri, Y.; Locardi, F.; Gélvez-Rueda, M. C.; Prato, M.; Sessolo, M.; Ferretti, M.; Grozema, F. C.; Palazon, F. and Bolink, H. J. 'Mechanochemical Synthesis of Sn(II) and Sn(IV) Iodide Perovskites and Study of Their Structural, Chemical, Thermal, Optical, and Electrical Properties'. *Energy Technol.*, 2020, **8**, 1900788.

[167] Mundt, L. E.; Tong, J.; Palmstrom, A. F.; Dunfield, S. P.; Zhu, K.; Berry, J. J.; Schelhas, L. T. and Ratcliff, E. L. 'Surface-Activated Corrosion in Tin–Lead Halide Perovskite Solar Cells'. *ACS Energy Lett.*, 2020, **5**, 3344–3351.

[168] Motti, S. G.; Meggiolaro, D.; Martani, S.; Sorrentino, R.; Barker, A. J.; De Angelis, F. and Petrozza, A. 'Defect Activity in Lead Halide Perovskites'. *Adv. Mater.*, 2019, **31**, 1901183.

[169] Chen, J. and Park, N.-G. 'Causes and Solutions of Recombination in Perovskite Solar Cells'. *Adv. Mater.*, 2019, **31**, 1803019.

[170] Xu, P.; He, H.; Ding, J.; Wang, P.; Piao, H.; Bao, J.; Zhang, W.; Wu, X.; Xu, L.; Lin, P. *et al.* 'Simultaneous Passivation of the SnO_2/Perovskite Interface and Perovskite Absorber Layer in Perovskite Solar Cells Using KF Surface Treatment'. *ACS Appl. Energy Mater.*, 2021, **4**, 10921–10930.

[171] Gu, F.; Wang, S. F.; Song, C. F.; Lü, M. K.; Qi, Y. X.; Zhou, G. J.; Xu, D. and Yuan, D. R. 'Synthesis and Luminescence Properties of SnO_2 Nanoparticles'. *Chem. Phys. Lett.*, 2003, **372**, 451–454.

[172] Xiong, L.; Guo, Y.; Wen, J.; Liu, H.; Yang, G.; Qin, P. and Fang, G. 'Review on the Application of SNO2 in Perovskite Solar Cells'. *Adv. Funct. Mater.*, 2018, **28**, 1802757.

[173] Liu, D.; Wang, Y.; Xu, H.; Zheng, H.; Zhang, T.; Zhang, P.; Wang, F.; Wu, J.; Wang, Z.; Chen, Z. *et al.* 'SnO_2-Based Perovskite Solar Cells: Configuration Design and Performance Improvement'. *Sol. RRL*, 2019, **3**, 1800292.

[174] Xie, J.; Huang, K.; Yu, X.; Yang, Z.; Xiao, K.; Qiang, Y.; Zhu, X.; Xu, L.; Wang, P.; Cui, C. *et al.* 'Enhanced Electronic Properties of SnO_2 via Electron Transfer From Graphene Quantum Dots for Efficient Perovskite Solar Cells'. *ACS Nano*, 2017, **11**, 9176–9182.

[175] Godinho, K. G.; Walsh, A. and Watson, G. W. 'Energetic and Electronic Structure Analysis of Intrinsic Defects in SnO_2'. *J. Phys. Chem. C*, 2009, **113**, 439–448.

[176] Kubicki, D. J.; Prochowicz, D.; Salager, E.; Rakhmatullin, A.; Grey, C. P.; Emsley, L. and Stranks, S. D. 'Local Structure and Dynamics in Methylammonium, Formamidinium, and Cesium Tin(II) Mixed-Halide Perovskites From ^{119}Sn Solid-State NMR'. *J. Am. Chem. Soc.*, 2020, **142**, 7813–7826.

[177] Lim, V. J.-Y.; Righetto, M.; Yan, S.; Patel, J. B.; Siday, T.; Putland, B.; McCall, K. M.; Sirtl, M. T.; Kominko, Y.; Peng, J. *et al.* 'Contrasting Ultra-Low Frequency Raman and Infrared Modes in Emerging Metal Halides for Photovoltaics'. *ACS Energy Lett.*, 2024, **9**, 4127–4135.

[178] Li, M.; Fu, J.; Xu, Q. and Sum, T. C. 'Slow Hot-Carrier Cooling in Halide Perovskites: Prospects for Hot-Carrier Solar Cells'. *Adv. Mater.*, 2019, **31**, 1802486.

[179] Zhang, Y.; Conibeer, G.; Liu, S.; Zhang, J. and Guillemoles, J. F. 'Review of the Mechanisms for the Phonon Bottleneck Effect in III-V Semiconductors and Their Application for Efficient Hot Carrier Solar Cells'. *Prog. Photovoltaics Res. Appl.*, 2022, **30**, 581596.

[180] Zhang, X. B.; Taliercio, T.; Kolliakos, S. and Lefebvre, P. 'Influence of Electron-Phonon Interaction on the Optical Properties of III Nitride Semiconductors'. *J. Phys.: Condens. Matter*, 2001, **13**, 70537074.

[181] Segall, B. and Mahan, G. D. 'Phonon-Assisted Recombination of Free Excitons in Compound Semiconductors'. *Phys. Rev.*, 1968, **171**, 935.

[182] Coropceanu, V.; Cornil, J.; Silva Filho, D. A. da; Olivier, Y.; Silbey, R. and Brédas, J. L. 'Charge Transport in Organic Semiconductors'. *Chem. Rev.*, 2007, **107**, 926952.

[183] Sharif, R.; Khalid, A.; Ahmad, S. W.; Rehman, A.; Qutab, H. G.; Akhtar, H. H.; Mahmood, K.; Afzal, S. and Saleem, F. 'A Comprehensive Review of the Current Progresses and Material Advances in Perovskite Solar Cells'. *Nanoscale Adv.*, 2023, **5**, 38033833.

[184] Mayers, M. Z.; Tan, L. Z.; Egger, D. A.; Rappe, A. M. and Reichman, D. R. 'How Lattice and Charge Fluctuations Control Carrier Dynamics in Halide Perovskites'. *Nano Lett.*, 2018, **18**, 80418046.

[185] Herz, L. M. 'How Lattice Dynamics Moderate the Electronic Properties of Metal-Halide Perovskites'. *J. Phys. Chem. Lett.*, 2018, **9**, 68536863.

[186] Chu, W.; Zheng, Q.; Prezhdo, O. V.; Zhao, J. and Saidi, W. A. 'Low-Frequency Lattice Phonons in Halide Perovskites Explain High Defect Tolerance Toward Electron-Hole Recombination'. *Sci. Adv.*, 2020, **6**, 74537467.

[187] Yamada, Y. and Kanemitsu, Y. 'Electron-Phonon Interactions in Halide Perovskites'. *NPG Asia Mater.*, 2022, **14**, 48.

[188] Miyata, K.; Atallah, T. L. and Zhu, X. Y. 'Lead Halide Perovskites: Crystal-Liquid Duality, Phonon Glass Electron Crystals, and Large Polaron Formation'. *Sci. Adv.*, 2017, **3**, e1701469.

[189] Zhu, H.; Miyata, K.; Fu, Y.; Wang, J.; Joshi, P. P.; Niesner, D.; Williams, K. W.; Jin, S. and Zhu, X. Y. 'Screening in Crystalline Liquids Protects Energetic Carriers in Hybrid Perovskites'. *Science*, 2016, **353**, 14091413.

[190] Panzer, F.; Li, C.; Meier, T.; Kohler, A. and Huettner, S. 'Impact of Structural Dynamics on the Optical Properties of Methylammonium Lead Iodide Perovskites'. *Adv. Energy Mater.*, 2017, **7**, 1700286.

[191] Whalley, L. D.; Skelton, J. M.; Frost, J. M. and Walsh, A. 'Phonon Anharmonicity, Lifetimes, and Thermal Transport in $CH_3NH_3PbI_3$ from Many-Body Perturbation Theory'. *Phys. Rev. B*, 2016, **94**, 220301.

[192] Liu, W. W.; Wu, T. H.; Liu, M. C.; Niu, W. J. and Chueh, Y. L. 'Recent Challenges in Perovskite Solar Cells Toward Enhanced Stability, Less Toxicity, and Large-Area Mass Production'. *Adv. Mater. Interfaces*, 2019, **6**, 1801758.

[193] Ghosh, S.; Shankar, H. and Kar, P. 'Recent Developments of Lead-Free Halide Double Perovskites: A New Superstar in the Optoelectronic Field'. *Mater. Adv.*, 2022, **3**, 37423765.

[194] Yaffe, O.; Guo, Y.; Tan, L. Z.; Egger, D. A.; Hull, T.; Stoumpos, C. C.; Zheng, F.; Heinz, T. F.; Kronik, L.; Kanatzidis, M. G.; Owen, J. S.; Rappe, A. M.; Pimenta, M. A. and Brus, L. E. 'Local Polar Fluctuations in Lead Halide Perovskite Crystals'. *Phys. Rev. Lett.*, 2017, **118**, 136001.

[195] Hehlen, B.; Bourges, P.; Rufflé, B.; Clément, S.; Vialla, R.; Ferreira, A. C.; Ecolivet, C.; Paofai, S.; Cordier, S.; Katan, C.; Létoublon, A. and Even, J. 'Pseudospin-Phonon Pretransitional Dynamics and Rashba Paramagnons in 3D Hybrid Halide Perovskites'. *Adv. Funct. Mater.*, 2022, **32**, 2111543.

[196] Huang, X.; Li, X.; Tao, Y.; Guo, S.; Gu, J.; Hong, H.; Yao, Y.; Guan, Y.; Gao, Y.; Li, C.; Lü, X. and Fu, Y. 'Understanding Electron-Phonon Interactions in 3D Lead Halide Perovskites from the Stereochemical Expression of $6s^2$ Lone Pairs'. *J. Am. Chem. Soc.*, 2022, **144**, 12247–12260.

[197] Seiler, H.; Palato, S.; Sonnichsen, C.; Baker, H.; Socie, E.; Strandell, D. P. and Kambhampati, P. 'Two-Dimensional Electronic Spectroscopy Reveals Liquid-like Lineshape Dynamics in $CsPbI_3$ Perovskite Nanocrystals'. *Nat. Commun.*, 2019, **10**, 4962.

[198] Sharma, R.; Dai, Z.; Gao, L.; Brenner, T. M.; Yadgarov, L.; Zhang, J.; Rakita, Y.; Korobko, R.; Rappe, A. M. and Yaffe, O. 'Elucidating the Atomistic Origin of Anharmonicity in Tetragonal $CH_3NH_3PbI_3$ with Raman Scattering'. *Phys. Rev. Mater.*, 2020, **4**, 092401.

[199] Gao, L.; Yadgarov, L.; Sharma, R.; Korobko, R.; McCall, K. M.; Fabini, D. H.; Stoumpos, C. C.; Kanatzidis, M. G.; Rappe, A. M. and Yaffe, O. 'Metal Cation s Lone-Pairs Increase Octahedral Tilting Instabilities in Halide Perovskites'. *Mater. Adv.*, 2021, **2**, 4610–4616.

[200] Zhao, D.; Skelton, J. M.; Hu, H.; La-O-Vorakiat, C.; Zhu, J. X.; Marcus, R. A.; Michel-Beyerle, M. E.; Lam, Y. M.; Walsh, A. and Chia, E. E. M. 'Low-Frequency Optical Phonon Modes and Carrier Mobility in the Halide Perovskite $CH_3NH_3PbBr_3$ Using Terahertz Time-Domain Spectroscopy'. *Appl. Phys. Lett.*, 2017, **111**, 201903.

[201] La-O-Vorakiat, C.; Xia, H.; Kadro, J.; Salim, T.; Zhao, D.; Ahmed, T.; Lam, Y. M.; Zhu, J. X.; Marcus, R. A.; Michel-Beyerle, M. E. and Chia, E. E. M. 'Phonon Mode Transformation Across the Orthorhombic-Tetragonal Phase Transition in a Lead Iodide Perovskite $CH_3NH_3PbI_3$: A Terahertz Time-Domain Spectroscopy Approach'. *J. Phys. Chem. Lett.*, 2016, **7**, 1–6.

[202] Johnston, M. B. and Herz, L. M. 'Hybrid Perovskites for Photovoltaics: Charge-Carrier Recombination, Diffusion, and Radiative Efficiencies'. *Acc. Chem. Res.*, 2016, **49**, 146–154.

[203] Cohen, A.; Brenner, T. M.; Klarbring, J.; Sharma, R.; Fabini, D. H.; Korobko, R.; Nayak, P. K.; Hellman, O. and Yaffe, O. 'Diverging Expressions of Anharmonicity in Halide Perovskites'. *Adv. Mater.*, 2022, **34**, 2107932.

[204] Pérez-Osorio, M. A.; Lin, Q.; Phillips, R. T.; Milot, R. L.; Herz, L. M.; Johnston, M. B. and Giustino, F. 'Raman Spectrum of the Organic-Inorganic Halide Perovskite $CH_3NH_3PbI_3$ from First Principles and High-Resolution Low-Temperature Raman Measurements'. *J. Phys. Chem. C*, 2018, **122**, 21703–21717.

[205] Maalej, A.; Abid, Y.; Kallel, A.; Daoud, A.; Lautié, A. and Romain, F. 'Phase Transitions and Crystal Dynamics in the Cubic Perovskite $CH_3NH_3PbCl_3$'. *Solid State Commun.*, 1997, **103**, 279–284.

[206] Menahem, M.; Benshalom, N.; Asher, M.; Aharon, S.; Korobko, R.; Hellman, O. and Yaffe, O. 'Disorder Origin of Raman Scattering in Perovskite Single Crystals'. *Phys. Rev. Mater.*, 2023, **7**, 044602.

[207] Cowley, R. A. 'Anharmonic Crystals'. *Rep. Prog. Phys.*, 1968, **31**, 123.

[208] Iaru, C. M.; Brodu, A.; Hoof, N. J. J. van; Huurne, S. E. T. ter; Buhot, J.; Montanarella, F.; Buhbut, S.; Christianen, P. C. M.; Vanmaekelbergh, D.; Mello Donega, C. de; Rivas, J. G.; Koenraad, P. M. and Silov, A. Y. ‘Fröhlich Interaction Dominated by a Single Phonon Mode in $CsPbBr_3$’. *Nat. Commun.*, 2021, **12**, 5844.

[209] Rodríguez-Suárez, R.; Menéndez-Proupin, E.; Trallero-Giner, C. and Cardona, M. ‘Multiphonon Resonant Raman Scattering in Nanocrystals’. *Phys. Rev. B*, 2000, **62**, 11006.

[210] Quarti, C.; Mosconi, E.; Ball, J. M.; D’Innocenzo, V.; Tao, C.; Pathak, S.; Snaith, H. J.; Petrozza, A. and Angelis, F. D. ‘Structural and Optical Properties of Methylammonium Lead Iodide across the Tetragonal to Cubic Phase Transition: Implications for Perovskite Solar Cells’. *Energy Environ. Sci.*, 2016, **9**, 155–163.

[211] Beecher, A. N.; Semonin, O. E.; Skelton, J. M.; Frost, J. M.; Terban, M. W.; Zhai, H.; Alatas, A.; Owen, J. S.; Walsh, A. and Billinge, S. J. L. ‘Direct Observation of Dynamic Symmetry Breaking above Room Temperature in Methylammonium Lead Iodide Perovskite’. *ACS Energy Lett.*, 2016, **1**, 880–887.

[212] Fabini, D. H.; Laurita, G.; Bechtel, J. S.; Stoumpos, C. C.; Evans, H. A.; Kontos, A. G.; Raptis, Y. S.; Falaras, P.; Ven, A. V. D.; Kanatzidis, M. G. and Seshadri, R. ‘Dynamic Stereochemical Activity of the Sn2+ Lone Pair in Perovskite $CsSnBr_3$’. *J. Am. Chem. Soc.*, 2016, **138**, 11820–11832.

[213] Remsing, R. C. and Klein, M. L. ‘A New Perspective on Lone Pair Dynamics in Halide Perovskites’. *APL Mater.*, 2020, **8**, 050902.

[214] Fabini, D. H.; Seshadri, R. and Kanatzidis, M. G. ‘The Underappreciated Lone Pair in Halide Perovskites Underpins Their Unusual Properties’. *MRS Bull.*, 2020, **45**, 467–477.

[215] Caicedo-Dávila, S.; Cohen, A.; Motti, S. G.; Isobe, M.; McCall, K. M.; Grumet, M.; Kovalenko, M. V.; Yaffe, O.; Herz, L. M.; Fabini, D. H. and Egger, D. A. ‘Disentangling the Effects of Structure and Lone-Pair Electrons in the Lattice Dynamics of Halide Perovskites’. *Nat. Commun.*, 2024, **15**, 4184.

[216] Lee, J. H.; Bristowe, N. C.; Lee, J. H.; Lee, S. H.; Bristowe, P. D.; Cheetham, A. K. and Jang, H. M. ‘Resolving the Physical Origin of Octahedral Tilting in Halide Perovskites’. *Chem. Mater.*, 2016, **28**, 4259–4266.

[217] Kieslich, G.; Sun, S. and Cheetham, A. K. ‘Solid-State Principles Applied to OrganicInorganic Perovskites: New Tricks for an Old Dog’. *Chem. Sci.*, 2014, **5**, 4712–4715.

[218] Baldwin, W. J.; Liang, X.; Klarbring, J.; Dubajic, M.; Dell’Angelo, D.; Sutton, C.; Caddeo, C.; Stranks, S. D.; Mattoni, A.; Walsh, A. and Csányi, G. ‘Dynamic Local Structure in Caesium Lead Iodide: Spatial Correlation and Transient Domains’. *Small*, 2024, **20**, 2303565.

[219] Dahod, N. S.; France-Lanord, A.; Paritmongkol, W.; Grossman, J. C. and Tisdale, W. A. ‘Low-Frequency Raman Spectrum of 2D Layered Perovskites: Local Atomistic Motion or Superlattice Modes?’ *J. Chem. Phys.*, 2020, **153**, 44710.

[220] Harvey, S. P.; Li, Z.; Christians, J. A.; Zhu, K.; Luther, J. M. and Berry, J. J. ‘Probing Perovskite Inhomogeneity beyond the Surface: TOF-SIMS Analysis of Halide Perovskite Photovoltaic Devices’. *ACS Appl. Mater. Interfaces*, 2018, **10**, 28541–28552.

[221] Halperin, B. I. and Varma, C. M. 'Defects and the Central Peak near Structural Phase Transitions'. *Phys. Rev. B*, 1976, **14**, 4030.

[222] Folk, R. and Schwabl, F. 'EPR in $SrTiO_3$: Dynamical or Dirt Effect?' *Solid State Commun.*, 1974, **15**, 937–940.

[223] Li, C.; Sun, H.; Gan, S.; Dou, D. and Li, L. 'Perovskite Single Crystals: Physical Properties and Optoelectronic Applications'. *Mater. Futur.*, 2023, **2**, 042101.

[224] Naftaly, M. and Gregory, A. 'Terahertz and Microwave Optical Properties of Single-crystal Quartz and Vitreous Silica and the Behavior of the Boson Peak'. *Appl. Sci.*, 2021, **11**, 6733.

[225] Rakita, Y.; Cohen, S. R.; Kedem, N. K.; Hodes, G. and Cahen, D. 'Mechanical Properties of $APbX_3$ (A = Cs or CH_3NH_3; X = I or Br) Perovskite Single Crystals'. *MRS Commun.*, 2015, **5**, 623–629.

[226] Hassan, A. K.; Börjesson, L. and Torell, L. M. 'The Boson Peak in Glass Formers of Increasing Fragility'. *J. Non. Cryst. Solids*, 1994, **172174**, 368374.

[227] Malinovsky, V. K. and Sokolov, A. P. 'The Nature of Boson Peak in Raman Scattering in Glasses'. *Solid State Commun.*, 1986, **57**, 757–761.

[228] Sommer, R.; Toulouse, J. and Jain, H. 'A Low Frequency Study of the Vibrational Modes in Alkali-Silicate Glasses by Raman Spectroscopy'. *MRS Online Proc. Libr. 1995 4071*, 1995, **407**, 215–220.

[229] Mori, T.; Jiang, Y.; Fujii, Y.; Kitani, S.; Mizuno, H.; Koreeda, A.; Motoji, L.; Tokoro, H.; Shiraki, K.; Yamamoto, Y. and Kojima, S. 'Detection of Boson Peak and Fractal Dynamics of Disordered Systems Using Terahertz Spectroscopy'. *Phys. Rev. E*, 2020, **102**, 022502.

[230] Grigera, T. S.; Martín-Mayor, V.; Parisi, G. and Verrocchio, P. 'Phonon Interpretation of the "boson Peak" in Supercooled Liquids'. *Nature*, 2003, **422**, 289–292.

[231] Nakayama, T. 'Boson Peak and Terahertz Frequency Dynamics of Vitreous Silica'. *Rep. Prog. Phys.*, 2002, **65**, 1195.

[232] Shuker, R. and Gammon, R. W. 'Raman-Scattering Selection-Rule Breaking and the Density of States in Amorphous Materials'. *Phys. Rev. Lett.*, 1970, **25**, 222.

[233] Galeener, F. L. and Sen, P. N. 'Theory for the First-Order Vibrational Spectra of Disordered Solids'. *Phys. Rev. B*, 1978, **17**, 1928.

[234] Ando, M. F.; Fuhrmann, S.; Pan, Z.; Rodrigues, B. P.; Mori, T.; Ebbinghaus, S. G.; Wondraczek, K.; Kitani, S. and Wondraczek, L. 'Boson Peak and Structural Heterogeneity in Ternary SiO_2-Al_2O_3-B_2O_3 Glasses'. *J. Am. Ceram. Soc.*, 2021, **104**, 4991–5000.

[235] Smith, J. E.; Brodsky, M. H.; Crowder, B. L.; Nathan, M. I. and Pinczuk, A. 'Raman Spectra of Amorphous Si and Related Tetrahedrally Bonded Semiconductors'. *Phys. Rev. Lett.*, 1971, **26**, 642.

[236] Burns, G.; Dacol, F. H.; Shafer, M. W. and Alben, R. 'The Raman Spectra of the Superionic Conductor CuI in Its Three Phases'. *Solid State Commun.*, 1977, **24**, 753–757.

[237] Bouziane, E.; Fontana, M. D. and Ayadi, M. 'Study of the Low-Frequency Raman Scattering in $NaNbO_3$ Crystal'. *J. Phys.: Condens. Matter*, 2003, **15**, 1387–1395.

[238] Fontana, M. D.; Kokanyan, N. and Kauffmann, T. H. ‘Sub-THz Raman Response in $BaTiO_3$ and Link with Structural Phase Transition’. *J. Phys.: Condens. Matter*, 2020, **32**, 285403.

[239] Ahmad, N.; Hutt, K. W. and Phillips, W. A. ‘Low-Frequency Vibrational States in As_2S_3 Glasses’. *J. Phys. C: Solid State Phys.*, 1986, **19**, 3765–3773.

[240] Surovtsev, N. V. and Sokolov, A. P. ‘Frequency Behavior of Raman Coupling Coefficient in Glasses’. *Phys. Rev. B*, 2002, **66**, 054205.

[241] Surovtsev, N. V. ‘Features of the Raman Coupling Coefficient of Boson Peak Vibrations in Glasses’. *Phys. Status Solidi C: Conferences*, 2004, **1**, 2867–2870.

[242] Zwick, A. and Carles, R. ‘Multiple-Order Raman Scattering in Crystalline and Amorphous Silicon’. *Phys. Rev. B*, 1993, **48**, 6024.

[243] Carles, R.; Bayle, M.; Benzo, P.; Benassayag, G.; Bonafos, C.; Cacciato, G. and Privitera, V. ‘Plasmon-Resonant Raman Spectroscopy in Metallic Nanoparticles: Surface-Enhanced Scattering by Electronic Excitations’. *Phys. Rev. B*, 2015, **92**, 174302.

[244] Leguy, A. M. A.; Goñi, A. R.; Frost, J. M.; Skelton, J.; Brivio, F.; Rodríguez-Martínez, X.; Weber, O. J.; Pallipurath, A.; Alonso, M. I.; Campoy-Quiles, M.; Weller, M. T.; Nelson, J.; Walsh, A. and Barnes, P. R. F. ‘Dynamic Disorder, Phonon Lifetimes, and the Assignment of Modes to the Vibrational Spectra of Methylammonium Lead Halide Perovskites’. *Phys. Chem. Chem. Phys.*, 2016, **18**, 27051–27066.

[245] Quarti, C.; Grancini, G.; Mosconi, E.; Bruno, P.; Ball, J. M.; Lee, M. M.; Snaith, H. J.; Petrozza, A. and De Angelis, F. ‘The Raman Spectrum of the $CH_3NH_3PbI_3$ Hybrid Perovskite: Interplay of Theory and Experiment’. *J. Phys. Chem. Lett.*, 2014, **5**, 279–284.

[246] Ibaceta-Jaña, J.; Muydinov, R.; Rosado, P.; Mirhosseini, H.; Chugh, M.; Nazarenko, O.; Dirin, D. N.; Heinrich, D.; Wagner, M. R.; Kühne, T. D.; Szyszka, B.; Kovalenko, M. V. and Hoffmann, A. ‘Vibrational Dynamics in Lead Halide Hybrid Perovskites Investigated by Raman Spectroscopy’. *Phys. Chem. Chem. Phys.*, 2020, **22**, 5604–5614.

[247] Ghosh, S.; Rana, D.; Pradhan, B.; Donfack, P.; Hofkens, J. and Materny, A. ‘Vibrational Study of Lead Bromide Perovskite Materials with Variable Cations Based on Raman Spectroscopy and Density Functional Theory’. *J. Raman Spectrosc.*, 2021, **52**, 2338–2347.

[248] Pérez-Osorio, M. A.; Milot, R. L.; Filip, M. R.; Patel, J. B.; Herz, L. M.; Johnston, M. B. and Giustino, F. ‘Vibrational Properties of the Organic-Inorganic Halide Perovskite $CH_3NH_3PbI_3$ from Theory and Experiment: Factor Group Analysis, First-Principles Calculations, and Low-Temperature Infrared Spectra’. *J. Phys. Chem. C*, 2015, **119**, 25703–25718.

[249] Sendner, M.; Nayak, P. K.; Egger, D. A.; Beck, S.; Müller, C.; Epding, B.; Kowalsky, W.; Kronik, L.; Snaith, H. J.; Pucci, A. and Lovrincic, R. ‘Optical Phonons in Methylammonium Lead Halide Perovskites and Implications for Charge Transport’. *Mater. Horizons*, 2016, **3**, 613–620.

[250] Klemens, P. G. ‘Anharmonic Decay of Optical Phonons’. *Phys. Rev.*, 1966, **148**, 845.

[251] Sekiguchi, F.; Hirori, H.; Yumoto, G.; Shimazaki, A.; Nakamura, T.; Wakamiya, A. and Kanemitsu, Y. ‘Enhancing the Hot-Phonon Bottleneck Effect in a Metal Halide Perovskite by Terahertz Phonon Excitation’. *Phys. Rev. Lett.*, 2021, **126**, 077401.

[252] Debernardi, A.; Ulrich, C.; Syassen, K. and Cardona, M. ‘Raman Linewidths of Optical Phonons in 3C-SiC under Pressure: First-Principles Calculations and Experimental Results’. *Phys. Rev. B - Condens. Matter Mater. Phys.*, 1999, **59**, 6774–6783.

[253] Vallée, F. and Bogani, F. ‘Coherent Time-Resolved Investigation of LO-Phonon Dynamics in GaAs’. *Phys. Rev. B*, 1991, **43**, 12049.

[254] Ridley, B. K. and Gupta, R. ‘Nonelectronic Scattering of Longitudinal-Optical Phonons in Bulk Polar Semiconductors’. *Phys. Rev. B*, 1991, **43**, 4939.

[255] Wright, A. D.; Verdi, C.; Milot, R. L.; Eperon, G. E.; Pérez-Osorio, M. A.; Snaith, H. J.; Giustino, F.; Johnston, M. B. and Herz, L. M. ‘Electron-Phonon Coupling in Hybrid Lead Halide Perovskites’. *Nat. Commun.*, 2016, **7**, 11755.

[256] Munson, K. T.; Swartzfager, J. R. and Asbury, J. B. ‘Lattice Anharmonicity: A Double-Edged Sword for 3D Perovskite-Based Optoelectronics’. *ACS Energy Lett.*, 2019, **4**, 1888–1897.

[257] Ferreira, A. C.; Paofai, S.; Létoublon, A.; Ollivier, J.; Raymond, S.; Hehlen, B.; Rufflé, B.; Cordier, S.; Katan, C.; Even, J. and Bourges, P. ‘Direct Evidence of Weakly Dispersed and Strongly Anharmonic Optical Phonons in Hybrid Perovskites’. *Commun. Phys.*, 2020, **3**, 48.

[258] Lanigan-Atkins, T.; He, X.; Krogstad, M. J.; Pajerowski, D. M.; Abernathy, D. L.; Xu, G. N. M. N.; Xu, Z.; Chung, D. Y.; Kanatzidis, M. G.; Rosenkranz, S.; Osborn, R. and Delaire, O. ‘Two-Dimensional Overdamped Fluctuations of the Soft Perovskite Lattice in $CsPbBr_3$’. *Nat. Mater.*, 2021, **20**, 977–983.

[259] Li, B.; Kawakita, Y.; Liu, Y.; Wang, M.; Matsuura, M.; Shibata, K.; Ohira-Kawamura, S.; Yamada, T.; Lin, S.; Nakajima, K. and Liu, S. F. ‘Polar Rotor Scattering as Atomic-Level Origin of Low Mobility and Thermal Conductivity of Perovskite $CH_3NH_3PbI_3$’. *Nat. Commun.*, 2017, **8**, 16086.

[260] Gehrmann, C. and Egger, D. A. ‘Dynamic Shortening of Disorder Potentials in Anharmonic Halide Perovskites’. *Nat. Commun.*, 2019, **10**, 3141.

[261] de Mello, J. C.; Wittmann, H. F. and Friend, R. H. ‘An Improved Experimental Determination of External Photoluminescence Quantum Efficiency’. *Adv. Mater.*, 1997, **9**, 230–232.

[262] Kirchartz, T.; Márquez, J. A.; Stolterfoht, M. and Unold, T. ‘Photoluminescence-Based Characterization of Halide Perovskites for Photovoltaics’. *Adv. Energy Mater.*, 2020, **10**, 1904134.

[263] Klug, M. T.; Milot, R. L.; Patel, J. B.; Green, T.; Sansom, H. C.; Farrar, M. D.; Ramadan, A. J.; Martani, S.; Wang, Z.; Wenger, B. *et al.* ‘Metal Composition Influences Optoelectronic Quality in Mixed-Metal Lead–Tin Triiodide Perovskite Solar Absorbers’. *Energy Environ. Sci.*, 2020, **13**, 1776–1787.

[264] Poncé, S.; Schlipf, M. and Giustino, F. ‘Origin of Low Carrier Mobilities in Halide Perovskites’. *ACS Energy Lett.*, 2019, **4**, 456–463.

[265] Umari, P.; Mosconi, E. and De Angelis, F. ‘Relativistic GW Calculations on $CH_3NH_3PbI_3$ and $CH_3NH_3SnI_3$ Perovskites for Solar Cell Applications’. *Sci. Rep.*, 2014, **4**, 4467.

[266] Noel, N. K.; Habisreutinger, S. N.; Wenger, B.; Klug, M. T.; Hörantner, M. T.; Johnston, M. B.; Nicholas, R. J.; Moore, D. T. and Snaith, H. J. 'A Low Viscosity, Low Boiling Point, Clean Solvent System for the Rapid Crystallisation of Highly Specular Perovskite Films'. *Energy Environ. Sci.*, 2017, **10**, 145–152.

[267] Lin, Q.; Armin, A.; Burn, P. L. and Meredith, P. 'Near Infrared Photodetectors Based on Sub-Gap Absorption in Organohalide Perovskite Single Crystals'. *Laser Photonics Rev.*, 2016, **10**, 1047–1053.

[268] Saidaminov, M. I.; Abdelhady, A. L.; Murali, B.; Alarousu, E.; Burlakov, V. M.; Peng, W.; Dursun, I.; Wang, L.; He, Y.; Maculan, G. *et al.* 'High-Quality Bulk Hybrid Perovskite Single Crystals Within Minutes by Inverse Temperature Crystallization'. *Nat. Commun.*, 2015, **6**, 7586.